A Measurement of the Partial Width of the Z^0 Boson Into b Quarks and the Forward-Backward Asymmetry in the Reaction $e^+e^- \rightarrow Z^0 \rightarrow b\bar{b}$, Using Inclusive Electrons

by

Paul Robert Schenk

B.Sc., University of Western Ontario, 1987

M.Sc., University of Victoria, 1989

A Dissertation Submitted In Partial Fulfillment of the Requirements for the Degree of

DOCTOR OF PHILOSOPHY

in the Department of Physics and Astronomy

We accept this dissertation as conforming to the required standard

---

Dr.A. Astbury, Supervisor (Department of Physics and Astronomy)

Dr.R. Keeler, Departmental Member (Department of Physics and Astronomy)

Dr.L. Robertson, Departmental Member (Department of Physics and Astronomy)

Dr.T.W. Dingle, Outside Member (Department of Chemistry)

Dr.D. Harrington, Outside Member (Department of Chemistry)

Dr.R. Dubois, External Examiner (Stanford Linear Accelerator Center)

Supervisor: Dr.A. Astbury

ABSTRACT

The process $e^+e^- \rightarrow Z^0 \rightarrow b\bar{b}$ is studied using prompt electrons. The partial width of the Z^0 boson into $b\bar{b}$ pairs is found to be $400 \pm 35 \pm 57 \pm 3$ MeV, and the forward-backward asymmetry in the reaction $e^+e^- \rightarrow Z^0 \rightarrow b\bar{b}$ is found to be $0.101 \pm 0.029 \pm 0.011 \pm 0.006$.

Examiners:

Dr.A. Astbury, Supervisor (Department of Physics and Astronomy)

Dr.R. Keeler, Departmental Member (Department of Physics and Astronomy)

Dr.L. Robertson, Departmental Member (Department of Physics and Astronomy)

Dr.T.W. Dingle, Outside Member (Department of Chemistry)

Dr.D. Harrington, Outside Member (Department of Chemistry)

Dr.R. Dubois, External Examiner (Stanford Linear Accelerator Center)

Contents

List of Tables

List of Figures

Acknowledgements

There is a great number of people to whom I owe deep gratitude for their help and support during the long journey that led to this dissertation. First and foremost I express my deep thanks to the entire OPAL collaboration for creating a working environment which is so pleasant and productive.

While everybody in OPAL has contributed in some way to this work, I must express special thanks to: R. Shypit, from whom I have learned a great deal; J. Kroll for his help in the understanding of the CLEO branching ratio measurements; S. Tarem for her collaboration in the asymmetry measurement and, along with R. Van Kooten, for developing the conversion finder used in this work.

Finally, R. d'Entremont has lived through the highs and lows of this work and her unfailing support and company have made it all that much easier

Chapter 1

Introduction

The physics of elementary particles has advanced from trying to understand the properties of a large collection of particles, to dealing with only twelve fermions (the quarks and leptons), one spin zero boson, and twelve spin one bosons that mediate the possible interactions [1]. These interactions are the strong force, responsible for the nuclear binding; the weak interaction, responsible for nuclear beta decay; and electromagnetism, responsible for atomic binding. There exists a theory that predicts the behaviour of the weak and electromagnetic interactions as one ensemble. It is this theory that will be tested in this thesis.

Certain conditions must be satisfied for the theory to make meaningful (i.e. finite) predictions for all energies. There must be three times as many quarks as leptons, ensuring that the sum of the charges of the fermions is zero. This is achieved by the inclusion of a quantum number called "colour". Each quark may have one of three possible values of the colour quantum number. The interaction involving this quantum number is the strong force. The weak and electromagnetic interactions are blind to colour. A scalar particle is introduced to incorporate mass into the theory. Finally, in addition to the weak interaction which transfers charge, there must be a weak interaction that does not involve the transfer of charge.

The Z^0 boson was predicted to be the mediator of the weak interaction that does not involve a transfer of charge. Such "neutral current" interactions were first seen in neutrino scattering experiments in 1973 [2] and the Z^0 boson was observed directly in proton-antiproton collisions in 1983 [3]. The LEP accelerator [4] at CERN was designed to study in detail the properties of the Z^0 boson using the clean environment of e^+e^- collisions.

Figure 1.1 shows some cross sections for e^+e^- collisions as a function of centre of mass energy. In processes where a Z^0 can be produced a large enhancement is

[1] Although the measurement of the mass of the Z^0 at LEP has become the first particle physics measurement to be significantly affected by all the known forces of nature [1], the force of gravity will be ignored here.

evident when the centre of mass energy is equal to the mass of the Z^0. Experimentally this large enhancement yields high rates, making possible the determination of the couplings of the fermions to the Z^0. In particular, final states with quark-antiquark pairs provide a practical opportunity to study in detail the properties of the quarks.

The LEP accelerator [4] is housed in a 27 km circumference ring at an average depth of approximately 50m. Positrons and electrons circulate in opposite directions, colliding in eight possible points around the ring. The design luminosity of the machine is 1.6×10^{31} cm^{-2}s^{-1} with a centre of mass energy of 100 GeV. There are detectors in four of the eight collision points, ALEPH [6], DELPHI [7], L3 [8] and OPAL [9]. The work in this thesis uses data collected with the OPAL detector.

The first physics run of LEP was in September 1989 and approximately 20 pb^{-1} of integrated luminosity was delivered to each experiment during the period of 1989 to 1991. Only the data collected during the 1990 and 1991 LEP running periods are used here. During those runs, LEP was operated at approximately seven different centre of mass energies. Table 1.1 shows the integrated luminosities recorded at each energy point by the OPAL detector.

centre of mass energy (GeV)	(nb^{-1}) (1990)	(nb^{-1}) (1991)
88	485	90
89	627	114
90	393	159
91	3432	5763
92	457	161
93	563	277
94	562	–

Table 1.1: *The integrated luminosity recorded, by OPAL, at the various beam energies during the 1990 and 1991 running periods. The peak of the cross section is at approximately 91.26 GeV, the energies given in the table are rounded to the nearest integer. The luminosity values correspond to the detector conditions demanded for the forward-backward asymmetry measurement.*

Due to the possibility of good statistical precision, it is possible to test the current theory of the interactions of the Z^0. This thesis reports on two measurements of the coupling of the Z^0 to the b quark; the partial decay width of the Z^0 into b quarks (the fraction of the total number of Z^0 decays that are $b\bar{b}$ pairs) and the forward-backward charge asymmetry in the reaction $e^+e^- \to Z^0 \to b\bar{b}$. Together these measurements test the strength and form of the coupling of the Z^0 to b quarks.

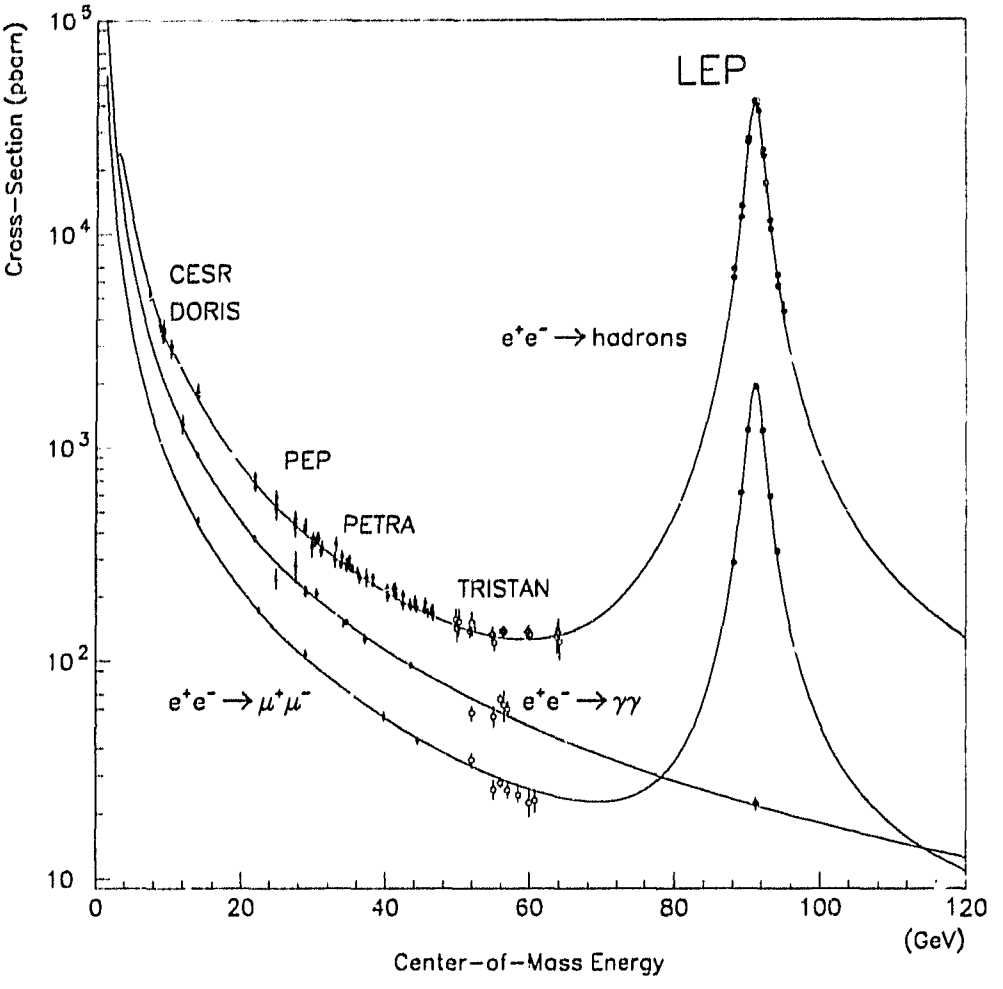

Figure 1.1: *The cross section for e^+e^- interactions shown as a function of the centre of mass energy [5].*

Such tests are important, as it is widely believed that the current theory is only a low energy approximation of some deeper underlying truth. Deviations from the predictions of the current theory may point the way to uncovering any hidden aspects of the nature of elementary particle interactions.

Chapter 2

Theory

2.1 Electroweak Theory

The unified theory of the electromagnetic and weak interactions results from work by Glashow, Weinberg and Salam (GSW) [10, 11, 12]. Along with Quantum Chromodynamics (QCD), a gauge theory of the strong interaction, it forms the basis of the Standard Model of the interactions of quarks and leptons. The gauge structure of the Standard Model is $SU(2)\times U(1)\times SU(3)$, and the interactions are mediated by twelve vector gauge bosons; eight coloured gluons of the strong interaction, W^+ and W^- of the charged current weak interaction, Z^0 of the neutral current weak interaction, and the photon of the electromagnetic interaction. Only the "electroweak" sector of $SU(2)\times U(1)$ will be discussed here.

The GSW theory has many free parameters; two coupling constants (g_1 and g_2) for the U(1) and SU(2) groups, the masses and mixings of the fermions, a vacuum expectation value of a scalar field (the Higgs field), and the mass of a scalar particle (the Higgs boson). The theory reduces to the Fermi theory of charged current weak interactions [13] and QED [14] at low energies. Thus, by construction, the theory explains all experimental data of charged current weak interactions at energies much below 100 GeV and incorporates QED. This theory also predicted the existence of neutral current weak interactions which were first observed in 1973 [2]. It is these neutral current weak interactions that are the subject of this thesis.

Due to the renormalisability of the GSW theory, only a finite number of experimental inputs are needed to fix the predictions of the theory at all orders of perturbation theory. Since the couplings g_1 and g_2, along with the vacuum expectation value (v) of the scalar field are not measurable directly, a set of experimental observables must be chosen to fix the theory. The choice is completely arbitrary, and all choices are equivalent in the limit of infinite experimental precision and infinite orders of perturbation theory. One set of input parameters, based on phys-

ically meaningful inputs, has become predominant in the literature. These inputs are $\alpha = e^2/4\pi$ measured in Thompson scattering ($q^2 = 0$)(e is the charge of the electron), the masses of the $W^{\pm}$ and Z^0 gauge bosons (m_W and m_{Z^0}), the mass of the Higgs scalar m_{Higgs} and the masses of the fermions in the theory m_f. Some of these input parameters are not known or are known to a fairly low precision. There are methods to overcome these uncertainties and with our present knowledge the theory is well constrained. It is important to measure as many independent observables as possible to expose any inconsistencies in the predictions, as even one measurement which is inconsistent with the predictions will demand modifications to the theory.

In the Standard Model, the lowest order cross section for the process $e^+e^- \to f\bar{f}$ (γ and Z^0 exchange) is given by [15]

$$\begin{aligned}\frac{d\sigma}{d\Omega} = \quad & \frac{\alpha^2}{4s} N_c^f \sqrt{1-4\mu_f}\,[\,G_1(s)(1+\cos^2\theta) \\ & + G_3(s) 2\cos\theta\sqrt{1-4\mu_f} + 4\mu_f G_2(s)\sin^2\theta\,]\,.\end{aligned} \tag{2.1}$$

Where

$$\begin{aligned} G_1(s) &= Q_f^2 - 2Q_f\nu_e\nu_f \mathrm{Re}[\chi_0(s)] + \\ &\quad (\nu_e^2+a_e^2)(\nu_f^2+a_f^2-4\mu_f a_f^2)|\chi_0(s)|^2 \\ G_2(s) &= Q_f^2 - 2Q_f\nu_e\nu_f \mathrm{Re}[\chi_0(s)] + (\nu_e^2+a_e^2)\nu_f^2|\chi_0(s)|^2 \\ G_3(s) &= -2Q_f a_e a_f \mathrm{Re}[\chi_0(s)] + 4\nu_e a_e \nu_f a_f |\chi_0(s)|^2. \end{aligned}$$

The factor N_c is 1 for leptons and 3 for quark final states, f denotes the final state fermion and $\mu_f = m_f^2/s$, where s is the centre of mass energy squared. Q_f is the charge of the fermion, and ν_f and a_f are the vector and axial vector couplings of the fermion to the Z^0. The factor $\chi_0(s)$ is given by

$$\chi_0(s) = \frac{s}{s - m_{Z^0}^2 + i m_{Z^0}\Gamma_{Z^0}}, \tag{2.2}$$

with $m_{Z^0}^2$, the mass, and Γ_{Z^0}, the width, of the Z^0 boson. Figure 2.1 shows the cross section for the process $e^+e^- \to$ hadrons as a function of the centre of mass energy as measured by OPAL [16]. The hadronic cross section is (30.86 ± 0.62) nb [16] at the Z^0 peak.

By introducing the notation

$$c_W = \frac{m_W}{m_{Z^0}} \tag{2.3}$$

and

$$s_W = \sqrt{1 - c_W^2} \tag{2.4}$$

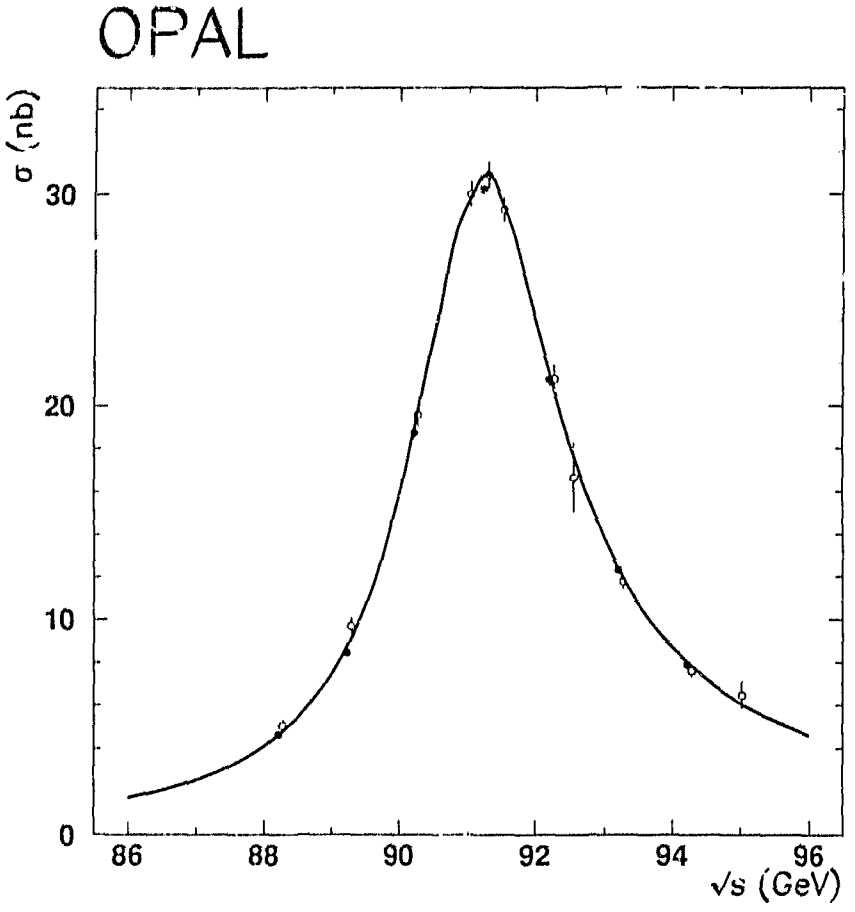

Figure 2.1: *The cross section for the process* $e^+e^- \rightarrow$ hadrons *measured by OPAL [16]. The open points are for the data collected during the 1989 LEP running period and the solid points are for the 1990 running period. The curve is the prediction of the Standard Model.*

the factors ν_f and a_f are given by

$$\nu_f = \frac{I_3^f - 2s_W^2 Q_f}{2s_W c_W} \tag{2.5}$$

$$a_f = \frac{I_3^f}{2s_W c_W}. \tag{2.6}$$

Table 2.1 shows the charge (Q) and isospin projection (I_3) assignments for the known fermions, along with the postulated top quark.

fermion	Q (units of e)	I_3
ν_e	0	1/2
e	-1	-1/2
ν_μ	0	1/2
μ	-1	-1/2
ν_τ	0	1/2
τ	-1	-1/2
u	2/3	1/2
d	-1/3	-1/2
c	2/3	1/2
s	-1/3	-1/2
t	2/3	1/2
b	-1/3	-1/2

Table 2.1: *The charge (Q) and isospin projection (I_3) for the fermions in the electroweak theory.*

The forward-backward asymmetry (A_{FB}) is defined as

$$A_{FB} = \frac{\sigma(\cos\theta > 0) - \sigma(\cos\theta < 0)}{\sigma(\cos\theta > 0) + \sigma(\cos\theta < 0)}, \tag{2.7}$$

the difference between the number of events with the outgoing fermion scattered in the forward ($\cos\theta > 0$) direction (N_F) and the number in the backward direction (N_B) divided by the total number of events. θ is the angle of the outgoing fermion with respect to the incoming electron direction (Figure 2.2). At centre of mass energies near to the mass of the Z^0, mass terms for the known fermions in the cross section formula (Equation 2.1) may be neglected and Equation 2.7 becomes,

$$A_{FB}^f = \frac{3\nu_e a_e \nu_f a_f}{(\nu_e^2 + a_e^2)(\nu_f^2 + a_f^2)}, \tag{2.8}$$

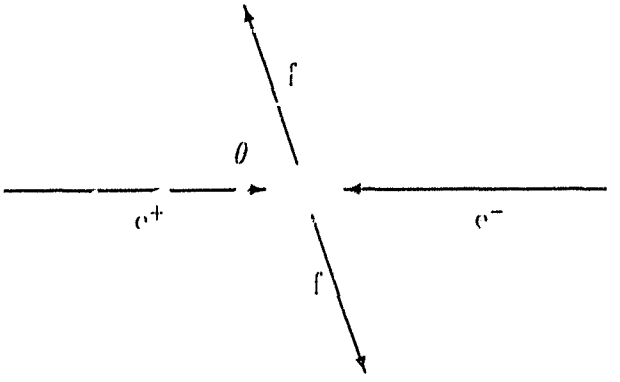

Figure 2.2: *Definition of the angle θ. Note that θ is the angle between the incoming electron momentum vector and the outgoing fermion momentum vector.*

for the process $e^+e^- \to Z^0 \to f\bar{f}$. This also implies that, for $\sqrt{s} \approx m_{Z^0}$, the cross section for this process, neglecting the photon (Q_f^2) term, may be written as

$$\frac{d\sigma_{f\bar{f}}}{d\cos\theta} = B\left[1 + \cos^2\theta + \frac{8}{3}A_{FB}^{f}\cos\theta\right], \tag{2.9}$$

with B a normalisation constant. The Standard Model prediction for A_{FB}^{b} at $\sqrt{s} =$ 91.2 GeV, is 0.085 [17].[1] This is consistent with the previous LEP measurements:

$$\begin{aligned} A_{FB}^{b} &= 0.097 \pm 0.057 \pm 0.014 \quad \text{OPAL [18]} \\ A_{FB}^{b} &= 0.126 \pm 0.028 \pm 0.012 \quad \text{ALEPH [19]} \\ A_{FB}^{b} &= 0.161 \pm 0.060 \pm 0.021 \quad \text{DELHI [20]} \\ A_{FB}^{b} &= 0.130^{+0.044}_{-0.042} \quad \text{L3 [21].} \end{aligned}$$

Due to the s dependence of γ_0, the forward-backward asymmetry varies with the centre of mass energy, Figure 2.3 shows the predicted centre of mass energy dependence of the forward-backward asymmetry for b and c quarks.

At any value of $|\cos\theta|$, the forward-backward asymmetry may be measured as

$$\frac{N(+|\cos\theta|) - N(-|\cos\theta|)}{N(+|\cos\theta|) + N(-|\cos\theta|)} = \frac{8}{3}\frac{A_{FB}^{f}|\cos\theta|}{1 + \cos^2\theta}, \tag{2.10}$$

[1] Throughout this thesis, unless stated otherwise, all Standard Model values are derived using $m_{Z^0} = 91.175\ \text{GeV}/c^2$, $m_t = 132\ \text{GeV}/c^2$ and $m_{\text{Higgs}} = 300\ \text{GeV}/c^2$.

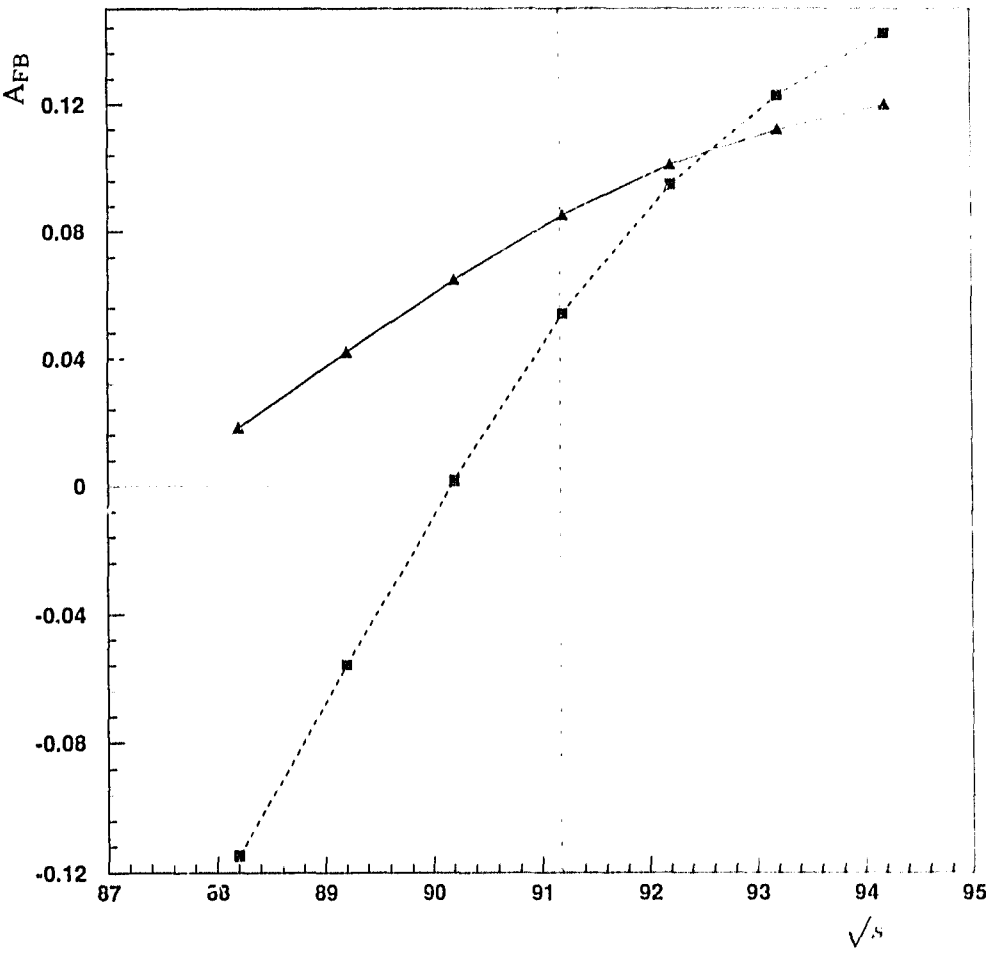

Figure 2.3: *The forward-backward asymmetry for b quarks (triangles, solid line) and c quarks (squares, dashed line) vs. the centre of mass energy. These curves are the Standard Model [17] prediction for a top mass of 132 GeV/c^2 and a Higgs mass of 300 GeV/c^2. $m_{Z^0} = 91.175$ GeV/c^2 is indicated.*

with $N(+|\cos\theta|)$ ($N(-|\cos\theta|)$) the number of fermions scattered at positive (negative) $\cos\theta$. The experimental sensitivity to the forward-backward asymmetry thus varies as $|\cos\theta|/(1+\cos^2\theta)$, and therefore it is important to extend the acceptance to as large values of $|\cos\theta|$ as possible.

The partial width of the Z^0 for each fermion is specified by the Standard Model. In lowest order of perturbation theory the partial width into fermion pairs is given, for energies $s \approx m_{Z^0}$, by [15]

$$\Gamma_{Z^0\to f\bar{f}} = \frac{\alpha}{3} N_c M_{Z^0} \left(v_f^2 + a_f^2\right). \tag{2.11}$$

$\frac{\Gamma_{Z^0\to b\bar{b}}}{\Gamma_{had}}$ has been measured to be

$$\frac{\Gamma_{Z^0\to b\bar{b}}}{\Gamma_{had}} = 0.226 \pm 0.008 \pm 0.018 \quad \text{OPAL [22]}$$

$$\frac{\Gamma_{Z^0\to b\bar{b}}}{\Gamma_{had}} = 0.193 \pm 0.006 \pm 0.011 \pm 0.021 \quad \text{OPAL [18]}$$

$$\Gamma_{Z^0\to b\bar{b}} = 385 \pm 7 \pm 11 \text{ MeV} \quad \text{L3 [23]}$$

$$\frac{\Gamma_{Z^0\to b\bar{b}}}{\Gamma_{had}} = 0.215 \pm 0.017 \pm 0.024 \quad \text{ALEPH [24]}.$$

All these results are consistent with the Standard Model prediction of $\Gamma_{Z^0\to b\bar{b}} = 376$ MeV [17]. Γ_{had} has been measured to be 1.740 ± 0.012 GeV [25].

It is important to note at this point that the above equations will be modified when higher orders of perturbation theory are considered. However no more degrees of freedom enter the theory in higher orders. The GSW theory makes only one prediction for any observable, any variation of these predictions arises purely from uncertainties in the calculations (finite orders, approximations) or in the input parameters. For the forward-backward asymmetry and partial width to b quarks, Figure 2.4 shows the allowed region of values at the Z^0 peak due to these uncertainties. The remaining freedom of the values comes mainly from the unknown mass of the top quark and the mass of the Higgs boson. A_{FB}^b is much more sensitive to the top quark mass than is the quantity $\Gamma_{Z^0\to b\bar{b}}$. This arises from the cancellation of some of the top quark mass dependence in diagrams that enter the calculation of $\Gamma_{Z^0\to b\bar{b}}$. Figure 2.5 shows the variation of $\Gamma_{Z^0\to b\bar{b}}$ and $\Gamma_{Z^0\to c\bar{c}}$ with the mass of the top quark. Since $\Gamma_{Z^0\to b\bar{b}}$ is much less sensitive to the mass of the top quark (m_t), a measurement of $\Gamma_{Z^0\to b\bar{b}}$ may test the Standard Model more precisely even when the mass of the top quark is unknown. In contrast A_{FB}^b is sensitive to the masses of the top quark and Higgs boson (Figure 2.6). This dependence makes A_{FB}^b a less reliable test of the model when these masses are not known, but a measurement of A_{FB}^b could provide an indication of possible values of the Higgs mass once the top mass in known.

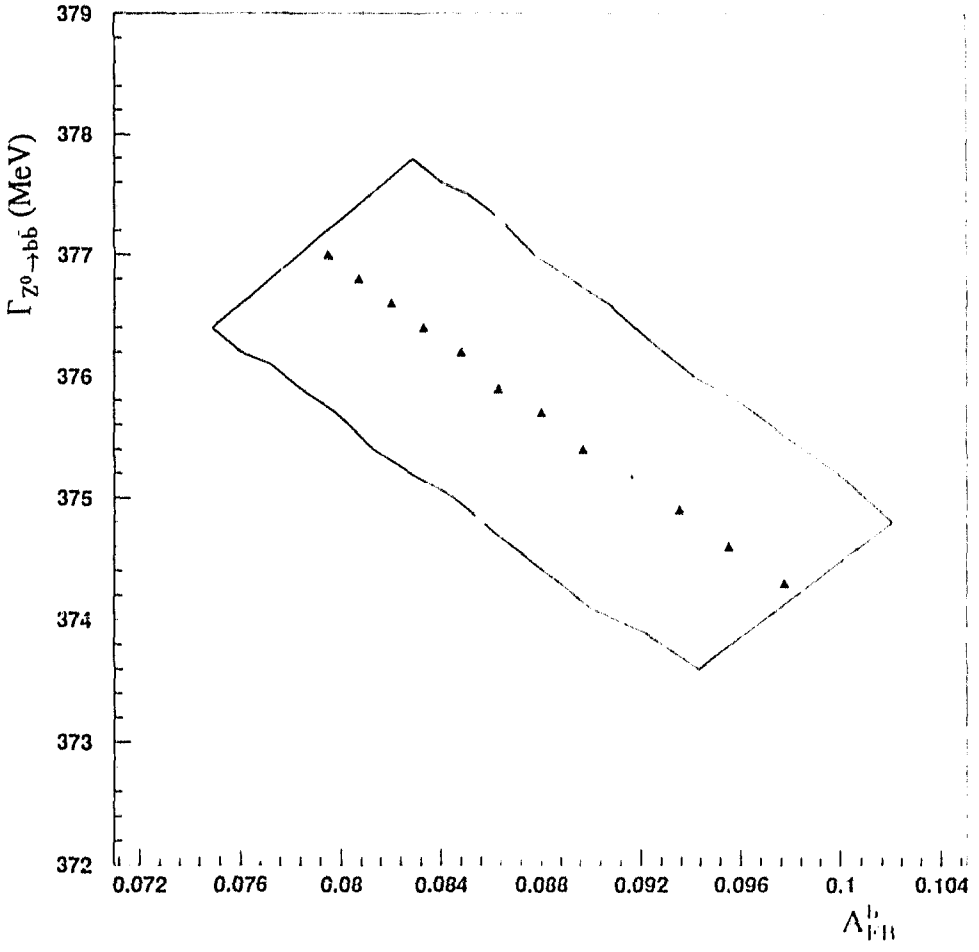

Figure 2.4: $\Gamma_{Z^0\to b\bar{b}}$ *vs.* A_{FB}^b *at* $\sqrt{s} = 91.2$ *GeV and* $m_{Z^0} = 91.175$ *GeV/c*^{2}. *The triangles correspond to a Higgs mass of 300 GeV/c*^{2}. *The upper curve is for a Higgs mass of 60 GeV/c*^{2} *and the lower curve is for a Higgs mass of 1000 GeV/c*^{2}. *The top mass varies between 80 GeV/c*^{2} *(top left) to 200 GeV/c*^{2} *(bottom right). The unevenness of the lines reflects the calculational uncertainties.*

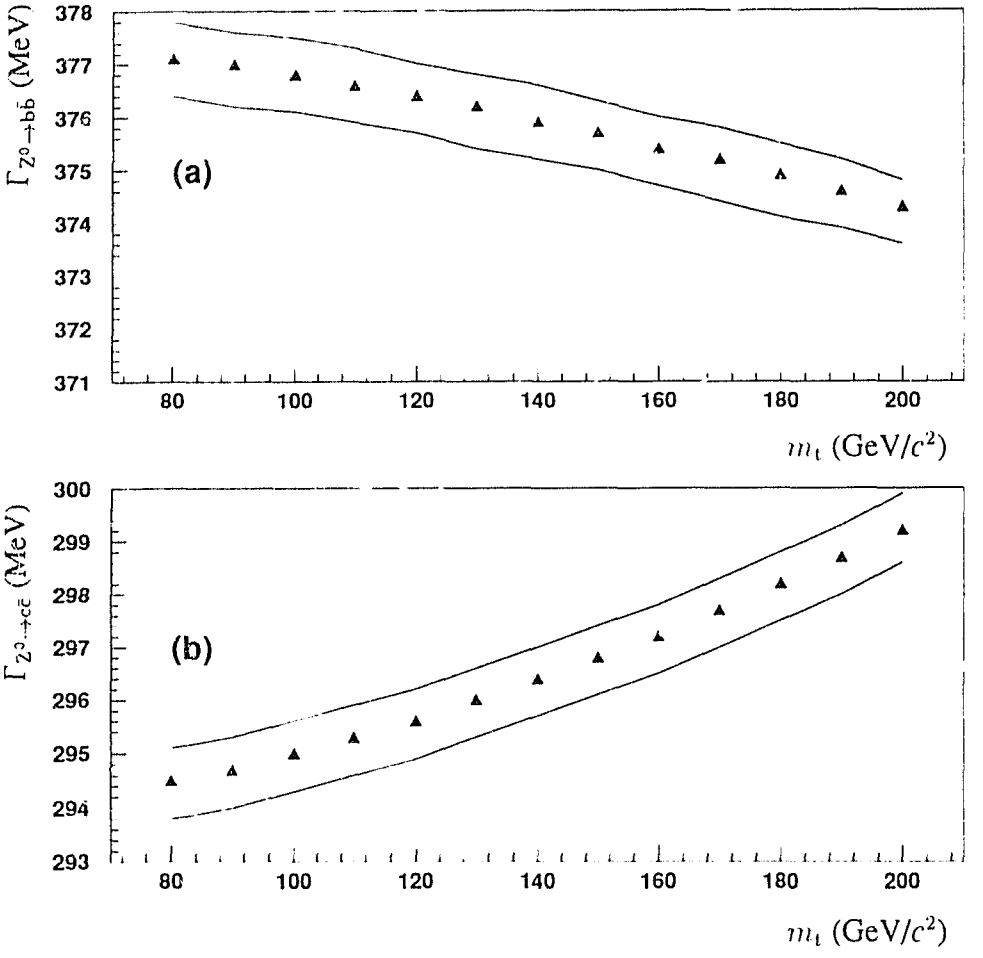

Figure 2.5: *(a)* $\Gamma_{Z^0\to b\bar{b}}$ *and (b)* $\Gamma_{Z^0\to c\bar{c}}$ *vs. the mass of the top quark* (m_t) *in the the Standard Model [17] with* $\sqrt{s} = 91.2$ *GeV and* $M_{Z^0} = 91.175$ *GeV/*c^2. *The triangles correspond to a Higgs mass of 300 GeV/*c^2, *while the upper curves are for a Higgs mass of 60 GeV/*c^2 *and the lower curves are for a Higgs mass of 1000 GeV/*c^2.

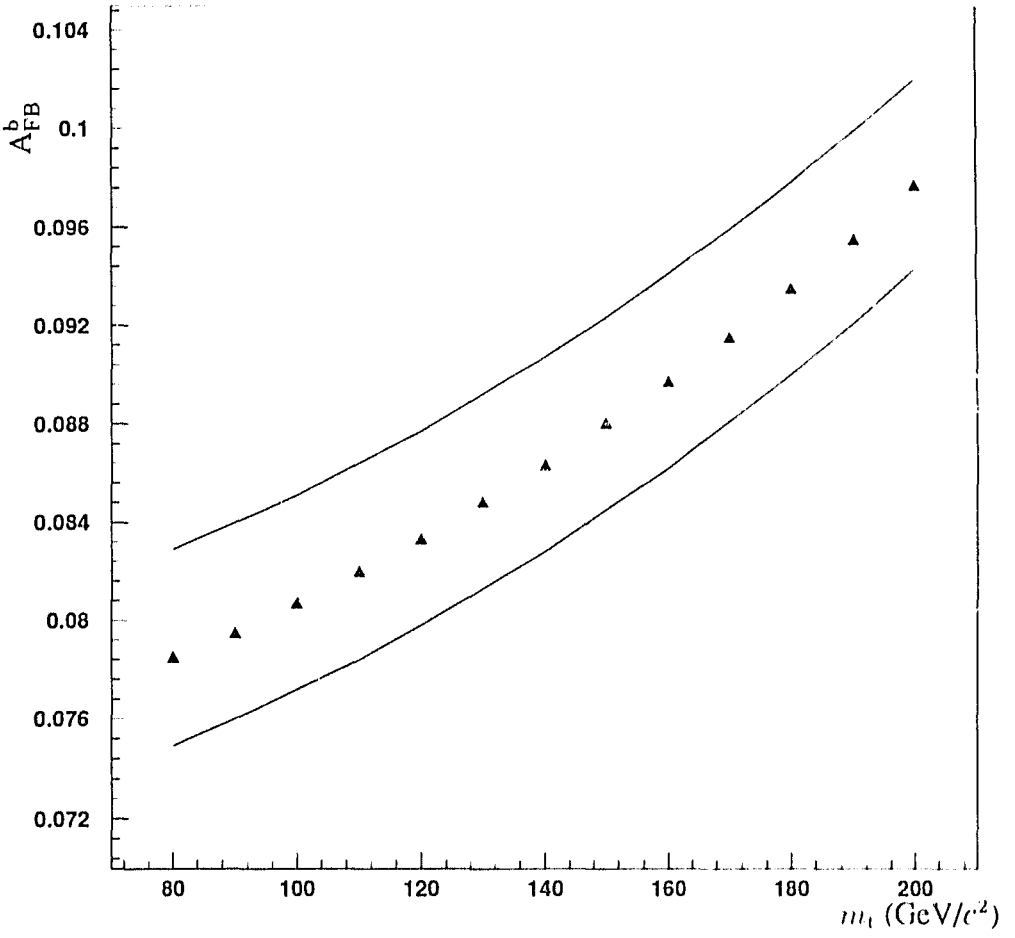

Figure 2.6: A_{FB}^{b} *vs. the mass of the top quark* (m_t) *in the the Standard Model [17] with* $\sqrt{s} = 91.2$ *GeV and* $M_{Z^0} = 91.175$ *GeV/*c^2. *The triangles correspond to a Higgs mass of 300 GeV/*c^2, *while the upper curve is for a Higgs mass of 60 GeV/*c^2 *and the lower curve is for a Higgs mass of 1000 GeV/*c^2.

2.2 b-flavoured Hadron Decays

The average b hadron lifetime has been measured by OPAL to be [26]

$$1.37 \pm 0.07(\text{stat}) \pm 0.06(\text{sys}) \text{ ps}. \tag{2.12}$$

With this average lifetime b-flavoured hadrons produced at the Z^0 travel approximately 2 mm before decaying, and therefore direct observation of b-flavoured hadrons in the detector is practically impossible. Identification of hadronic events that originate from $b\bar{b}$ quark pairs thus requires the identification of the b-flavoured hadron from its decay products in the detector.

The decays of hadrons containing heavy (b and c) quarks are most easily understood in the context of the so called "Spectator Model" [27]. This model makes the assumption that the decay of a hadron containing a heavy quark is the independent decay of the heavy quark via virtual W emission, with the other quarks in the hadron having no influence. After the heavy quark decays, all the remaining quarks form hadrons. Figure 2.7 shows the spectator decay $B^0_d \rightarrow e^+\nu_e D^-$. Decays of hadrons containing heavy quarks thus proceed via a chain of virtual W emission. When leptons are present in the decay products of the hadron, the decay is termed semileptonic (if the lepton is an electron the decay will be termed semielectronic). Any lepton that originates directly from b or c quark decays or from any of the three cascade processes will be termed a "prompt" lepton. Figure 2.8 shows that the decay chain of a b-flavoured hadron may result in two prompt leptons, while c hadrons may only produce one prompt lepton. The decay chains $b \rightarrow c \rightarrow e^+$, $b \rightarrow c \rightarrow e^-$ and $b \rightarrow \tau \rightarrow e^-$ are known as "cascade processes" and are shown in Figure 2.9. [2]

The branching ratio of a hadron (h_1) into electrons $B(h_1 \rightarrow e\overline{\nu_e}X)$ is given by

$$B(h_1 \rightarrow e\overline{\nu_e}X) = \frac{\Gamma_{h_1 \rightarrow e\overline{\nu_e}X}}{\Gamma_{h_1 \rightarrow \text{anything}}}, \tag{2.13}$$

the ratio of the partial width into electrons divided by the total width. The lifetime of a hadron is just the inverse of the total width and therefore

$$\frac{B(h_1 \rightarrow e\overline{\nu_e}X)}{\tau_{h_1}} = \Gamma_{h_1 \rightarrow e\overline{\nu_e}X}. \tag{2.14}$$

The relations in Equations 2.13 and 2.14 make no assumption on the actual decay mechanisms. Since spectator decays of the sort shown in Figure 2.7 are expected to be the dominant process in semileptonic decays of heavy quarks, the semielectronic

[2] Throughout this thesis, the charge conjugate processes are implied, e.g.: $b \rightarrow c \rightarrow e^+$ implies also $\bar{b} \rightarrow \bar{c} \rightarrow e^-$. When no distinction is to be made between $b \rightarrow c \rightarrow e^+$ and $\bar{b} \rightarrow \bar{c} \rightarrow e^-$ the symbol $b \rightarrow c \rightarrow e$ will denote both processes.

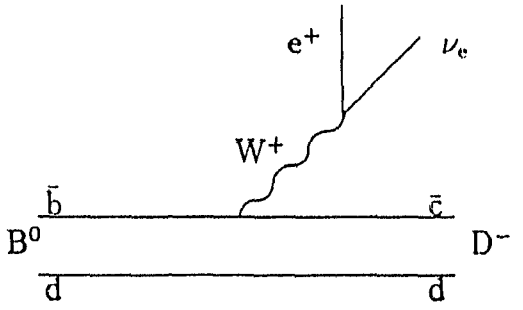

Figure 2.7: *The decay spectator decay* $B^0_d \rightarrow D^- e^+ \nu_e$.

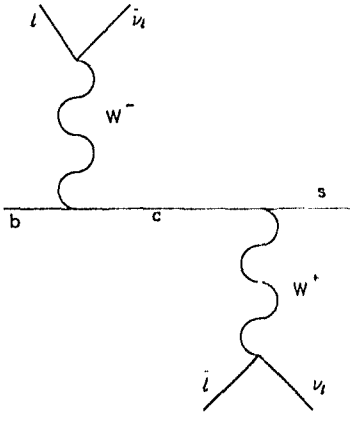

Figure 2.8: *Possible sources of prompt leptons from b quark decay. Note that b quark decay may result in two prompt leptons, while c decay can give only one.*

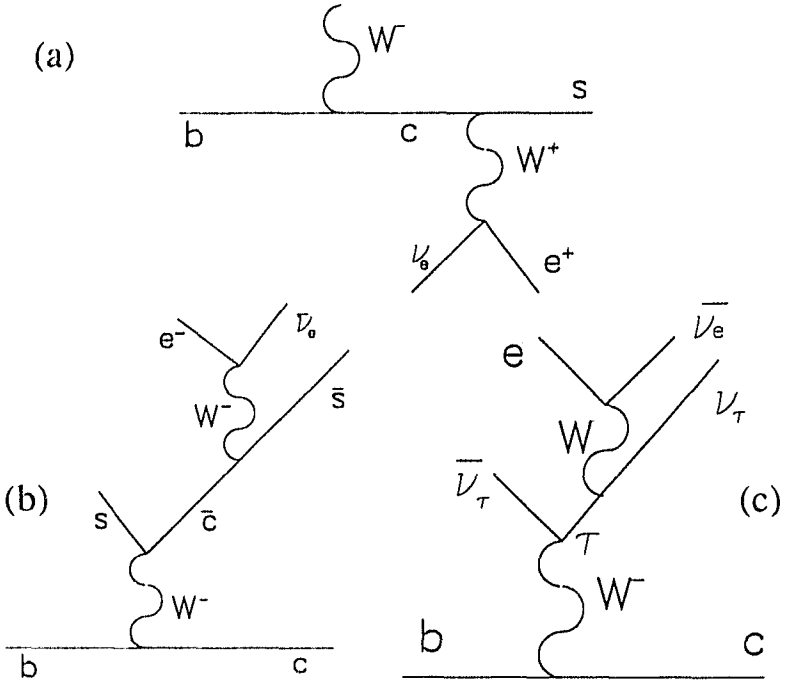

Figure 2.9: *The three cascade decays.* *(a)* $b \to c \to e^+$ *(b)* $b \to c \to e^-$ *(c)* $b \to \tau \to e^-$.

decay rates for two hadrons (h_1 and h_2) containing the same heavy quark should be equal; $\Gamma_{h_1 \to e\overline{\nu_e}X} \approx \Gamma_{h_2 \to e\overline{\nu_e}X}$. Using this expectation and Equations 2.13 and 2.14 the semielectronic branching ratios and lifetimes of two hadrons containing the same heavy quark should be related by

$$\frac{\tau_{h_1}}{\tau_{h_2}} = \frac{B(h_1 \to e)}{B(h_2 \to e)}, \tag{2.15}$$

regardless of whether the total decay width of the hadrons are equal or not. For the D system, the branching ratios and lifetimes are measured to be [28],

$$\tau_{D^0} = (4.21 \pm 0.10) \times 10^{-13} \text{ s} \tag{2.16}$$

$$\tau_{D^\pm} = (10.62 \pm 0.28) \times 10^{-13} \text{ s} \tag{2.17}$$

$$B(D^0 \to e^+ X) = (7.7 \pm 1.2)\% \tag{2.18}$$

$$B(D^\pm \to eX) = (19.2^{+1.7}_{-1.4})\%. \tag{2.19}$$

The ratio of these numbers support the idea that spectator processes dominate the semileptonic decays of these mesons.

The virtual W emitted in b quark decay may materialise as any of the pairs: $e^-\overline{\nu_e}$, $\mu^+\overline{\nu}_\mu$, sc, dc, du or su. Quigg and Rosner [29] have calculated the rates for these virtual W branchings, assuming that only $b \to cW^-$ occurs and $b \to uW^-$ does not, to be:

$$\Gamma(b \to ce^-\overline{\nu_e}) = \tfrac{2}{5}\Gamma_\mu \left(\tfrac{m_b}{m_\mu}\right)^5 f(m_c/m_b) \tag{2.20}$$

$$\Gamma(b \to c\mu^-\overline{\nu}_\mu) = \tfrac{2}{5}\Gamma_\mu \left(\tfrac{m_b}{m_\mu}\right)^5 f(m_c/m_b) \tag{2.21}$$

$$\Gamma(b \to c\tau\overline{\nu}_\tau) = \tfrac{2}{5}\Gamma_\mu \left(\tfrac{m_b}{m_\mu}\right)^5 g((m_c + m_\tau)^2/m_b^4) \tag{2.22}$$

$$\Gamma(b \to (c(du) + c(su))) = \tfrac{2}{5}3\Gamma_\mu \left(\tfrac{m_b}{m_\mu}\right)^5 f(m_c/m_b) \tag{2.23}$$

$$\Gamma(b \to (c(d\bar{c}) + c(sc))) = \tfrac{2}{5}3\Gamma_\mu \left(\tfrac{m_b}{m_\mu}\right)^5 g(4m_c^2/m_b^2). \tag{2.24}$$

The m_i are masses of the fermions and Γ_μ is a normalisation factor. The phase space factors $f(y)$ and $g(y)$ are given by:

$$f(y) = (1 - y')(1 - 8y^2 + y^4) - 12y^4 \ln y^2 \tag{2.25}$$

and

$$g(y) = (1 - 7y/2 - y^2/8 - 3y^3/16)(1 - y)^{1/2} + 3y^2(1 - y^2/16)\ln\left(\tfrac{1+\sqrt{1-y}}{\sqrt{y}}\right). \tag{2.26}$$

If the mass of the b quark is taken to be $m_b = 5.0$ GeV/c^2, the c quark mass is taken to be $m_c = 1.5$ GeV/c^2 and using the τ mass of $m_\tau = 1.7841$ GeV/c^2 then

$$\Gamma(b \to c(sc) + c(dc))/\Gamma(b \to cX) \approx 0.15. \tag{2.27}$$

This prediction has not been tested directly, however it can be shown to be plausible. The hadron formed by the charm quark from the decay $b \to cW^-$, will be assumed to decay to electrons with the branching ratio $B(c \to e^+) = 0.079$ [28], which is an average of low energy measurements with unknown mixes of charmed hadrons. The virtual W^- is predicted to branch into a c quark and a d-type quark 15% of the time. Due to the magnitudes of the quark mixing angles [28], cs is expected to dominate, hence it will be assumed that 15% of the time the virtual W^- forms a D_s^-. Hence $B(b \to c \to e)$ may be written as

$$B(b \to c \to e) \approx B(c \to e^+) + 0.15B(D_s^- \to e^-).$$

Using $B(D_s^- \to e^-) = 1.06B(D^0 \to e^-)$ (from Equation 2.15 using $\tau_{D_s^-} = 4.15 \times 10^{-13}$ s [28]), the prediction is $B(b \to c \to e) \approx 0.09$, which is in good agreement with the measured value of (0.097 ± 0.010) [30].

An expectation for the lepton momentum spectrum is needed to predict the efficiency for leptons from heavy quark decays to satisfy any kinematic requirements. Figure 2.10(a) shows the momentum of the electron in the decaying hadron rest frame for the decay $b \to e^-\overline{\nu}_e c$. This should be compared to the spectrum in Figure 2.10(b) for the decay $c \to e^+\nu_e s$. The large b–c quark mass difference results in a larger electron momentum endpoint. Angular momentum considerations also suggest that the electron takes a larger fraction of the available energy in b decay than in the corresponding charm decay (Figure 2.11). The electron in b decay will have the highest energy when it recoils against the anti-neutrino and the charmed quark. In the corresponding c decay this topology is not allowed for massless final state particles, due to the lefthanded nature of the charged current weak interaction. In the case of massive final state particles helicity considerations determine the electron momentum spectra shown in Figure 2.11.

The CLEO collaboration has reported measurements of the semileptonic branching ratios $B(b \to eX)$, $B(b \to c \to eX)$, at the $\Upsilon(4S)$ resonance using various decay models [30]. The CLEO collaboration considered the free quark model of Altarelli *et al.* (ACM) [31] (a spectator model) and two forms of the decay model of Isgur *et al.* [33]. The original model of Isgur *et al.* (ISGW) has, in principle, no free parameters and predicts that the decays $B \to De^+\nu_e X$, $B \to D^*e^+\nu_e X$ and $B \to D^{**}e^+\nu_e X$, occur at the rates 27%, 62% and 11% respectively. CLEO also considered a modified version of the ISGW model (ISGW**) in which the relative rates to D and D^* were held constant, but the branching ratio to D^{**} was increased to 32% of the total. This change in the $B \to D^{**}$ branching ratio improved the agreement with the CLEO data [30].

The CLEO collaboration's measurements of the branching ratios $B(b \to lX)$ and $B(b \to c \to lX)$ were obtained by fitting the observed lepton spectrum [30]. Figure 2.12 shows the measured electron spectrum, with the fit to the ACM model superimposed. The modelling of the semileptonic decay is important for

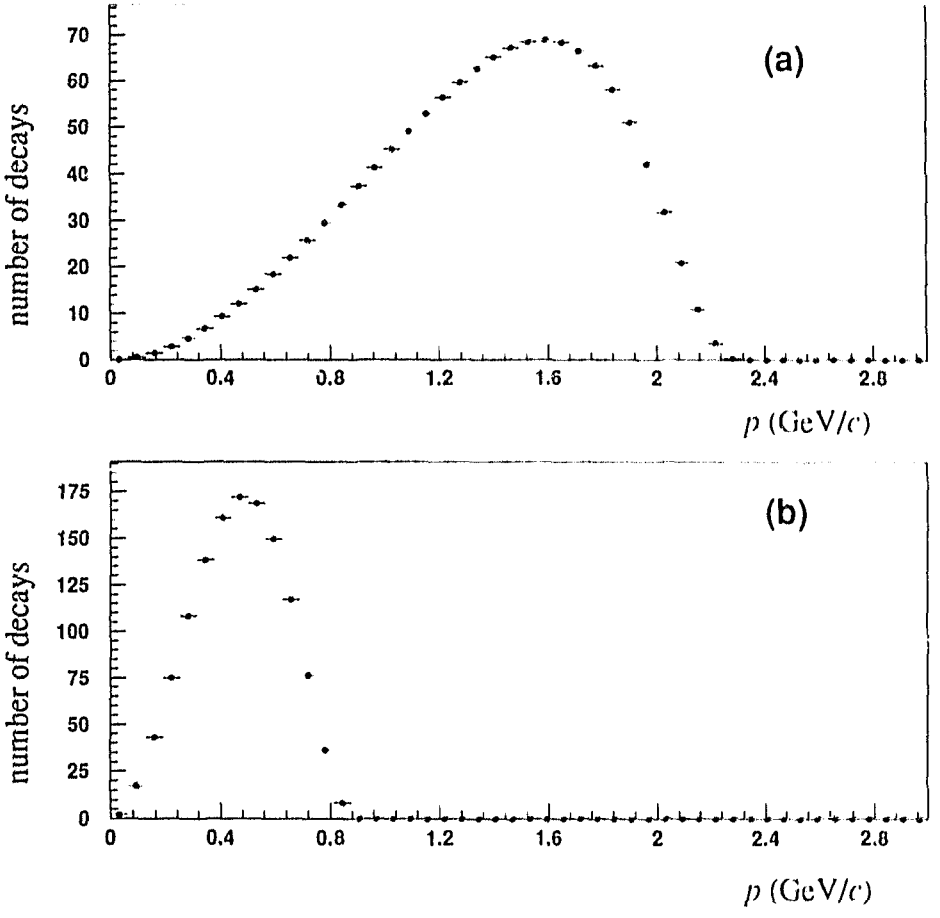

Figure 2.10: *(a) The electron momentum spectrum in the rest frame of the decaying b-flavoured hadron as predicted by the model of Altarelli et al. (ACM) [31]. (b) The electron momentum spectrum in the rest frame of the decaying c-flavoured hadron as predicted by the ACM model. The large b-c mass difference results in a larger possible electron momentum.*

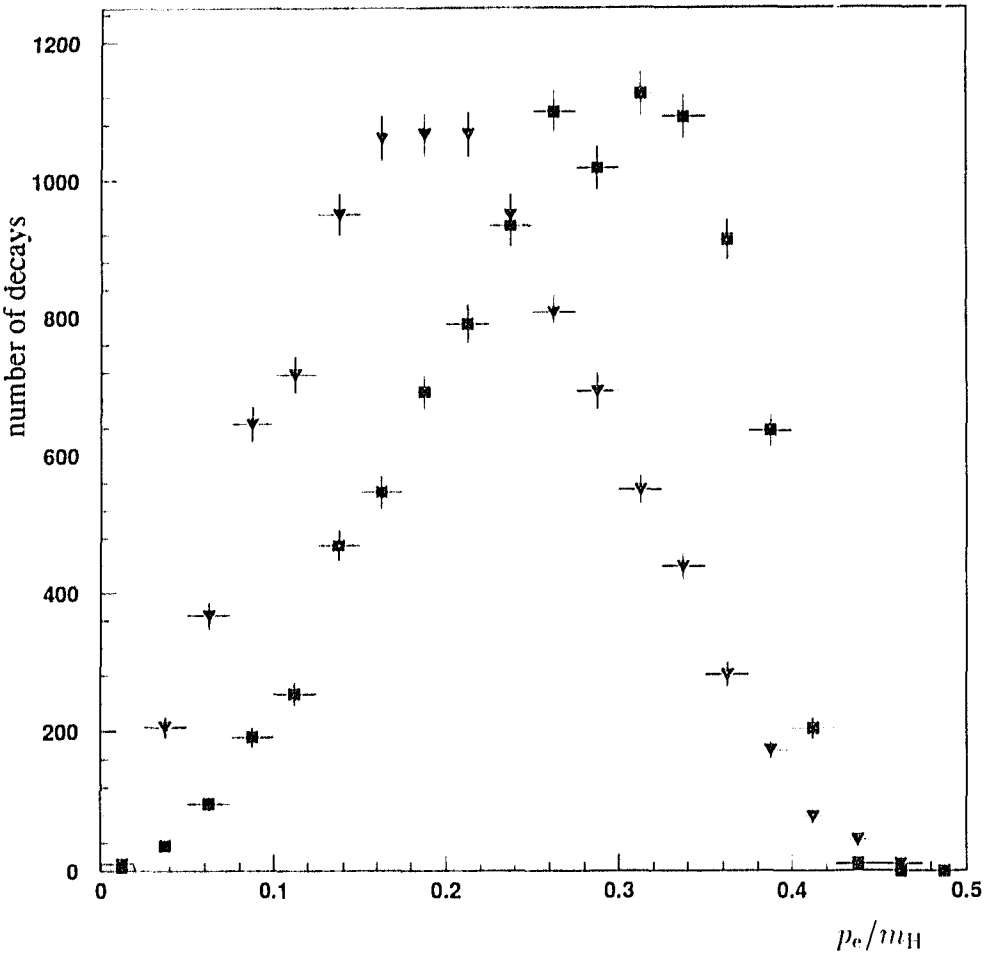

Figure 2.11: *The ratio of the electron momentum p_e in the parent rest frame to the parent mass (m_H) for $b \to e$ (squares) and $c \to e$ (triangles) as predicted by the JETSET Monte Carlo [32]. The different shapes of the two distributions can be understood by angular momentum considerations.*

extrapolation to regions of low electron momentum, which are not experimentally accessible and to separate direct b decays from cascade decays. Differences in the extrapolations result in different branching ratios. Figure 2.13 compares the momentum spectrum for semileptonic decays of B mesons in the B rest frame from the ACM and the ISGW** model. Table 2.2 shows the branching ratios obtained by CLEO in the context of these models [30].

	ISGW model	ACM model	ISGW** model
$B(\mathrm{b} \to l\nu_l\mathrm{q})\%$	$9.9 \pm 0.1 \pm 0.4$	$10.5 \pm 0.2 \pm 0.4$	$11.2 \pm 0.3 \pm 0.4$
$B(\mathrm{b} \to \mathrm{c} \to lX)\%$	$11.3 \pm 0.7 \pm 0.6$	$9.7 \pm 0.8 \pm 0.6$	$9.0 \pm 0.8 \pm 0.6$
$B(\mathrm{b} \to l\nu_l\mathrm{u})\%$	$0.06 \pm 0.08 \pm 0.03$	$0.28 \pm 0.12 \pm 0.03$	$0.27 \pm 0.10 \pm 0.02$

Table 2.2: *The semileptonic branching ratios measured by the CLEO collaboration at the $\Upsilon(4S)$ resonance [30] in the context of three semileptonic decay models. The branching ratio $B(\mathrm{b} \to l\nu_l\mathrm{q})$ includes the $\mathrm{b} \to l\nu_l\mathrm{u}$ contribution.*

At $\sqrt{s} \approx m_{Z^0}$, the efficiency for prompt electrons from b decay to satisfy any kinematic requirements is dominated by the energy spectrum of the parent b-flavoured hadrons (fragmentation), as shown in Figure 2.14. This is in contrast to measurements at the $\Upsilon(4S)$ resonance where the B mesons are produced nearly at rest and thus the lepton momentum spectrum is dominated by the decay spectrum. Since it is necessary to use semileptonic branching ratios determined at the $\Upsilon(4S)$ resonance and these branching ratios vary with the model of the lepton momentum spectrum used, it is necessary to take into account these correlations when calculating prompt electron kinematic efficiencies.

2.3 b Fragmentation

The process by which a $q\bar{q}$ pair evolves into a system of colourless hadrons is known as fragmentation, which is dominated by nonperturbative processes. A simplistic picture of the fragmentation process is that the colour lines of force between the two quarks are stretched and produce $q\bar{q}$ pairs that also move apart. This process can continue until no more energy is available to materialise $q\bar{q}$ pairs. The quarks produced in this manner then group into colourless states, which are the observed hadrons.

In this picture of fragmentation, quarks are most likely to group into hadrons if their velocities are equal. A heavy quark must lose very little energy to materialise a light quark with the same velocity. Therefore it is expected that hadrons containing a primordial heavy quark should carry more of the initial quark energy on average,

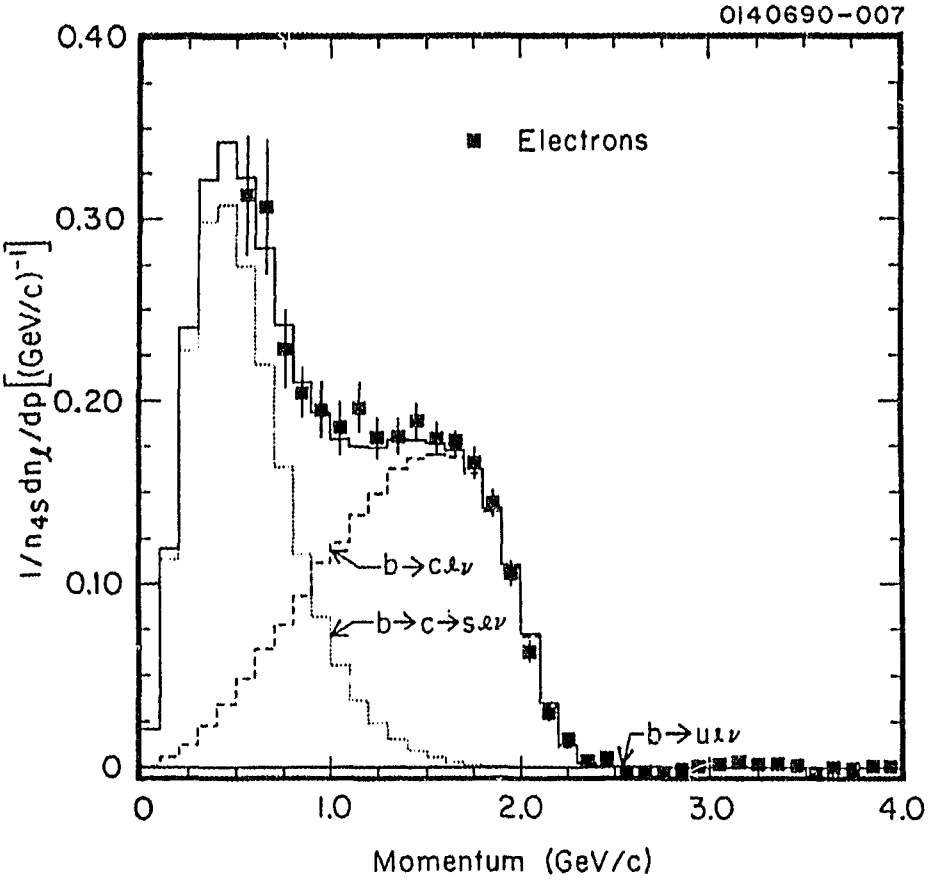

Figure 2.12: *The electron spectrum from* B *meson decays as measured by the CLEO collaboration at the* $\Upsilon(4S)$ *resonance [30]. The direct and cascade components, as predicted by the ACM model [31], are shown.*

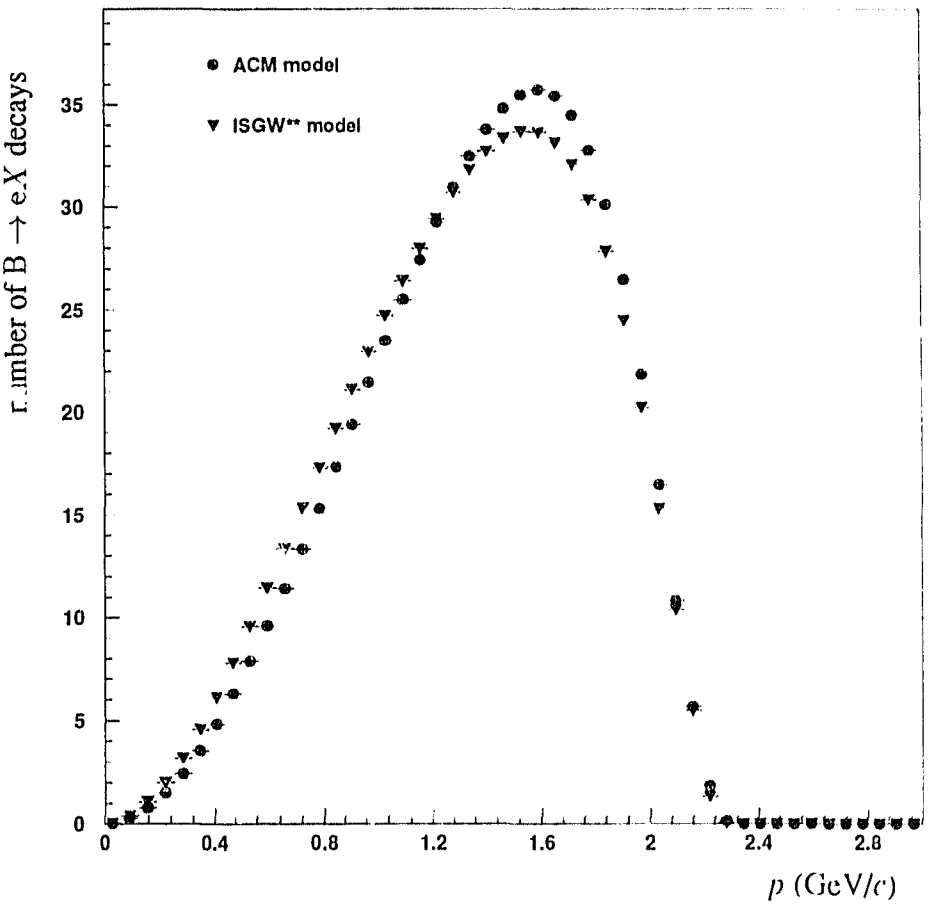

Figure 2.13: *The electron momentum in the decaying b-flavoured hadron rest frame as predicted by the ACM and ISGW** model.*

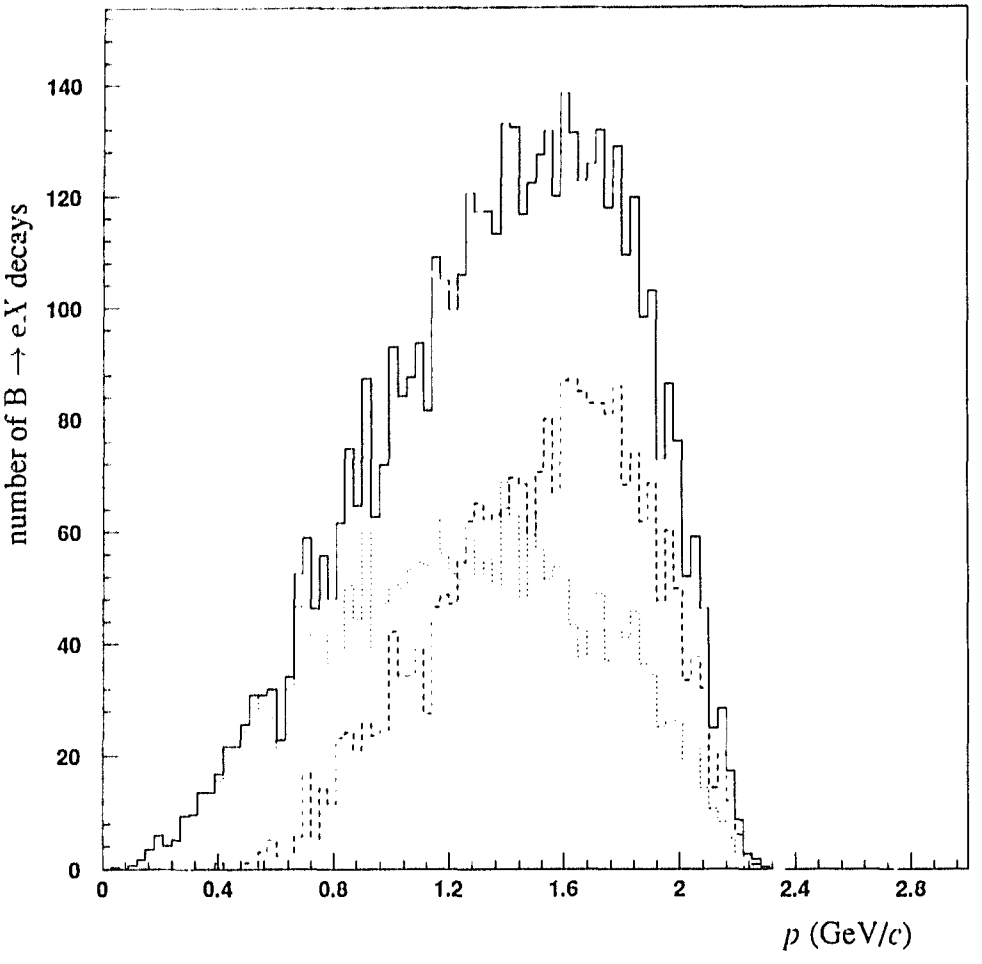

Figure 2.14: *The electron energy in the rest frame of the decaying* B *meson (solid line) separated into the electrons that satisfy the requirements; momentum greater than 2 GeV/c and and transverse momentum with respect to the jet axis greater than 0.8 GeV/c as discussed in Section 4.4, in the lab frame (dashed line) and those that do not (dotted line). The fluctuations in the* B *meson momentum in the lab frame dominate the probability that an electron will satisfy any kinematic requirement imposed in the lab frame.*

than a lighter quark. The tendency for heavy quarks to materialise into a heavy hadron with large energy is called "hard fragmentation". The fragmentation model of Peterson *et al.* [34] reproduces this feature of heavy quark fragmentation. This

hadron with large energy is called "hard fragmentation". The fragmentation model

model parametrises $D^{\rm H}(z)$, the probability of a hadron H having an energy $E^{\rm H}$ as

$$D^{\rm H}(z) = C z^{-1}\left(1 - \frac{1}{z} - \frac{\epsilon_{\rm q}}{1-z}\right)^{-2}. \qquad (2.28)$$

Here, $z = E^{\rm H}/E^{\rm q}$, the energy of the hadron divided by the initial energy of the heavy quark. $\epsilon_{\rm q}$ is the only free parameter (C is an overall normalisation). As $\epsilon_{\rm q}$ is decreased, the mean z increases.

As the energy of the quark is not measurable (it depends on radiation at the initial event vertex), what is determined experimentally is $\langle x_E\rangle_{\rm q}$, which is the energy of the hadron divided by the beam energy:

$$\langle x_E\rangle_{\rm q} = E_{\rm H}/\sqrt{s}/2. \qquad (2.29)$$

OPAL has measured $\langle x_E\rangle_{\rm b}$ and $\langle x_E\rangle_{\rm c}$ using prompt muons, to be [18]:

$$\langle x_E\rangle_{\rm b} = 0.726 \pm 0.007 \pm 0.022 \qquad (2.30)$$
$$\langle x_E\rangle_{\rm c} = 0.56 \pm 0.02 \pm 0.03. \qquad (2.31)$$

These measured values of $\langle x_E\rangle_{\rm q}$ correspond approximately to $\epsilon_{\rm q}$ values of

$$\epsilon_{\rm b} = 0.0035 \qquad (2.32)$$
$$\epsilon_{\rm c} = 0.053. \qquad (2.33)$$

The L3 and ALEPH collaborations have measured $\langle x_E\rangle_{\rm b}$ to be [23, 24]

$$\langle x_E\rangle_{\rm b} = 0.686 \pm 0.006 \pm 0.016 \qquad (2.34)$$
$$\langle x_E\rangle_{\rm b} = 0.67^{+0.04}_{-0.03} \qquad (2.35)$$

In addition, the ALEPH collaboration has measured $\langle x_E\rangle_{\rm c}$ to be [24]

$$\langle x_E\rangle_{\rm c} = 0.52^{+0.16}_{-0.15}. \qquad (2.36)$$

These measurements are consistent with those obtained by OPAL, and will be used to assess the uncertainty in these parameters.

When studying semileptonic decays of heavy quarks, it is not usually possible to reconstruct the parent hadron's direction. This difficulty is overcome by using the jet axis as an approximation to the parent hadron's direction. Figure 2.15 shows the difference between the jet axis and the hadron direction in simulated events. These simulated events suggest that the jet axis approximates the parent

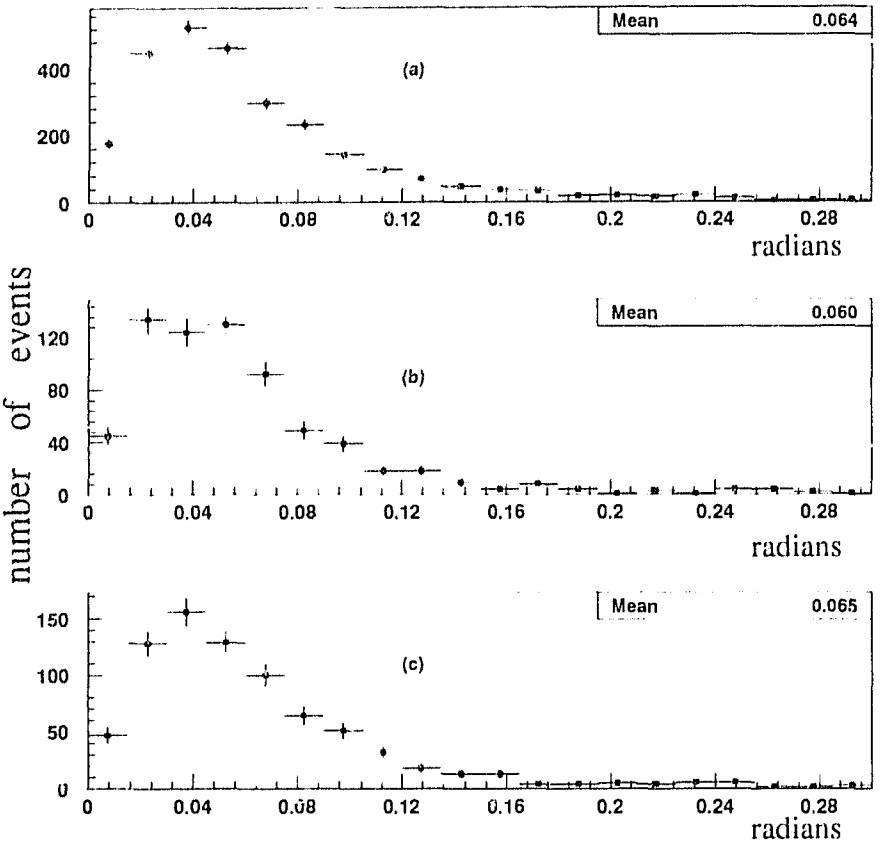

Figure 2.15: *The angle between the reconstructed jet axis and the parent hadron direction for simulated events containing a* $b \rightarrow c$ *decay. (a) is the difference for the angular range* $|\cos\theta|$ *less than 0.3, (b) corresponds to the range* $0.3 < |\cos\theta| < 0.6$ *and (c) to the range* $0.6 < |\cos\theta| < 0.9$. *The distributions do not peak a zero due to the missing neutrino in the* $b \rightarrow c$ *decay and the decreasing solid angle available at zero angle.*

hadron direction to approximately 60 mrad, for $|cos\theta_{jet}| < 0.9$. The procedure for finding jets experimentally will be addressed in Section 4.4.

The quark direction at the electroweak vertex is needed to measure the forward-backward asymmetry. Since the quark is never observed directly, it is necessary to approximate its initial direction. The quark direction could be approximated by the hadron (jet) direction, however a complication arises in events with more than two jets. These events are due to gluon radiation at the electroweak vertex and thus the thrust axis is used to approximate the initial quark direction.

The thrust axis is defined as the vector $\hat{T}$ that maximises :

$$\sum_i |p_i \cdot \hat{T}|, \tag{2.37}$$

with the sum over i implying all particles in the event. Figure 2.16 shows that for simulated data, the thrust axis represents the original quark direction with a resolution of less than 80 mrad for most polar angles.

An ambiguity exists in the choice for the sign of the z component of $\hat{T}$ ($\hat{T}_z$) and therefore the sign of $\cos\theta_{\rm thrust}$. To resolve this ambiguity for events containing a prompt lepton, the thrust direction is chosen as follows. The dot product $(p \cdot \hat{T})$ is formed, with p the momentum of the lepton. If this product is positive then the thrust direction is taken as

$$\cos\theta_{\rm thrust} = \hat{T}_z/|\hat{T}|, \tag{2.38}$$

if it is negative the opposite sign is chosen. The ambiguity in the quark direction is resolved by using the sign of the observed lepton. b quarks have charge $-\frac{1}{3}$, thus b quark semileptonic decay results in a negative signed lepton, hence the quark direction is thus chosen as

$$\cos\theta_{\rm q} = -Q\cos\theta_{\rm thrust}. \tag{2.39}$$

In this way the quark direction is signed correctly for b quarks that are tagged from a direct semileptonic decay. For c quarks this assignment results in the incorrect sign for $\cos\theta_{\rm c}$.

2.4 Summary

In this thesis the predictions of the Standard Model for the forward-backward asymmetry in the reaction $e^+e^- \to b\bar{b}$ and the partial width of the Z^0 boson into b quarks will be tested. It has been shown above that b quark production can be tagged through the presence of prompt electrons, which form approximately 10% of all b decays. By determining the sign of the prompt lepton, the quark direction at the electroweak vertex may be inferred. From the total number of

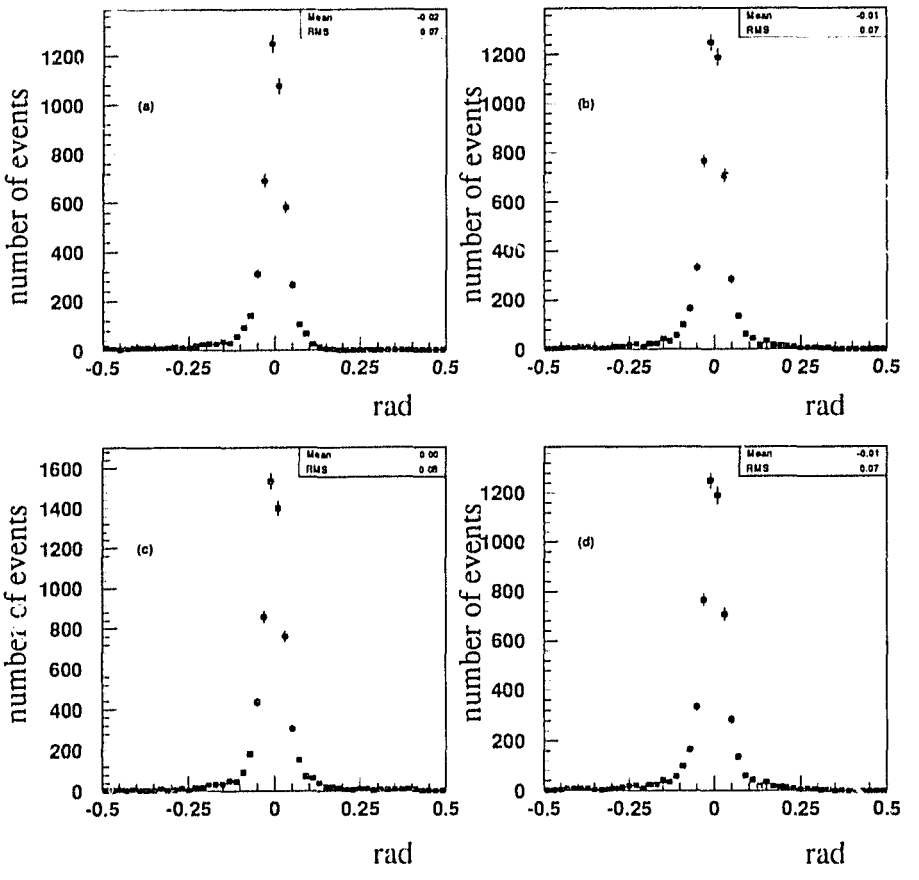

Figure 2.16: *The difference between the thrust axis and the initial* $q\bar{q}$ *direction for simulated events containing a* $b \to c$ *decay. (a) is the difference for the angular range* $|\cos\theta_{\rm thrust}|$ *less than 0.2, (b) corresponds to the range* $0.2 < |\cos\theta_{\rm thrust}| < 0.4$, *(c) is for the range* $0.4 < |\cos\theta_{\rm thrust}| < 0.6$ *and (d) is for the range* $0.6 < |\cos\theta_{\rm thrust}| < 0.9$.

observed prompt electrons and their angular distribution $\Gamma_{Z^0 \to b\bar{b}}$ and A_{FB}^b may be determined. In the following sections a set of selection crite ia developed to identify prompt electrons in multihadronic Z^0 decays is described. The resulting sample of prompt electrons will be used to obtain $\Gamma_{Z^0 \to b\bar{b}}$ and A_{FB}^b.

Chapter 3

The OPAL Detector

The OPAL detector has been described in detail in [9] and full descriptions of the subcomponents are given in the references contained in that publication. Only a brief description is given here.

The OPAL detector (Figure 3.1) is based around a 4.36 m diameter solenoidal magnet, providing a field of 0.435 T. The OPAL coordinate system is defined as follows; the z axis is along the e^- beam direction, the x axis is into the centre of the LEP ring and the y axis is perpendicular to both, forming a right handed coordinate system. The azimuthal angle (ϕ) is measured from the x axis around the z axis, while the polar angle (θ) is measured from the z axis. The origin of the coordinate system is the centre of the detector. The detector subcomponents are optimised to provide energy and momentum measurements and particle identification.

3.1 Central Tracking System

The OPAL central tracking system is comprised of three tracking detectors inside a solenoidal magnet (Figure 3.2). These detectors share the same gas mixture (88.2% argon, 9.8% methane and 2.0% isobutane), which is maintained at a pressure of 4 bar.

The innermost tracking detector, between radii of 88 mm and 235 mm is a 1 m long drift chamber (CV).[1] This chamber is optimised to provide a precise measurement of the $r - \phi$ origin of a track. Beginning at a radius of 1.9 m is a system of 4 m long chambers designed to measure precisely the z coordinate of a track (CZ). These chambers provide a z coordinate resolution of 100-350 μm in the range $44 \leq \theta \leq 136$.

The main tracking is provided by a large (approximately 4 m long) drift

[1] For the 1991 running period a silicon vertex detector was installed between CV and the beampipe. This detector was not used in this analysis.

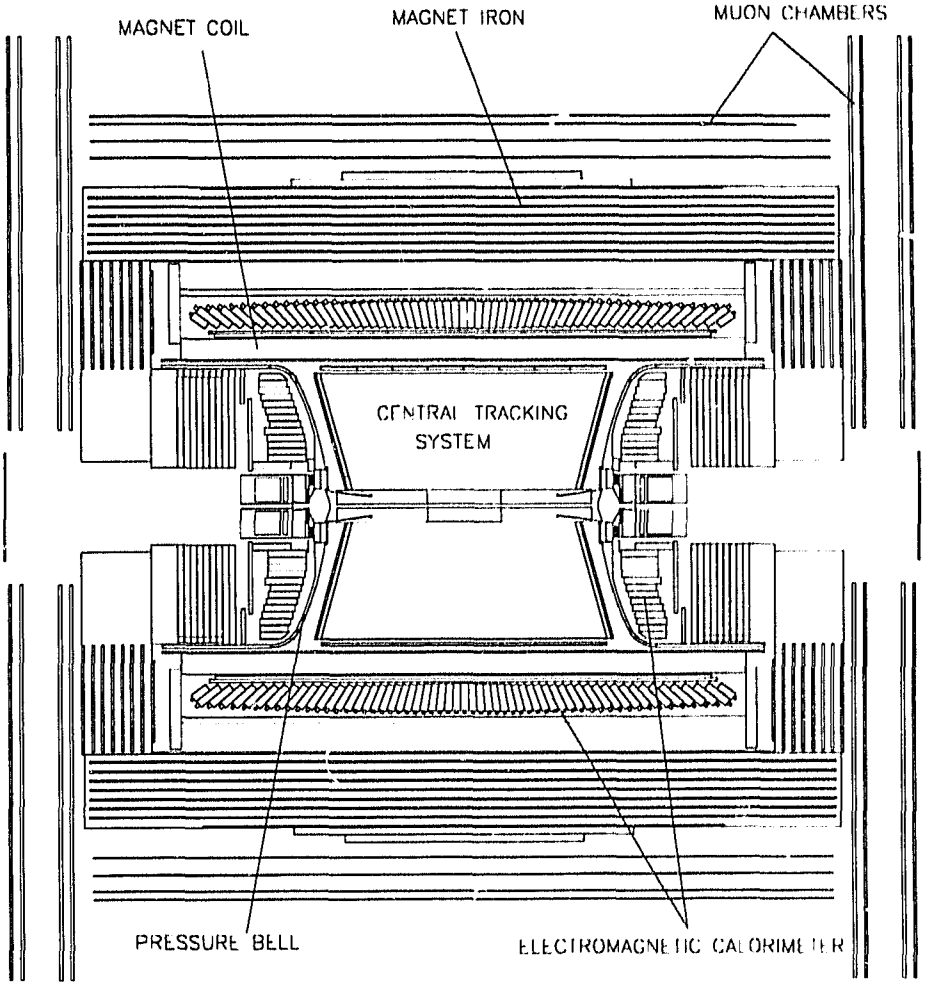

Figure 3.1: *A vertical section view of the OPAL detector with the major systems indicated.*

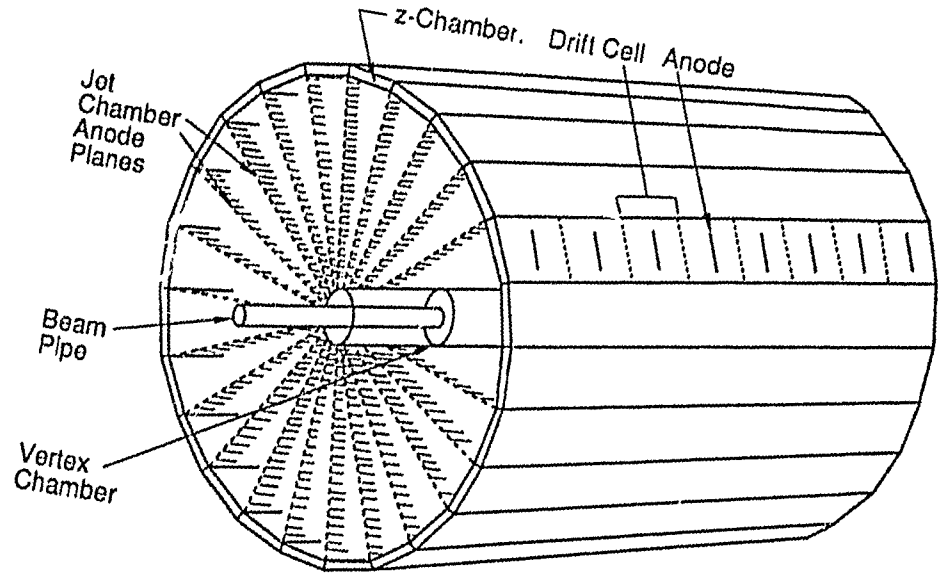

Figure 3.2: *The OPAL central tracking system (from [35]).*

chamber (CJ). This chamber has an inner radius of 250 mm, an outer radius of 1850 mm and is divided into 24 sectors in ϕ. Each sector in ϕ can provide up to 159 space points along a track. True space points of hits (r, ϕ, z) are measured by wire position, drift time and charge division. The intrinsic coordinate resolution has been determined to be 135 μm in $r-\phi$ and 6 cm in z [35]. The first anode wire is at a radius of 255 mm and the last is at a radius of 1835 mm, resulting in a 10 mm anode spacing. The wires are supported at each end of the chamber by conical supports of opening angle 15°. At track polar angles of $|\cos\theta| > 0.73$ a measurement of the z coordinate of a track upon exit of the chamber is possible. The z coordinate of the track endpoint is determined from the last $r-\phi$ hit on a track using the known z position of the hit wire at the conical support. Tracks that have a z coordinate measured in this way will be termed to have a CJ endpoint.

CJ also measures the energy loss to ionisation per unit length (dE/dx) of a particle as it traverses the chamber gas. The dE/dx measurement uses a truncated mean to compensate the tails in the Landau distribution. The 70% of samples with the smallest measured charges are used to calculate the dE/dx for a track. When 159 samples are used in the determination of dE/dx a resolution of approximately 3% is obtained. The 4 bar operating pressure was chosen partially to optimise the resolution of the dE/dx measurement.

The combined vertex resolution of all 3 detectors is estimated to be 40 μm in the $r-\phi$ plane and 6 cm in the z [35]. The CJ endpoint z measurement results in a polar angle resolution of 2.7 mrad [35]. In the region of active CZ acceptance, the momentum resolution, neglecting the small contribution from multiple scattering, is found to be [35]:

$$\frac{\sigma p}{p^2} = 1.5 \times 10^{-3} \ (\mathrm{GeV}/c)^{-1}.$$

In the range $0.815 < |\cos(\theta)| < 0.91$, where 159 samples in CJ are not possible, the momentum resolution is well described by [36]

$$\frac{\sigma p_t}{p_t} = \left[(0.02)^2 + \left(\frac{p_t}{0.03} \frac{\sigma_{r-\phi}}{L^2 B} \sqrt{\frac{750}{nhitcj + 4}} \right)^2 \right]^{1/2}.$$

Here p_t(GeV/c) is the momentum in the bending plane, B is the magnetic field (4.35 kG), L(m) is the radial track length and $nhitcj$ is the number of space points measured in CJ for the track. The factor $\sigma_{r-\phi}$ is the average single hit resolution and is 120 μm in this angular range. The 0.02 is the momentum-independent contribution from multiple scattering.

3.2 Electromagnetic Calorimeter

Outside the pressure vessel of tracking system (and after the magnet coil and the time of flight system (TOF), for $|\cos\theta| < 0.82$) is the electromagnetic calorimeter. Two distinct systems make up the electromagnetic calorimeter; a system of preshower counters (presampler) and a lead glass calorimeter. The material in front of the electromagnetic calorimeter is approximately 2 radiation lengths (X_0) thick which ensures that most electromagnetic showers will have started before entering the calorimeter.

The preshower counter system is divided into a barrel (PB), for $|\cos\theta| < 0.81$, and endcap (PE), for $0.83 < |\cos\theta| < 0.95$. The PB is constructed as a cylinder of two layers of limited streamer tubes. Each layer is read out by a system of strips, designed to give a precise position measurement of the electromagnetic shower. The pulse height on the strips also provides some information about the longitudinal energy deposit profile.

The lead glass calorimeter (ECAL) is divided into two separate detectors, the barrel (EB) in the range $|\cos(\theta)| < 0.82$ and the endcap (EE) covering $0.81 < |\cos\theta| < 0.95$. Both detectors are Čerenkov shower counters made up of blocks of lead glass. Since the EB and EE are very similar in operation and EE is used to develop the prompt electron selection described in Chapter 5, only EE will be described in detail here.

The endcap calorimeter (EE) (Figure 3.3) consists of 2264 lead glass blocks (CEREN 25 [37]) of dimensions $9.2 \times 9.2 \times 52.0$ cm. At each end of OPAL in z, 1132 blocks are arranged in a disk surrounding the beampipe. The block medians are parallel to the beam (z) axis and, for tracks originating from the centre of the detector, the EE presents approximately $22X_0$ of material. This "non-projecting" geometry of the EE will be exploited in the work described here.

Identification of localised energy deposits in the calorimeter is necessary to make associations between charged tracks and energy deposits. This clustering is a two step process, the first step is to create "coarse" clusters. The algorithm to create the "coarse" clusters is as follows. A block with energy greater than 60 MeV is identified (seed block)[2]. All of the blocks touching the seed block with energy greater than 40 MeV are grouped with this seed block to form a cluster. Each touching block that has energy above 60 MeV is then used in turn as the seed block and the process is repeated. This process continues until no blocks can be added to the cluster in this way. Once a "coarse" cluster is thus finished, the next unassigned block with energy above 60 MeV is used to start a new cluster. This procedure is continued until no more seed blocks are available.

It is possible that these "coarse" clusters contain many separate energy deposits

[2]The RMS noise in EE is approximately 14 MeV. Hence blocks with energy larger 60 MeV are at least three σ above the noise level.

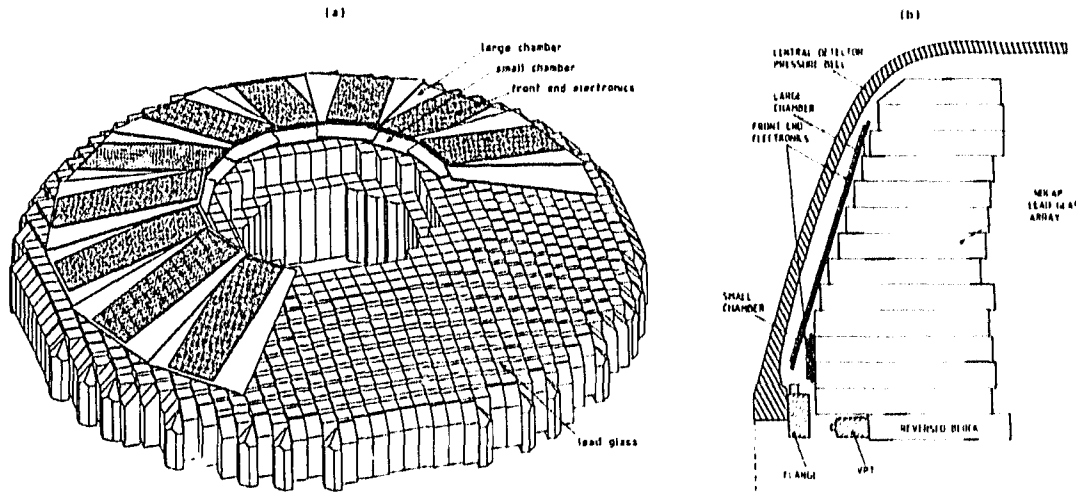

Figure 3.3: *The endcap calorimeter showing how the endcap preshower counter is mounted on the lead glass array (from [38]). (b) shows the endcap electromagnetic calorimeter mounted behind the pressure bell of the central tracking detectors.*

and hence a further splitting into "fine" clusters is performed. The process of creating the "fine" clusters tries to identify valleys in the energy deposit of the coarse cluster.

To begin, the blocks within a "coarse" cluster are ordered by energy. In decreasing order of energy, each block not already assigned to a "fine" cluster, is considered in turn (present block). The block with the largest energy that touches the present block is found. If this largest neighbour block is already in a "fine" cluster and its energy is larger than the present block's energy, the present block and all the blocks touching the present block are assigned to the "fine" cluster that already contains this neighbour. Otherwise a new "fine" cluster is started containing the present block and all its neighbours. This process is repeated until all blocks in the "coarse" cluster are assigned to a "fine" cluster. Figure 3.4 shows a coarse cluster and two fine clusters found within it. The term 'cluster' will henceforth be used to refer to these "fine" clusters. The energy associated with the cluster at this stage is termed the "raw cluster energy".

The pressure vessel for the central detector adds approximately $1.5X_0$ in front of the calorimeter. Therefore the measured energies need to be corrected to account for the energy loss in this dead material. This correction is calculated for each

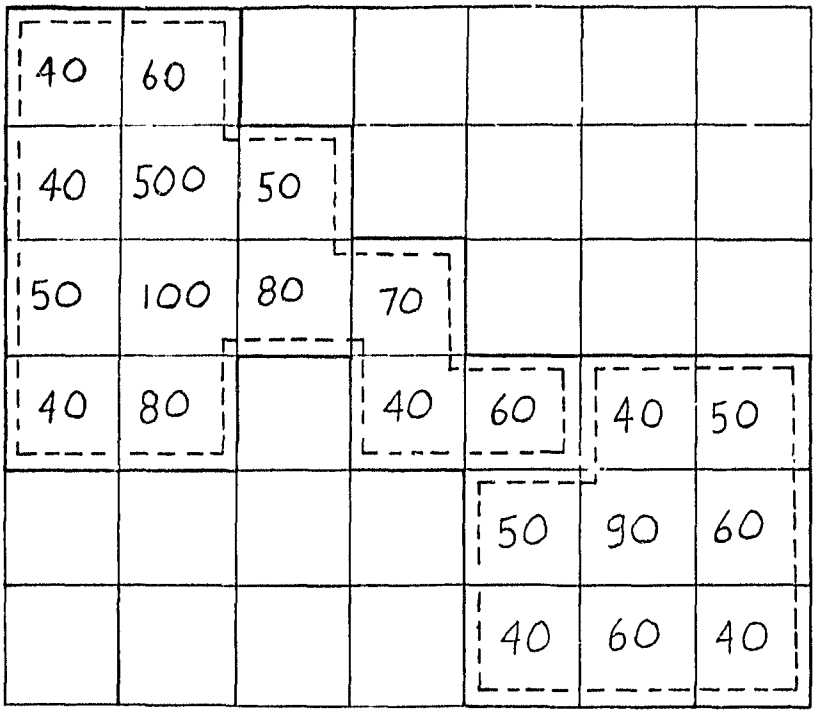

Figure 3.4: *An example of a "coarse" cluster split into two "fine" clusters, using the algorithm described in the text. The "coarse" cluster consists of all blocks with marked energies (in MeV). The two "fine" clusters are shown with dashed lines.*

cluster of energy assuming that the cluster was created by an electron [3]. The resulting energy resolution of the EE has been measured to be

$$\frac{\delta E}{E} = 0.025 \oplus \frac{0.16}{\sqrt{E}},$$

with E(GeV) the measured energy. The raw cluster energy corrected for the material in front of the calorimeter is termed the "cluster energy".

3.3 Muon System

Outside the electromagnetic calorimeter is the iron of the magnet return yolk. The magnet iron serves as an absorber (8-14 interaction lengths), which acts as a filter for muons, allowing them to be identified by their ability to penetrate this material. In the region $0.67 < |\cos\theta| < 0.98$ there is a system of limited streamer tubes that measures the positions of tracks penetrating the magnet iron. (A similar system exists at larger angles). These muon detectors provide up to 4 space points on each muon with resolutions of $\sim$ 1 mm in x-y and 5 mrad in polar angle.

3.4 The OPAL Trigger System

The OPAL trigger system [39] provides a redundant and efficient trigger for all Z^0 decays. It is based on a matrix of $\theta - \phi$ bins covering the entire detector, and has been measured to be 100% efficient for selecting hadronic decays of the Z^0 [16]. The basic trigger elements are described below.

CV and CJ provide a fast measurement of the $r - z$ coordinates of hits in bins of θ and ϕ. Tracks are identified as straight lines in $r - z$, thus enabling a track based trigger decision.

The time of flight counters, outside the magnet coil, provide trigger signals in 21 bins of ϕ. These signals are used in coincidence with other signals to form trigger decisions.

The electromagnetic calorimeter (both EB and EE) is divided into 6 θ bins and 24 overlapping ϕ bins. Trigger signals are formed from analogue energy sums in these bins.

Some trigger conditions relevant for multihadronic events (any of which alone will cause a trigger) are:

- $>$ 3 tracks

[3] For $|\cos\theta| \approx 0.85$ this correction increases the raw cluster energy by a factor of approximately 1.33, for energies between 4 and 10 GeV.

- $\geq$ 2 tracks in the barrel region
- track trigger-TOF coincidence in ϕ
- track trigger-ECAL coincidence in $\theta - \phi$
- TOF-ECAL coincidence in ϕ
- $\geq$ 7 TOF ϕ hits
- $\geq$ 7 GeV total energy in EB
- $\geq$ 6 GeV total energy in EE
- $\geq$ 2.6 GeV in a $\theta - \phi$ bin in EB
- $\geq$ 3 GeV in a $\theta - \phi$ bin in EE

3.5 Event Reconstruction System

The final stage of the OPAL data acquisition system [40] is a second level trigger and classification system (filter) [41]. The filter writes the triggered events to disk in files (partitions) of approximately 20 Mbyte. These partitions are copied from the filter to an optical disk for permanent storage and distributed to a system of APOLLO DN10000 computers that form the online reconstruction system [40]. An individual DN10000 processes the events in a partition through four parallel running copies of the OPAL event reconstruction program. The events are reordered onto a local disk of the DN10000 and moved to external computer systems.

The online reconstruction system takes full advantage of the capabilities available in modern low cost workstations. The services of the operating system, such as the file system, event scheduling and external communications were exploited to make a system that is easily expandable and easily maintained. Reconstructed events are typically available for analysis and detector monitoring less than one hour after the event is triggered.

Chapter 4

Event Selection

4.1 Hadronic Event Selection

The OPAL selection of hadronic events uses a combination of tracking and calorimetric requirements. Reconstructed tracks and energy clusters must pass certain quality requirements to be considered in the event selection. For tracks to be considered they must have greater than 19 measured space points in CJ and a distance of closest approach to the event vertex of less than 2 cm in the $r - \phi$ plane and less than 40 cm in z. Tracks must also have a momentum component in the bending plane of at least 50 MeV/c. Energy clusters are required to have at least 100 MeV in EB and at least 200 MeV in EE. For an event to be classified as a hadronic decay of the Z^0 the following criteria must be satisfied:

- ≥ 6 energy clusters
- ≥ 5 tracks
- The sum of all electromagnetic cluster energies must be greater than 10% of the centre of mass energy ($\sqrt{s}$)
- $\frac{|\sum(E_{clus}\cos\theta)|}{\sum E_{clus}} < 0.65$

where θ is the polar angle of the electromagnetic cluster. The last requirement rejects events with a large energy imbalance in z, thus discriminating against events that are not due to e^+e^- collisions. Figure 4.1 shows a selected multihadronic event.

This hadronic selection has an acceptance of 98.4% for hadronic decays of the Z^0 [16]. The fraction of events accepted by the selection that is not due to hadronic Z^0 decays is estimated to be 0.2%, arising equally from the reaction $e^+e^- \rightarrow Z^0 \rightarrow \tau^+\tau^-$ and 2 photon events ($e^+e^- \rightarrow e^+e^-X$).

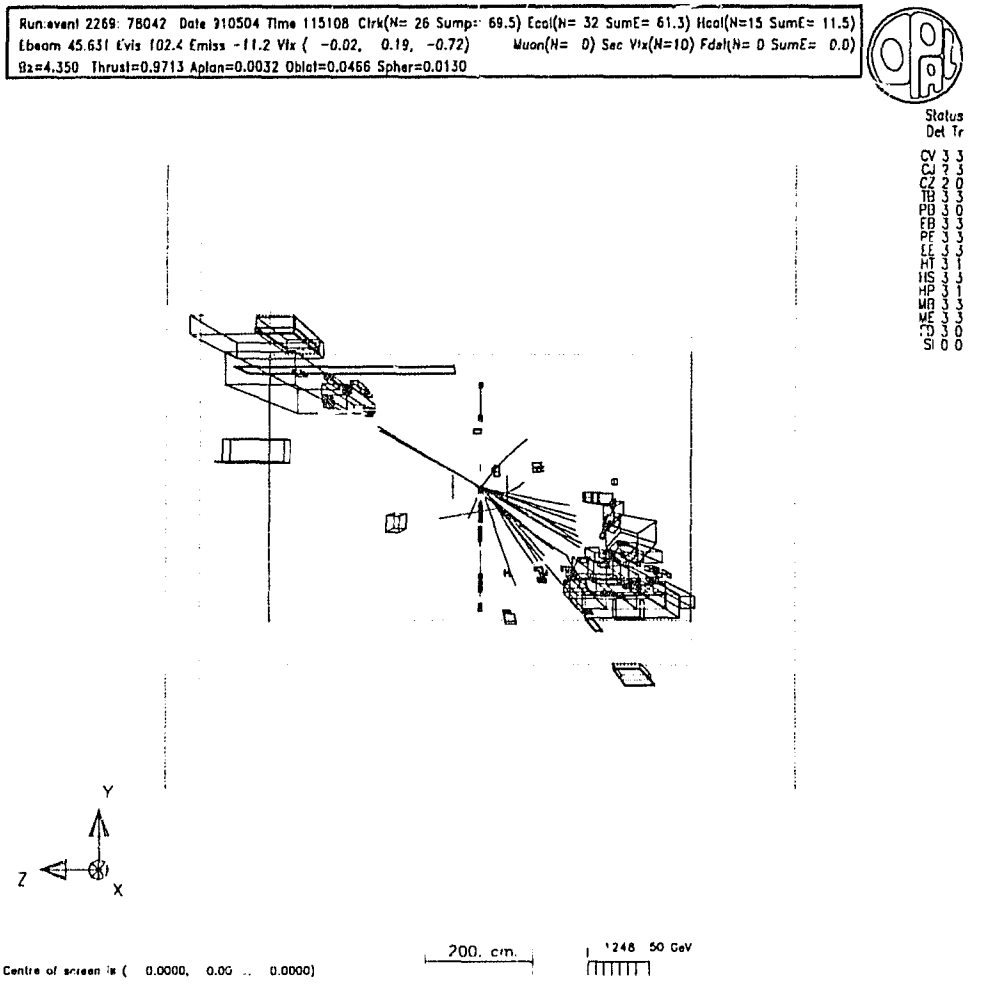

Figure 4.1: *An event selected as a multihadronic Z^0 decay as described in the text. The complicated nature of such events is evident.*

4.2 Single Electron Selection

For efficiency calculations it is desirable to have a set of events that contain only one particle in the detector, with that particle being an electron or a positron. This class of events may arise from the reactions $e^+e^- \to e^+e^-\gamma$ or $e^+e^- \to e^+e^-X$, where only the electron or positron is detected. To select events of this type the following requirements were imposed. The event was required to contain only one track that had a distance of closest approach to the vertex in the $r-\phi$ plane of less than 6 mm and no more than 30 cm in z. Requiring that the track did not match any reconstructed segment found in the muon chamber suppressed muon background. An electromagnetic energy deposit of greater than 200 MeV was required within a cone of opening angle of 200 mrad around the track. The energy deposit of a minimum ionising particle in EE is approximately 200 MeV. Events with electromagnetic clusters of energy greater than 500 MeV at angles greater than 200 mrad from the track were rejected. This requirement served to eliminate events with many particles but only one track satisfying the track quality requirements. With these cuts a fairly pure sample of electrons was obtained, with only a slight non-electron contamination below momenta of 4 GeV/c. Figure 4.2 shows an event selected in this manner.

4.3 Inclusive Muon Selection

Since the sources of prompt muons and prompt electrons are identical, prompt muons are useful in assessing effects that depend on activity surrounding the prompt lepton. A sample of muons in multihadronic events (inclusive muons) was obtained to study these effects. The ability of muons to penetrate the magnet iron and register in the muon chambers was the basis of the muon selection. The goodness of a match in position of a track segment found in the muon chambers and the extrapolated track impact point, obtained from the central tracking system, was used as the discriminating variable. Specifically a requirement was imposed on the variable χ_{pos}, defined as [42]:

$$\chi^2_{pos} = \frac{(\Delta\phi_{pos})^2}{\sigma(\Delta\phi_{pos})^2} + \frac{(\Delta\theta_{pos})^2}{\sigma(\Delta\theta_{pos})^2}, \tag{4.1}$$

where $\Delta\phi_{pos}$ ($\Delta\theta_{pos}$) was the difference between the extrapolated impact point and the reconstructed muon segment in ϕ (θ). The resolutions $\sigma(\Delta\phi_{pos})$ and $\sigma(\Delta\theta_{pos})$ include the various sources of errors possible in the positional match (multiple scattering, momentum mis-measurement, survey errors, etc.).

A purer muon sample results when the upper limit of accepted χ_{pos} values is decreased. It has been estimated [42] that a requirement of $\chi_{pos} < 3$ results in

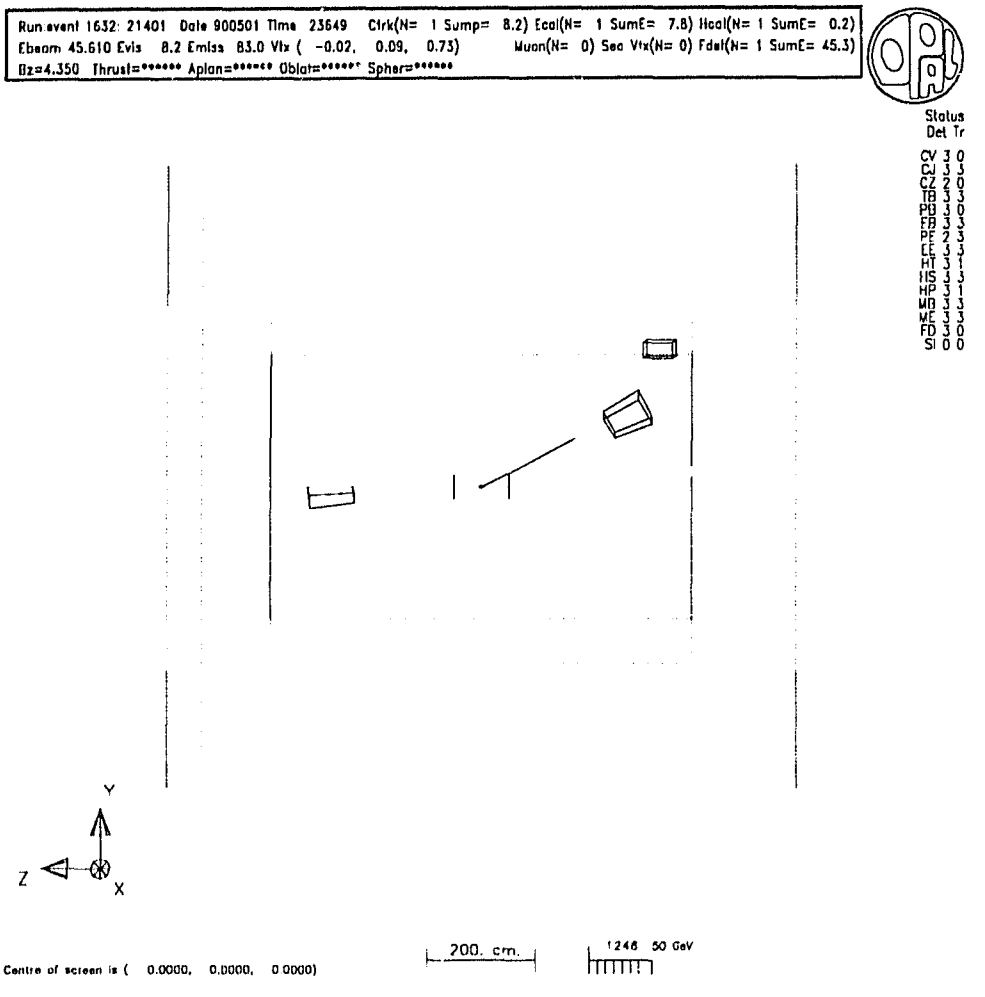

Figure 4.2: *An event selected to be a single electron using the procedure described in the text. The event has one track of momentum 8.2 GeV/c, matched to an EE cluster of 7.8 GeV. On the opposite side of the detector to this track in z, the forward luminosity calorimeter (which is not considered in the selection) registered an energy of 54.3 GeV. Noise of 192 MeV is seen in the hadron calorimeter.*

a selection of prompt muons with 48% purity and a more stringent criterion of $\chi_{pos} < 2$ results in a purity of 55%.

4.4 Jet Definition

Jets were derived using "good" tracks (defined in Section 5.1) and electromagnetic calorimeter clusters (ECAL clusters) not associated to "good" tracks. Unassociated ECAL clusters were required to satisfy the following quality requirements:

- The raw cluster energy must have been greater than 50 MeV. This removed clusters that were due to electronic noise.
- The cluster energy was required to exceed 100 MeV in the barrel electromagnetic calorimeter and 200 MeV in the endcap electromagnetic calorimeter.
- The reconstructed cluster must not have contained a region of the detector that was known to have a large amount of electronic noise.

The different energy thresholds for the EE and the EB clusters reflect the different noise levels in these detectors. The main source of unassociated ECAL clusters was assumed to be photons, from the decay of short lived neutral particles (π^0, η,...), with an energy equal to the cluster energy and originating from the event vertex.

To proceed with the jetfinding, an event was required to contain at least five good tracks. This is a stricter requirement than that used in the hadronic event selection, since the definition of "good" tracks is more demanding than the track selection used for the hadronic event selection. This requirement of at least five "good" tracks was estimated, using simulated data, to have an efficiency greater than 99.7% efficient for bb events.

The jet definition was based on the jetfinding algorithm developed by the JADE experiment [43] which uses a "scaled mass variable". This method of combining particles into jets employs the "E0 recombination scheme" developed by OPAL [44]. This algorithm considers all particles in turn and forms an invariant mass squared

$$y_{lm} = (p_l^\mu + p_m^\mu)^2. \tag{4.2}$$

If the invariant mass squared (y_{lm}) of a pair is smaller than some value y_{min} the two particles are combined into a pseudo-particle (n) using the prescription

$$\begin{aligned} E_n &= E_l + E_m \\ p_n &= \frac{E_n}{|p_l + p_m|} \cdot (p_l + p_m). \end{aligned} \tag{4.3}$$

The p_n is scaled by $\frac{E_n}{|p_l+p_m|}$ so that the pseudo-particle n has zero invariant mass (the origin of the name E0). The recombination process is repeated until no

pseudo-particles may be formed in this manner. The jet momenta are then equal to the momenta of the remaining pseudo-particles. The value of $x_{\min}$ used in this analysis was 49 $(\mathrm{GeV}/c^2)^2$.

The momentum component transverse to the jet axis, of any track associated to that jet, was given by:

$$p_T = |\frac{p \times p_{\mathrm{jet}}}{|p_{\mathrm{jet}}|}|. \tag{4.4}$$

Here p is the track momentum and p_{jet} is the jet momentum. The p_T of prompt electrons was thus determined with the electron candidate included in the jet. This underlines the importance of only including unassociated ECAL clusters in the jetfinding. Including ECAL clusters associated to tracks would have resulted in a large bias towards the electron direction.

Chapter 5

Prompt Electron Selection

5.1 Track Selection

Electron candidates were required to be associated to the "good" tracks used in jetfinding where tracks were considered "good" in this context if:

- the track had at least 20 space points measured in CJ ($nhitcj > 20$)
- the track had a distance of closest approach to the event vertex in the x y plane of less than 5 cm
- the track had a distance of closest approach to the event vertex in z of less than 200 cm
- the track momentum in the bending plane measured more than 150 MeV/c
- the measured track momentum was less than 65 GeV/c.

These "good" tracks were constrained to originate from the event vertex in z to provide a more reliable polar angle measurement.

Electron candidates were also required to have either a CJ endpoint measurement ($0.815 < |\cos\theta| < 0.91$) or at least 3 CZ samples used in the track fit. These requirements greatly reduced the systematics present in the determination of polar angle of the tracks.

5.2 Electron Identification

Identifying electrons in the mi... of a multihadronic event requires an optimised set of selection criteria. Two properties of electrons make it possible for a pure sample of high momentum electrons to be obtained in hadronic events. The first is the constant dE/dx of electrons in the CJ gas for momenta greater than 2 GeV/c.

The second property of electrons utilised is the distinctive energy loss distribution of electrons in the lead glass calorimeter. A selection for prompt electrons with momentum greater than 2 GeV/c, has already been developed in OPAL for the region $|\cos\theta| < 0.7$ (barrel selection) [22]. Here a set of selection criteria for prompt electrons in the region $0.815 < |\cos\theta| < 0.91$ (endcap selection) is presented. The barrel selection, which will be used with the endcap selection in the measurement of the forward-backward asymmetry for b quarks, is summarised in section 5.4.

5.3 Endcap Electron Identification

5.3.1 dE/dx

As a charged particle traverses any material it loses energy to ionisation of the surrounding material according to the Bethe-Bloch formula

$$-\frac{dE}{dx} = 2\pi N_a r_e^2 m_e c^2 \rho \frac{Z}{A}\frac{z^2}{\beta^2} \times \left[\ln\left(\frac{2m_e\gamma^2 c^2\beta^2 W_{\max}}{I^2}\right) - 2\beta^2 - \delta - 2\frac{C}{Z}\right], \tag{5.1}$$

with

- r_e : classical electron radius = 2.817×10^{-13} cm
- m_e : electron mass
- N_a : Avagadro's number
- I : mean ionisation potential of the medium
- Z : Atomic number of the medium
- A : Atomic weight of the medium
- ρ : density of the medium
- z : charge of the incident particle (units of e)
- $W_{\max}$: The maximum possible kinetic energy transfer
- β : v/c magnitude of the particle velocity in units of the speed of light
- γ : $\frac{1}{\sqrt{1-\beta^2}}$
- C : "shell correction "

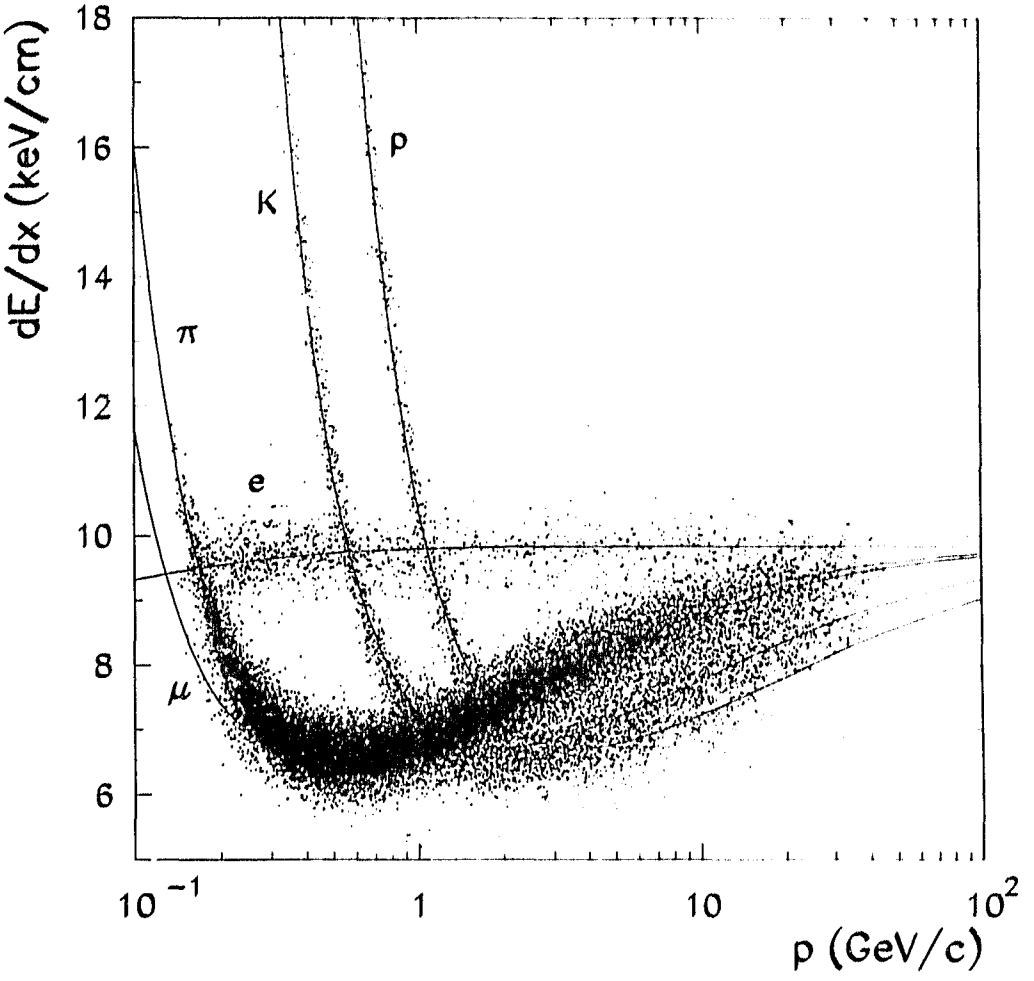

Figure 5.1: *The measured dE/dx in multihadronic events in OPAL (from [45]). The expected bands corresponding to various particles are shown. Note that for momenta greater than 2 GeV/c all particles have a mean dE/dx below that of electrons.*

- δ : "density correction ".

It is important to note that the energy loss to ionisation for a given medium is only a function of the charge and magnitude of the velocity of the incident particle. Figure 5.1 shows the measured dE/dx in the OPAL jet chamber for many tracks in multihadronic events. The bands corresponding to different mass particles are evident.

The value of dE/dx in a medium exhibits a plateau at large particle velocities. This Fermi plateau [46, 47] is due to dielectric effects and therefore depends on the density of the medium. Electrons with $p > 2$ GeV/c are highly relativistic and thus are already at the Fermi plateau. Figure 5.2 shows the measured dE/dx for single electron events with $p > 2$ GeV/c in the range $0.815 < |\cos\theta| < 0.91$. The mean d$E$/d$x$ for these electrons is 10.1 keV/cm.

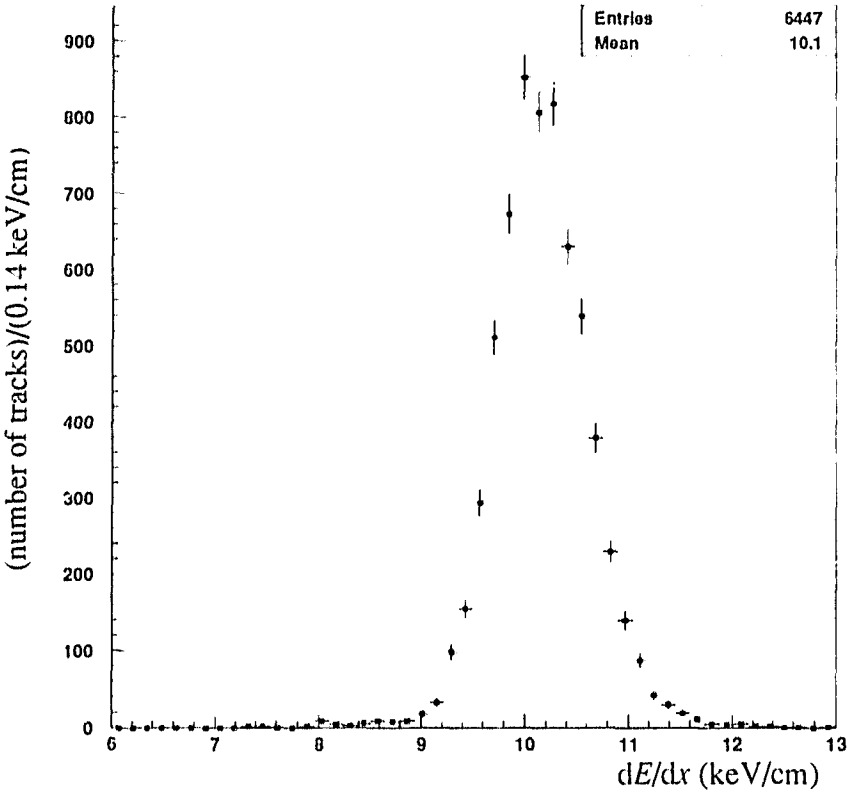

Figure 5.2: *The measured dE/dx distribution for single electrons in the region* $0.815 < |\cos\theta| < 0.91$. *The mean dE/dx is 10.1 keV/cm.*

Fluctuations, due to experimental resolution, may cause particles other than electrons to be measured with the electron dE/dx value; conversely electrons may be measured to have a low dE/dx value. Also, at higher momenta, other particles approach the plateau dE/dx value. It is thus important to have a measure of how consistent a dE/dx measurement is with that of an electron. For this measure it is necessary to know the experimental resolution of the dE/dx measurement.

The resolution for dE/dx measurements depends on many parameters, such as the gas pressure, the sample length, the number of samples and the electronic noise [48, 49]. The OPAL jet chamber has 159 signal wires and thus it is convenient to parameterise the dE/dx resolution as

$$\frac{\sigma_{\mathrm{dE/dx}}}{\mathrm{dE/dx}} = \sigma_{159}\left(\frac{159}{N_{\mathrm{samp}}}\right)^{0.43} \tag{5.2}$$

with σ_{159} the resolution obtained when 159 dE/dx samples (N_{samp}) are used in the dE/dx determination. The 0.43 power is due to the work of Walenta [50]. For single electrons in the range $0.815 < |\cos\theta| < 0.91$, σ_{159} is found to be 2.7% (Figure 5.3). It should be noted that in the angular range $0.815 < |\cos\theta| < 0.91$ 159 samples cannot be obtained. The resolution is stated in this manner so all regions of the detector can be described by the same expression, with only σ_{159} changing.

The number of standard deviations a measurement lies away from the expected electron dE/dx is used as the discriminating variable.

$$N\sigma_{\mathrm{dE/dx}} = \frac{(\mathrm{dE/dx})_{\mathrm{measured}} - (\mathrm{dE/dx})_{\mathrm{expected}}}{\sigma_{\mathrm{dE/dx}}}, \tag{5.3}$$

with

$$\sigma_{\mathrm{dE/dx}} = (\mathrm{dE/dx})_{\mathrm{measured}} \times 2.7\% \left(\frac{159}{N_{\mathrm{samp}}}\right)^{0.43}.$$

The expected dE/dx for electrons was taken to be the 10.1 keV/cm measured from single electron events.

Figure 5.1 shows that, for momenta greater than 2 GeV/c, all particles have a mean dE/dx value less than or equal to that of electrons. Thus electrons candidates were required to satisfy:

$$N\sigma_{\mathrm{dE/dx}} > -2.0. \tag{5.4}$$

Figure 5.3 shows that, for single electrons, the $N\sigma_{\mathrm{dE/dx}}$ distribution is a gaussian with mean of approximately zero and unit width, suggesting an efficiency of approximately 97.7%. The actual efficiency of this requirement will be discussed in section 6.1.

A requirement on the number of dE/dx samples was imposed in order to avoid tracks that had a poorly measured dE/dx value due to a small number of samples

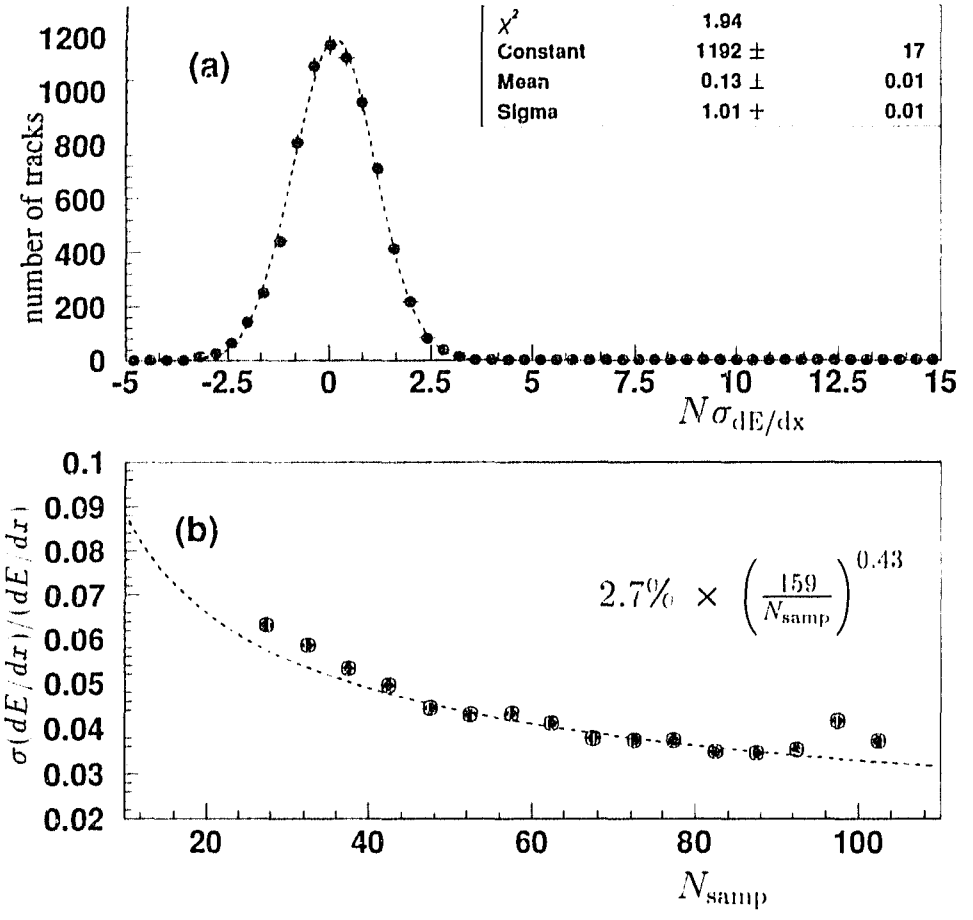

Figure 5.3: *(a) $N\sigma_{\mathrm{dE/dx}}$ (see Equation 5.3) for endcap single electrons. (b) Resolution $\sigma(dE/dx)/(dE/dx)$ vs number of samples for single electrons. The function $2.7\% \times (159/N_{\mathrm{samp}})^{0.43}$ is drawn dashed (from [36]).*

used in the dE/dx determination. Electron candidates were required to satisfy:

$$N_{\rm samp} > 20. \tag{5.5}$$

Besides the above requirement, the number of dE/dx samples was also required to satisfy :

$$\frac{N_{\rm samp}}{\text{Number of space points used in the CJ track } r-\phi \text{ fit}} > 0.5. \tag{5.6}$$

Only space points that are used to determine the track in $r-\phi$ in CJ may be used for the dE/dx determination. dE/dx samples may be discarded due to nearby tracks or because the candidate track passes too closed to a signal wire. A requirement on the fraction of CJ $r-\phi$ samples used imposes a form of isolation criterion and serves to make the efficiency for the $N_{\rm samp}$ requirement less dependent on $|\cos\theta|$.

5.3.2 Calorimetric Criteria

Electrons that enter the lead glass calorimeter lose energy through repeated processes of bremsstrahlung and pair production from the resulting photons (electromagnetic shower). This electromagnetic process creates a localised energy deposit with a distinctive longitudinal and transverse distribution.

The EE represents approximately $22X_0$ of absorber and therefore, for a very large fraction of electrons with $E < 50$ GeV/c, all of the energy will be deposited in the electromagnetic calorimeter. Muons do not initiate electromagnetic showers due to the lower bremsstrahlung cross section and therefore leave very little energy deposit in the calorimeter (≈ 300 MeV). Hadrons interact in the calorimeter mainly through nuclear interactions. These interactions tend to produce many low energy particles that escape detection by the lead glass. Hadronic showers also tend to have much larger longitudinal and transverse dimensions than electromagnetic showers [51]. The scale of hadronic showers is the nuclear interaction length and EE is approximately 2 interaction lengths thick.

The above factors make it possible to identify electrons with the electromagnetic calorimeter through the distinctive shower shape and the ratio of the energy measured in the calorimeter to the momentum measured in the central detector. Figure 5.4 shows the ratio of measured cluster energies to central track momenta ($E_{\rm clus}/p$) distributions for electrons from single electron events, pions (selected opposite signed pairs of tracks that have a mass consistent with that of a K^0 [52]) and muons from $e^+e^- \rightarrow Z^0 \rightarrow \mu^+\mu^-$ events. Three calorimetric variables were considered in selecting prompt electrons: E/p , θ-match and $N_{\rm blks}$.

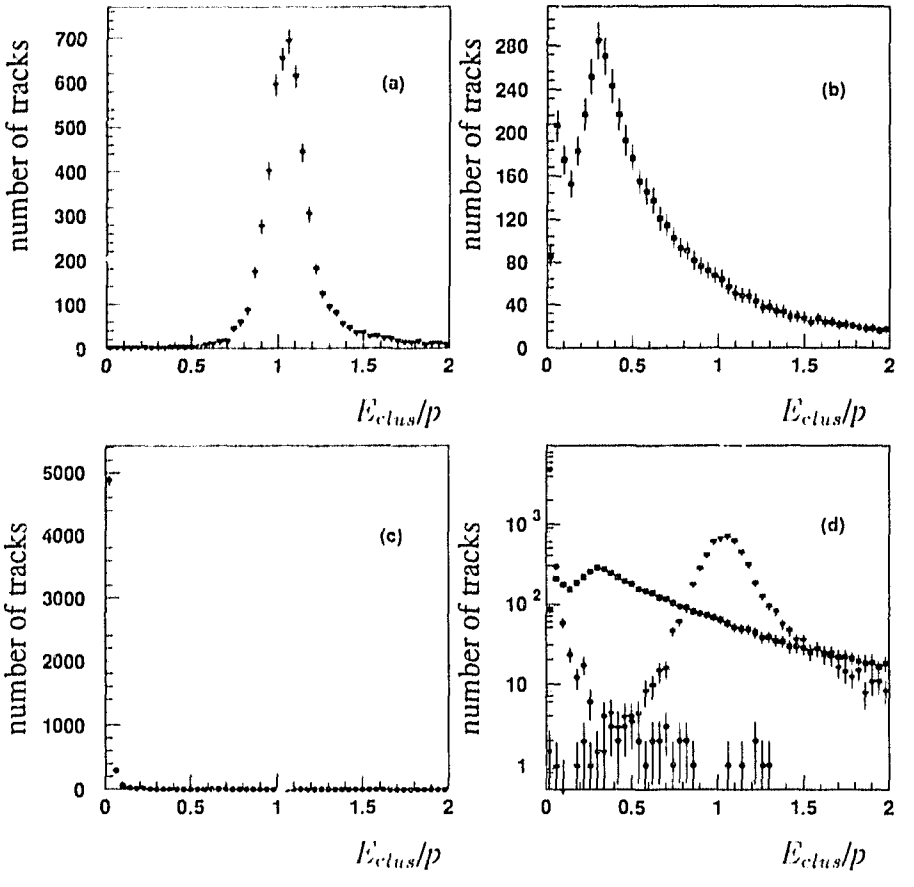

Figure 5.4: *The measured $E_{\rm clus}/p$ distributions for (a) single electrons, (b) pions and (c) muons from $e^+e^- \rightarrow \mu^+\mu^-$ events, in the region $0.815 < |\cos\theta| < 0.91$. (d) shows the three distributions overlaid on a logarithmic scale. The very small E/p (~ 0.006) for muons is evident in (d).*

5.3.2.1 E/p

In a multihadronic event, electromagnetic clusters are rarely created in isolation. Accompanying particles may increase the measured cluster energy. Conversely, an energy deposit may be split into more than one cluster due to neighbouring energy deposits. A corrected energy was calculated, which exploits the expected shape of electromagnetic showers, to reduce these effects on the energy measurement.

The corrected energy associated to a track was calculated by first finding the block in EE within which the track traversed its first four radiation lengths ($\sim$ 10 cm). This avoided problems arising from tracks extrapolated to the edge of a block. This block is termed the "centre block", and two rings of blocks were formed around the centre block. One contained the eight "touching" blocks and one the sixteen "next-to-touching" blocks (Figure 5.5).

As an attempt to remove any overlapping energy in the inner ring of blocks, a subtraction was performed as follows. The average of the eleven blocks in the outer ring, that were not in the direction of the extrapolated track (in the x-y plane), was calculated. Not all sixteen "next-to-touching" blocks were used in calculating this average to reduce the effects of track mis-extrapolations. Although no electron energy was expected in any of the "next-to-touching" blocks, the five blocks in the direction of the track were the most likely to be affected by any track misextrapolations. Since there is a small amount of noise in the EE electronics, a block had to have registered an energy deposit of more than 20 MeV to be considered in the average. This average energy was then subtracted from the centre and eight touching blocks. If this subtraction made the energy in a block negative, the block energy was set to zero. The resulting energy in these nine inner blocks was then summed and scaled by the ratio of the cluster energy to the raw cluster energy. This scaling took into account the average energy lost by an electron before entering the EE. It is this corrected energy that was associated to the track to form the ratio E/p . Hereafter, E will denote this corrected energy.

The subtraction of the outer ring energy accomplished two things. First, since there is no electron energy expected in this ring, it was an attempt to remove any overlapping activity affecting the energy measurement. Secondly, and perhaps more importantly, this subtraction tended to reduce the energy measured for pions. This reduction of the measured pion energy had the effect of reducing the background to the electron signal in the region of interest. Figure 5.6 compares the corrected energy to momentum ratio with the cluster energy and p for pions identified as originating from K^0 decays.

Electron candidates were required to satisfy:

$$0.8 < E/p < 1.2. \tag{5.7}$$

Figure 5.7 shows the measured E/p vs. $|\cos\theta|$ for single electron events in four bins of momentum. The angular range $0.815 < |\cos\theta| < 0.91$ was chosen for the

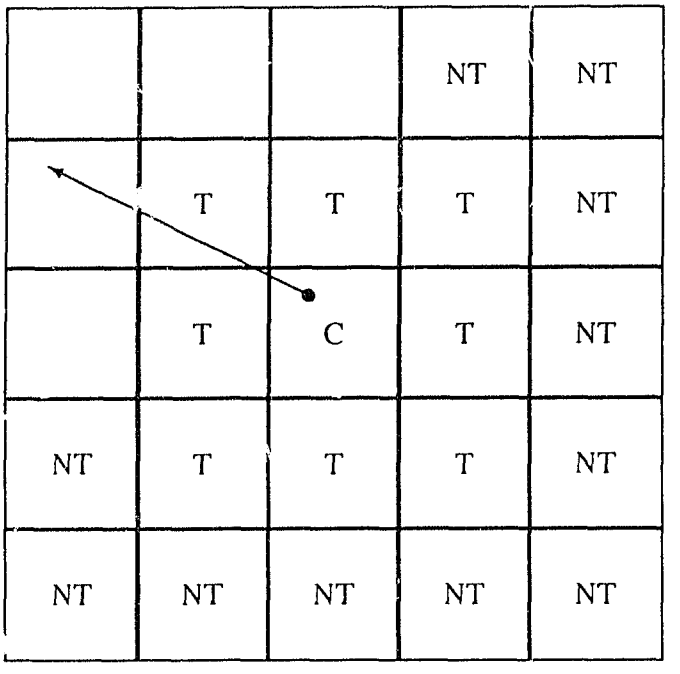

Figure 5.5: *The geometry used for the corrected energy. The track impact point is denoted by •, with a momentum vector in the x-y plane as shown. C denotes the centre block. Blocks denoted T are the "touching" blocks and NT denotes the "next-to-touching" blocks used in the background calculation.*

selection since empirically it was found to be free of large systematic effects in the E/p resolution.

5.3.2.2 θ-Match

The blocks of the EE are aligned parallel to the z axis. Electrons from the centre of the detector that enter the EE, on average, have three blocks in their direct path in $r - z$. This non-projecting geometry can be used to provide a crude longitudinal shower sampling. Figure 5.8 shows that longitudinal shower sampling is a potential selector of electrons over pions.

Any energy deposit in the EE will have a reconstructed centre of gravity in θ moved away from the track impact point, due to the non-projecting geometry (Figure 5.9). This deviation is corrected on a cluster by cluster basis assuming that the deposition is due to an electron. [1]. This correction yields a difference $|\theta_{\rm track} - \theta_{\rm cluster}|$ very close to zero for electrons, while hadrons have a much broader

[1] At $|\cos\theta| = 0.85$ the magnitude of this correction is approximately 20 mrad.

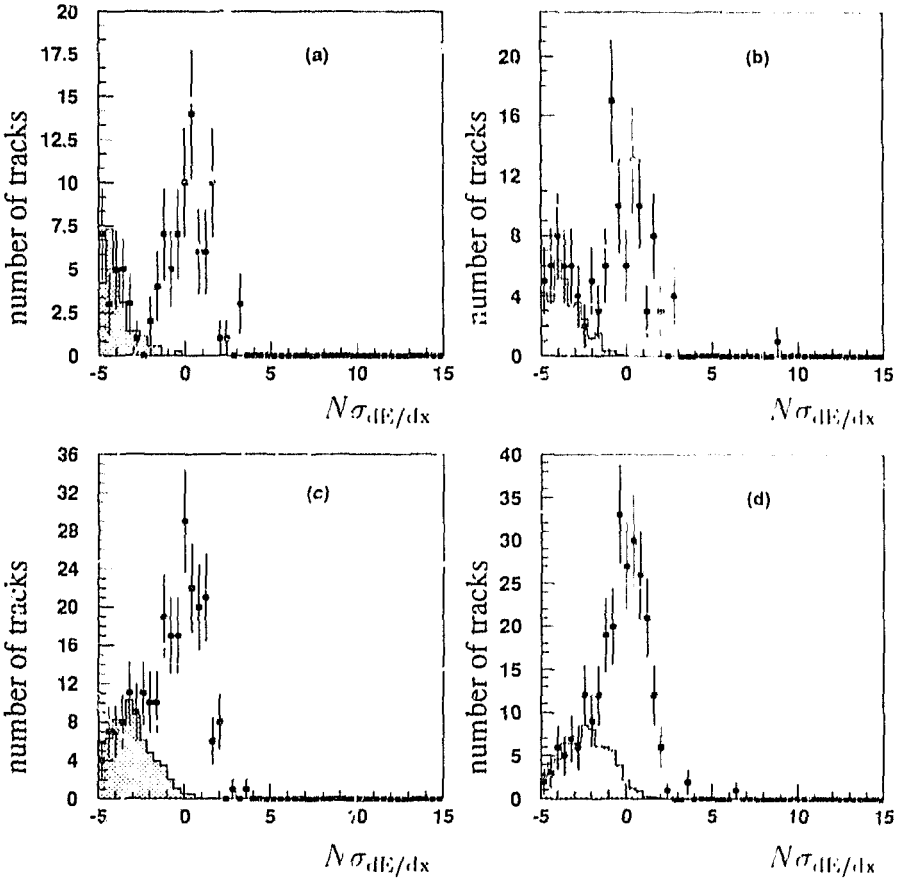

Figure 6.7: *The $N\sigma_{dE/dx}$ distributions for all prompt electron candidates with $p_T > 1.0$ GeV/c in the endcap acceptance with all the electron selection criteria applied except the $N\sigma_{dE/dx}$ and 0-match requirements. (a) is the distribution for the momentum bin of 2–4 GeV/c, while (b), (c) and (d) correspond to the momentum bins of 4–6 GeV/c, 6–10 GeV/c and above 10 GeV/c respectively. The shaded histograms are the predicted background shapes obtained with the requirement $0.1 < E/p < 0.6$, the normalisation was determined by the fit. The signal region is $N\sigma_{dE/dx} > -2.0$.*

p (GeV/c)	1	2	3	4
2–4	$(88.2 \pm 3.8)\%$	$(88.2 \pm 3.8)\%$	$(88.5 \pm 4.0)\%$	$(87.7 \pm 3.9)\%$
4–6	$(80.8 \pm 4.5)\%$	$(80.7 \pm 4.4)\%$	$(80.0 \pm 4.7)\%$	$(79.1 \pm 4.6)\%$
6–10	$(86.4 \pm 3.0)\%$	$(86.1 \pm 3.0)\%$	$(87.4 \pm 3.3)\%$	$(85.7 \pm 3.2)\%$
above 10	$(91.7 \pm 2.8)\%$	$(90.7 \pm 2.7)\%$	$(96.2 \pm 4.7)\%$	$(90.7 \pm 3.9)\%$

Table 6.8: *The efficiency for a prompt electron with $p_T > 1.0$ GeV/c to satisfy the requirement $|\theta_{\rm track} - \theta_{\rm cluster}| < 8$ mrad. The results of many fits are shown to illustrate the agreement among the various fitting methods. Column 1 is the efficiency calculated with background shape determined by the selection $N\sigma_{\rm dE/dx} < -2.5$, but with the q in Equation 6.1 fixed at 2. Column 2 was calculated with q in Equation 6.1 fixed at 2 and the background shape determined by the selection $N\sigma_{\rm dE/dx} < -3.5$. Column 3 is the efficiency obtained from fitting the $N\sigma_{\rm dE/dx}$ distribution with a background shape determined by the selection $0.1 < E/p < 0.6$. Finally column 4 is again a fit to the $N\sigma_{\rm dE/dx}$, but with the background shape determined by the selection $0.1 < E/p < 0.4$. These values should be compared to column 1 of Table 6.7.*

6.1.4 $N_{\rm blks}$ Efficiency

The efficiency for a prompt electron to satisfy the requirement on the number of blocks in the reconstructed cluster,

$$N_{\rm blks} < 16,$$

was determined similarly to the efficiency for the θ-match requirement. The E/p and $N\sigma_{\rm dE/dx}$ distributions were fit as in section 6.1.3. The $N_{\rm blks}$ efficiency was determined with all of the other electron selection requirements applied. Figures 6.8 and 6.9 show the E/p distributions, without the $N_{\rm blks}$ requirement applied and the resulting background normalisations for transverse momentum cuts of $p_T > 1.0$ GeV/c and $p_T > 0.8$ GeV/c respectively. Table 6.9 shows the efficiencies for the $N_{\rm blks}$ requirement determined as the ratio of the number of prompt electrons above the predicted background with and without the $N_{\rm blks}$ requirement applied. As expected from the single electrons, (Figures 5.11 and 5.12), the efficiency for low energy electrons is very high, while there is some loss of efficiency at higher momenta.

As for the θ-match efficiency, Table 6.10 compares the $N_{\rm blks}$ efficiency obtained using various $N\sigma_{\rm dE/dx}$ requirements to determine the background shape and the efficiency obtained from fitting the $N\sigma_{\rm dE/dx}$ distribution. These various determinations of the efficiency are in good agreement.

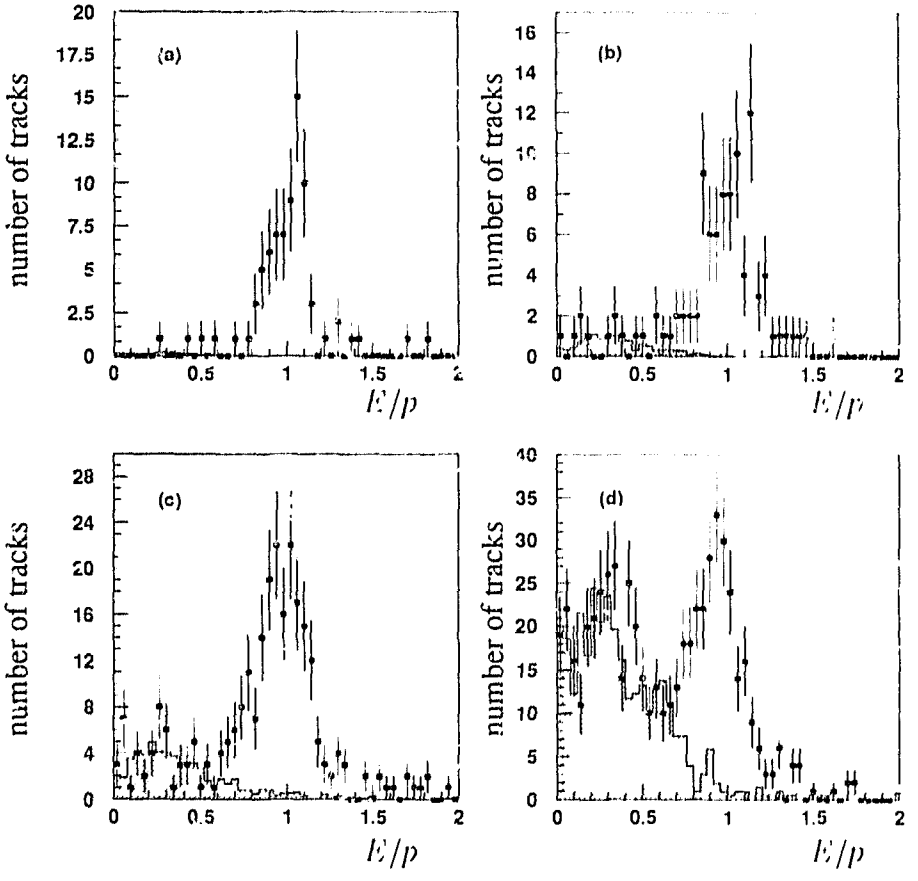

Figure 6.8: *The E/p distributions for all candidates with $p_T > 1.0$ GeV/c in the endcap acceptance with all the electron selection criteria applied except the E/p and $N_{\rm blks}$ requirements. (a) is the distribution for the momentum bin of 2–4 GeV/c, while (b), (c) and (d) correspond to the momentum bins of 4–6 GeV/c, 6–10 GeV/c and above 10 GeV/c respectively. The shaded areas are the predicted background shapes obtained with the selection $N\sigma_{{\rm d}E/{\rm d}x} < -2.5$, the normalisations were determined by the fit. The signal region is $0.8 < E/p < 1.2$.*

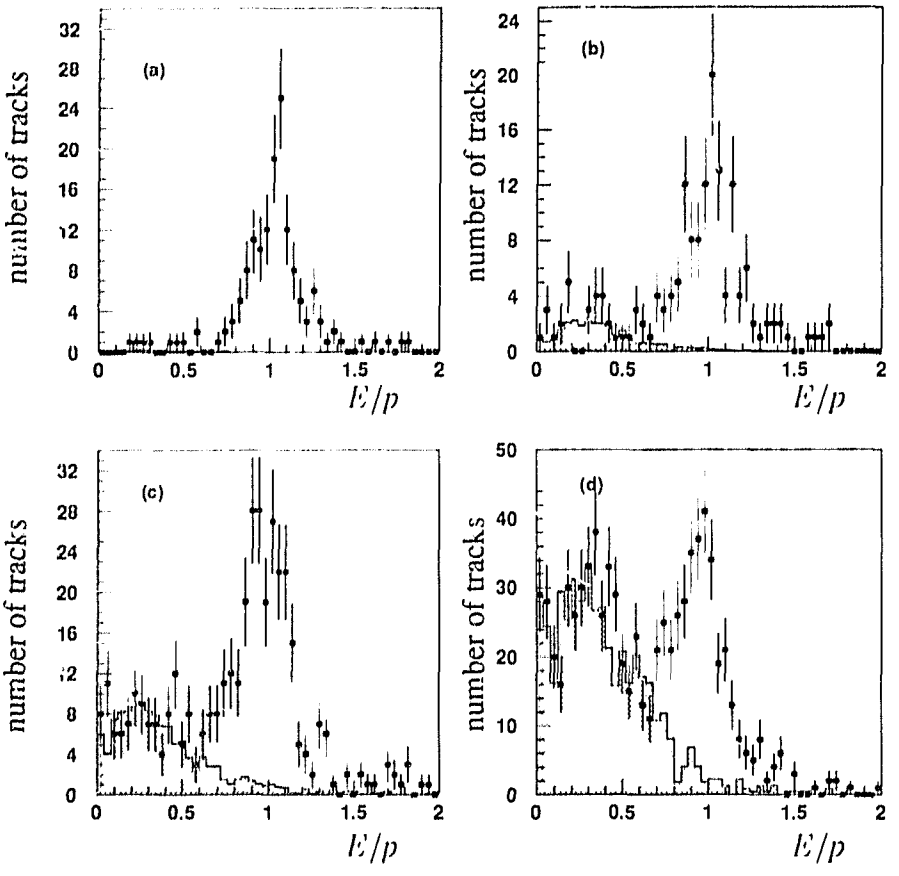

Figure 6.9: *The E/p distributions for all candidates with $p_T > 0.8$ GeV/c in the endcap acceptance with all the electron selection criteria applied except the E/p and $N_{\rm blks}$ requirements. (a) is the distribution for the momentum bin of 2–4 GeV/c, while (b), (c) and (d) correspond to the momentum bins of 4–6 GeV/c, 6–10 GeV/c and above 10 GeV/c respectively. The shaded areas are the predicted background shapes obtained with the selection $N\sigma_{\rm dE/dx} < -2.5$, the normalisations were determined from the fit. The signal region is $0.8 < E/p < 1.2$.*

p (GeV/c)	$p_T > 1.0$ GeV/c	$p_T > 0.8$ GeV/c
2–4	$(100 \pm 1.9)\%$	$(100 \pm 1.1)\%$
4–6	$(100 \pm 1.8)\%$	$(100 \pm 1.1)\%$
6–10	$(98.5 \pm 1.3)\%$	$(96.7 \pm 1.7)\%$
above 10	$(93.7 \pm 2.5)\%$	$(93.9 \pm 3.0)\%$

Table 6.9: *The efficiency for a prompt electron in the region* $0.815 < |\cos\theta| < 0.91$ *to satisfy the requirement* $N_{\rm blks} < 16$ *after all other electron selection criteria have been applied. This efficiency is determined from the* E/p *distribution as described in the text.*

It might be possible that the $N_{\rm blks}$ and θ-match requirements are correlated. For example, clusters with many blocks may be systematically displaced from candidate tracks in θ. The combined efficiency of the two requirements was obtained using the same method as for the two individual efficiencies to test for such correlations. Table 6.11 compares the efficiency determined for the combined $N_{\rm blks}$ and θ-match requirements, to the product of the individual efficiencies. No significant systematic trend is suggested. The efficiencies for the combined $N_{\rm blks}$ and θ-match requirements obtained in this manner are not used, as the number of hadrons misidentified as electrons is very large when both of these requirements are removed. It is possible that such a large amount of hadronic background could affect the efficiency determination.

6.1.5 E/p Efficiency

The efficiency for a prompt electron to satisfy the requirement

$$0.8 < E/p < 1.2$$

was determined using a combination of the single electron and inclusive muon data. It was not possible to determine the efficiency of the E/p requirement from the single electrons, as these electrons are isolated and thus any effect due to the multihadronic environment could not be assessed. Prompt muons originate from the same sources as prompt electrons and therefore should have the same surrounding activity, however muons interact very differently to electrons in the electromagnetic calorimeter. A combination of the single electrons and inclusive muons provided a sample that had the same surrounding activity and the same electromagnetic shower properties as prompt electrons. The surrounding activity can cause E/p to be mismeasured due to additional energy deposited near the electron in the calorimeter.

p (GeV/c)	1	2	3	4
2–4	$(100 \pm 1.9)\%$	$(100 \pm 2.0)\%$	$(100 \pm 1.9)\%$	$(100 \pm 1.8)\%$
4–6	$(100 \pm 1.8)\%$	$(100 \pm 1.8)\%$	$(100 \pm 1.9)\%$	$(100 \pm 1.9)\%$
6–10	$(98.5 \pm 1.3)\%$	$(98.6 \pm 1.4)\%$	$(98.6 \pm 1.9)\%$	$(98.9 \pm 1.9)\%$
above 10	$(94.3 \pm 2.5)\%$	$(93.9 \pm 2.4)\%$	$(93.0 \pm 3.6)\%$	$(94.3 \pm 3.9)\%$

Table 6.10: *The efficiency for a prompt electron with $p_T > 1.0$ GeV/c to satisfy the $N_{\rm blks} < 16$ requirement. The results of many fits are shown to illustrate the agreement among the various fitting methods. Column 1 is the efficiency calculated with a background shape determined by the requirement $N\sigma_{\rm dE/dx} < -2.5$, but with q in Equation 6.1 fixed at 2. Column 2 was calculated with the q fixed at 2 and a background shape determined with the selection $N\sigma_{\rm dE/dx} < -3.5$. Column 3 is the efficiency obtained from fitting the $N\sigma_{\rm dE/dx}$ distribution with a background shape obtained with the selection $0.1 < E/p < 0.6$. Finally column 4 is again a fit to the $N\sigma_{\rm dE/dx}$, but with the background shape determined by $0.1 < E/p < 0.4$. Good agreement is seen between the efficiency calculated in column 1 of Table 6.9.*

The E/p efficiency was determined by combining the EE block energies from inclusive muon and single electron events to determine an E/p value for a "pseudo-candidate". The muon and electron were required to be in the same momentum bin and at the same end of the detector in z. In forming E/p , the momentum of the single electron was used, while the p_T of the muon was used in forming the pseudo-candidate. The energy of the pseudo-candidate was formed by adding the block energies associated with the inclusive muon to those of the single electron. In determining the energy to be used in E/p the energy deposited in the inner ring of nine blocks used to form E (Section 5.3.2.1, Figure 5.5), by the muon, was subtracted.

p (GeV/c)	product	combined fit
2–4	$(88.7 \pm 3.1)\%$	$(88.8 \pm 2.9)\%$
4–6	$(84.9 \pm 3.9)\%$	$(80.7 \pm 3.9)\%$
6–10	$(81.4 \pm 3.1)\%$	$(74.3 \pm 3.2)\%$
above 10	$(86.7 \pm 4.1)\%$	$(81.1 \pm 4.2)\%$

Table 6.11: *A comparison of the product of the $N_{\rm blks}$ and 0-match efficiencies and a determination of the combined efficiency for $p_T > 0.8$ GeV/c. No significant correlation is suggested.*

The expected muon energy deposit in the inner ring of nine blocks was determined using $\mu^+\mu^-$ events. The events were selected as in [16] with further requirements imposed on the tracks. To be accepted a muon track had to have a momentum less than 30 GeV/c and the two tracks in the event were required to be more than 2° from collinear. The requirement on the acollinearity ensured that the radiated photon in the event was well removed from the muon track. Figure 6.10 shows the raw energy deposited in the nine inner blocks for muons selected in this manner. The mean energy deposit is approximately 300 MeV, therefore in the single electron–muon sum, 300 MeV was subtracted to account for the muon energy.

Table 6.12 shows the efficiency obtained from this method for a prompt electron to satisfy the E/p requirement for $p_T > 1.0$ GeV/c and $p_T > 0.8$ GeV/c. The efficiency in the 2–4 GeV/c momentum bin was determined by averaging the efficiencies of the three other momentum bins. The efficiency for the lowest momentum bin was evaluated in this manner since, in this momentum region, the inclusive muon sample and single electron samples have larger contamination than for larger momenta. The average appears justified as the efficiency of the E/p requirement appears constant over the three higher momentum bins. Figure 6.11 shows the E/p distributions for the pseudo-candidates for the case of $p_T > 0.8$ GeV/c. Good general agreement with the shape of the E/p distribution in Figure 6.3 is seen.

p (GeV/c)	$p_T > 1.0$ GeV/c	$p_T > 0.8$ GeV/c
2–4	(77.4 ± 4.2)%	(75.7 ± 3.6)%
4–6	(79.7 ± 4.7)%	(77.3 ± 3.6)%
6–10	(78.2 ± 3.9)%	(74.8 ± 3.4)%
above 10	(74.2 ± 4.0)%	(75.0 ± 3.7)%

Table 6.12: *The efficiency for a prompt electron in the region* $0.815 < |\cos\theta| < 0.91$ *to satisfy the requirement* $0.8 < E/p < 1.2$, *determined as described in the text.*

As a check on the consistency of the efficiency evaluated in this manner, Table 6.13 shows the efficiency determined using inclusive muon samples selected with more stringent requirements on $\chi^2_{\mu\mu}$. There is no suggestion of a significant variation of the efficiency.

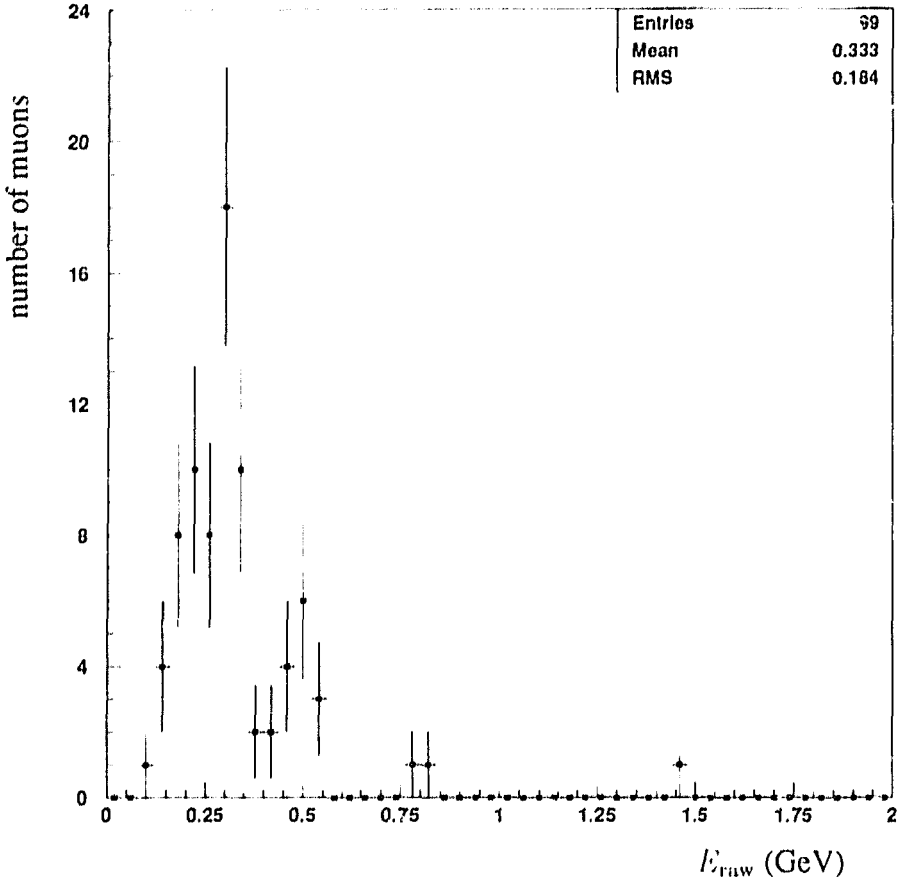

Figure 6.10: *The raw energy deposit, in the inner nine blocks used for the E/p determination, for isolated muons in the range $0.815 < |\cos\theta| < 0.91$ selected as described in the text. The average raw energy deposit is approximately 300 MeV.*

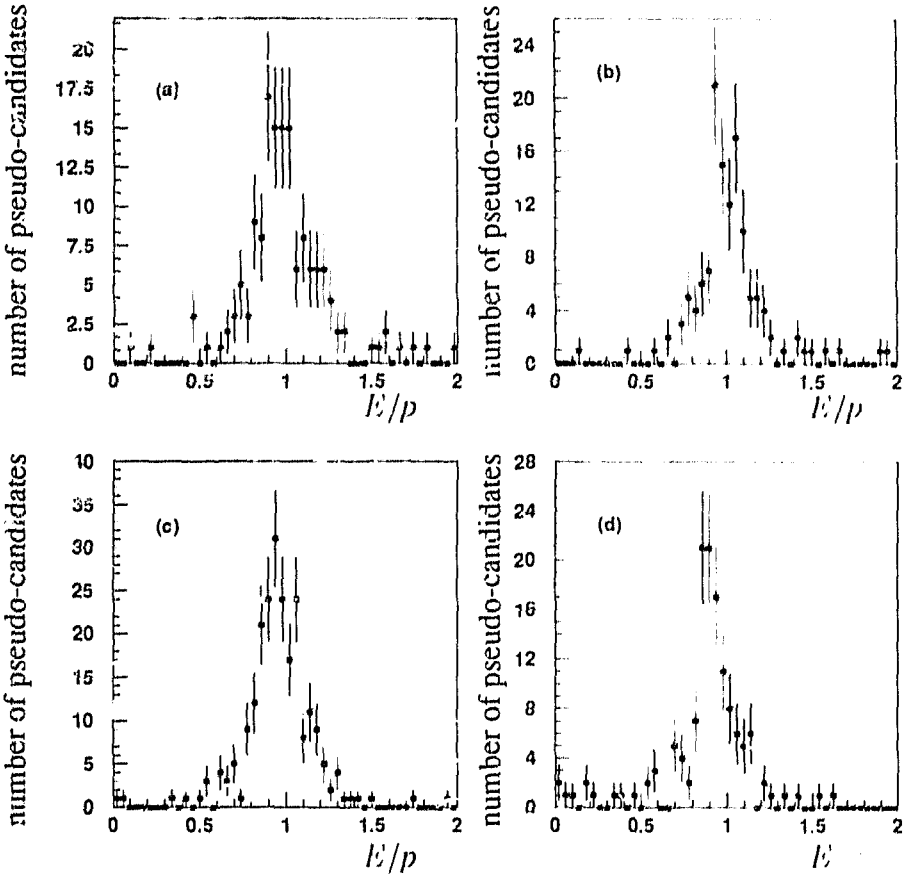

Figure 6.11: *The E/p distributions for pseudo-candidates obtained from combining the single electron and muon data for the case of $p_T > 0.8$ GeV/c. (a) is for the momentum bin 2–4 GeV/c and is not used to calculate the efficiency. (b) is for the momentum bin 4–6 GeV/c. (c) is for the momentum bin 6–10 GeV/c and (d) is for momenta greater than 10 GeV/c.*

p (GeV/c)	$\chi_{pos}^2 < 2.0$	$\chi_{pos}^2 < 1.5$
4-6	(79.5 ± 4.7)%	(80.9 ± 5.7)%
6-10	(83.3 ± 3.9)%	(79.7 ± 5.0)%
above 10	(72.0 ± 4.7)%	(75.9 ± 5.3)%

Table 6.13: *The efficiency for a pseudo-candidate to satisfy the requirement $0.8 < E/p < 1.2$, for $p_T > 1.0$ GeV/c determined using purer inclusive muon samples. Good agreement is seen with Column 1 of Table 6.12. Note that the efficiency for the 2-4 GeV/c momentum bin is not given in this table as it is not determined directly from the data.*

6.1.6 $N\sigma_{dE/dx}$ Efficiency

The single electron sample was used to establish the efficiency of the $N\sigma_{dE/dx}$ requirement. The fraction of all single electrons that satisfied the requirement

$$N\sigma_{dE/dx} > -2.0$$

was determined. The efficiency determined in this way was (97.67 ± 0.16)%, taken to be valid for all transverse momenta.

The prompt electron data themselves were used as a check on this efficiency determination. Using the fit to the background fraction, the amount of signal above the predicted background was determined for the range $-5.0 < N\sigma_{dE/dx} < 5.0$. The fraction of this signal that fell above $N\sigma_{dE/dx} > -2.0$ was calculated for the four momentum ranges. Table 6.14 shows the efficiency determined with this method for $p_T > 1.0$ GeV/c. The efficiency determined in this way is systematically lower than the (97.7 ± 0.2)% determined from the single electrons. The efficiency determined this way could suffer from systematic problems. It relies on the signal actually being described by a gaussian and that the N_{hits}, θ-match and E/p efficiencies are independent of the $N\sigma_{dE/dx}$ efficiency. Since it is not clear if this is a real loss in efficiency, an additional systematic error of 5% was added to the overall error on the efficiency of the $N\sigma_{dE/dx}$ requirement. This error covers the maximum difference between the two determinations indicated in any momentum bin. Therefore the efficiency for a prompt electron to satisfy the $N\sigma_{dE/dx}$ requirement is (97.7 ± 5.2)%.

6.1.7 Total Selection Efficiency

The selection efficiency for prompt electrons in the range $0.815 < |\cos\theta| < 0.91$ is the product of the efficiencies determined above. Table 6.15 presents the efficiency

p GeV/c	$N\sigma_{dE/dx}$ efficiency
2–4	$(96.6 \pm 2.2)\%$
4–6	$(89.2 \pm 3.6)\%$
6–10	$(90.8 \pm 2.1)\%$
above 10	$(91.5 \pm 1.6)\%$

Table 6.14: *The efficiency of the $N\sigma_{dE/dx}$ requirement, for $p_T > 1.0$ GeV/c, as determined from the $N\sigma_{dE/dx}$ distribution as described in the text. This efficiency is systematically lower than the $(97.7 \pm 0.2)\%$ expected from the single electron sample.*

for a prompt electron to satisfy the combined requirements

$$\begin{gathered}
\text{CJ endpoint used in track fit} \\
N_{\text{samp}} > 20 \\
\frac{N_{\text{samp}}}{\text{Number of hits used in the CJ } r-\phi \text{ fit}} > 0.5 \\
|\theta_{\text{track}} - \theta_{\text{cluster}}| < 8 \text{ mrad} \\
N_{\text{blks}} < 16 \\
N\sigma_{dE/dx} > -2.0 \\
0.8 < E/p < 1.2
\end{gathered}$$

The efficiency for a prompt electron to satisfy the track quality, kinematic and geometry requirements will be discussed in Section 6.3.

p GeV/c	$p_T > 0.8$ GeV/c	$p_T > 1.0$ GeV/c
2–4	$(50.8 \pm 4.4)\%$	$(52.9 \pm 5.3)\%$
4–6	$(47.2 \pm 4.1)\%$	$(47.4 \pm 5.2)\%$
6–10	$(40.7 \pm 3.5)\%$	$(45.2 \pm 4.0)\%$
above 10	$(44.4 \pm 4.0)\%$	$(44.1 \pm 4.0)\%$

Table 6.15: *The efficiency for a prompt electron to satisfy the selection criteria in the angular range $0.815 < |\cos\theta| < 0.91$ for two transverse momentum regions.*

6.2 Misidentification Fraction Determination

The E/p fit, with all the electron selection requirements applied, used to establish the efficiencies, also determined the number of hadronic tracks expected in the sample for each momentum bin. Table 6.16 shows the number of prompt electron candidates expected to be hadrons misidentified as electrons for the angular region $0.815 < |\cos\theta| < 0.91$ and Table 6.17 shows the number of prompt electron candidates found in each momentum bin. Thus, for the endcap selection, with $p_T > 0.8$ GeV/c, $(2.6 \pm 0.3)\%$ of the sample is expected to be hadrons misidentified as electrons, while for $p_T > 1.0$ $(2.4 \pm 0.3)\%$ hadron contamination is expected.

p GeV/c	$p_T > 0.8$ GeV/c	$p_T > 1.0$ GeV/c
2–4	(0.18 ± 0.27)	(0.14 ± 0.14)
4–6	(1.51 ± 0.47)	(0.58 ± 0.21)
6–10	(6.84 ± 0.15)	(3.60 ± 0.59)
above 10	(7.97 ± 0.66)	(6.53 ± 0.50)

Table 6.16: *The number of the prompt electron candidates expected to be hadrons misidentified as electrons for the endcap selection.*

p GeV/c	$p_T > 0.8$ GeV/c	$p_T > 1.0$ GeV/c
2–4	115	65
4–6	98	68
6–10	187	146
above 10	229	182

Table 6.17: *The number of the prompt electron candidates found for each momentum bin for the endcap selection.*

The same fitting technique was used to establish the misidentification rate for the barrel selection. The $E_{\rm cone}/p$ distribution, with all the other electron selection criteria applied, was fit as for the endcap selection. Figure 6.12 shows the background normalisations obtained for $p_T > 0.8$ GeV/c and Table 6.18 gives the expected misidentification percentages for the barrel selection in the four momentum bins.

Three different fits were used to assess possible systematic effects in the determinations of the misidentification fractions from the E/p and $E_{\rm cone}/p$ fits; the standard E/p fit with g in Equation 6.1 allowed to float free, the E/p fit with

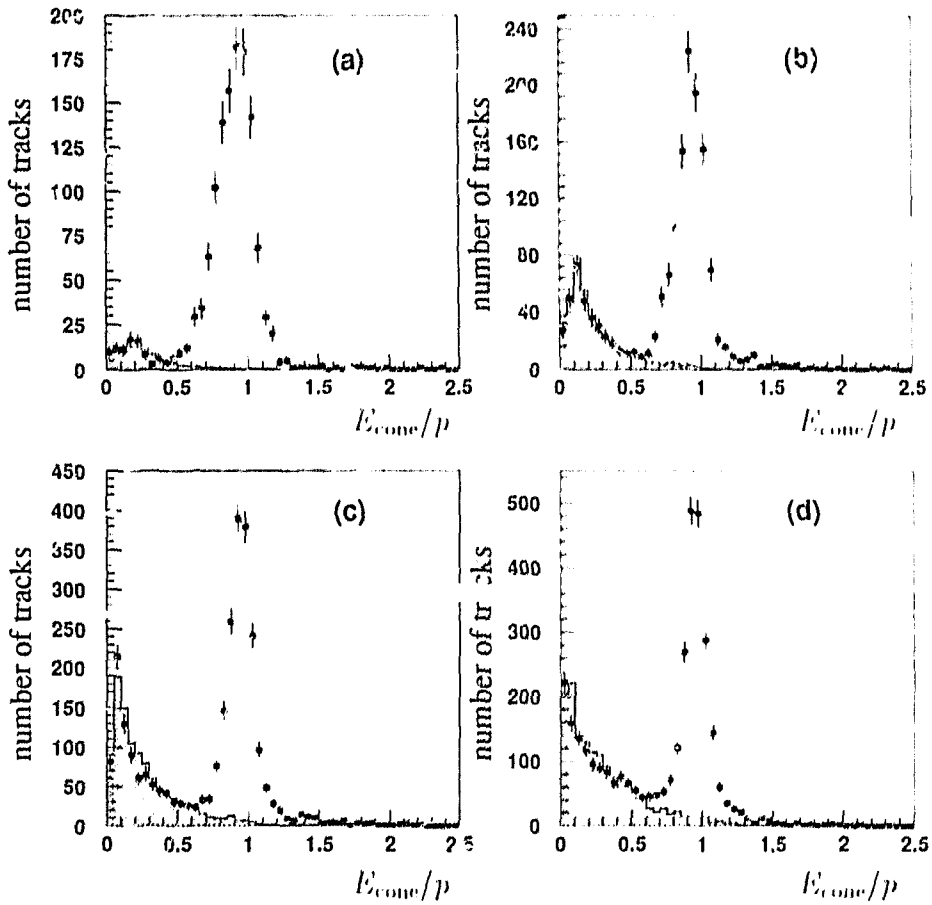

Figure 6.12: *The background normalisations used to establish the fraction of the prompt electron signal that is hadrons misidentified as electrons for the barrel selection, for $p_T > 0.8$ GeV/c. (a) 2–4 GeV/c (b) 4–6 GeV/c (c) 6–10 GeV/c (d) above 10 GeV/c.*

p GeV/c	$p_T > 0.8$ GeV/c	$p_T > 1.0$ GeV/c
2–4	$(0.5 \pm 0.1)\%$	$(0.3 \pm 0.1)\%$
4–6	$(2.1 \pm 0.1)\%$	$(1.2 \pm 0.1)\%$
6–10	$(4.1 \pm 0.1)\%$	$(2.8 \pm 0.1)\%$
above 10	$(7.3 \pm 0.3)\%$	$(6.4 \pm 0.2)\%$

Table 6.18: *The percentage of the prompt electron signal that is expected to be hadrons misidentified as electrons for the barrel selection.*

g fixed at 2 and the $N\sigma_{\mathrm{dE/dx}}$ fit. The $N\sigma_{\mathrm{dE/dx}}$ fit is almost independent of the other two. Table 6.19 shows the total misidentification fractions determined from these three fits for the endcap selection. The three background fractions agree within the fit errors for the endcap selection.

	E/p g free	E/p g fixed at 2	$N\sigma_{\mathrm{dE/dx}}$
Endcap selection	$(2.6 \pm 0.3)\%$	$(3.1 \pm 0.3)\%$	$(4.3 \pm 1.4)\%$
Barrel selection	$(3.8 \pm 0.1)\%$	$(4.2 \pm 0.1)\%$	$(3.6 \pm 0.3)\%$

Table 6.19: *The global hadron misidentification rates for the endcap and barrel electron selections, for $p_T > 0.8$ GeV/c, determined in three different ways. There is evidence for a systematic in the barrel determination.*

Table 6.19 shows the misidentification fractions determined from the three fits for the barrel selection. There is a possibility of a disagreement between the E_{cone}/p determinations using different descriptions of the signal functional form. The misidentification fraction from the $N\sigma_{\mathrm{dE/dx}}$ determination agrees well with the E/p fit with g allowed to be determined by the fit, however when the signal is described as a gaussian a slight disagreement is suggested. The E_{cone}/p signal is not expected to be gaussian, however the errors from all the fits were increased by 50% to account for the possible bias. The result of the E_{cone}/p fit with g allowed to float in the fit, is used to determine the background fraction.

The total fraction of hadrons misidentified as electrons in the sample for $p_T > 0.8$ GeV/c is $(3.8 \pm 0.2)\%$ for the barrel selection and $(2.6 \pm 0.3)\%$ for the endcap selection.

It will be essential to know the variation of the background fraction with $|\cos\theta_{\mathrm{thrust}}|$ for the $A_{\mathrm{FB}}^{\mathrm{b}}$ determination. The E_{cone}/p distribution was fit in three bins of $|\cos\theta_{\mathrm{thrust}}|$ to determine this variation for the barrel selection. Table 6.20 shows the background fraction for the barrel selection in the three bins of $|\cos\theta_{\mathrm{thrust}}|$.

There was only enough data in the last $|\cos\theta_{\rm thrust}|$ bin ($0.7 < |\cos\theta_{\rm thrust}| < 0.9$) to fit the misidentification fraction for the endcap selection reliably. The decreasing misidentification fraction with increasing $|\cos\theta_{\rm thrust}|$ is mainly due to the improving dE/dx separation with $|\cos\theta|$.

$\lvert\cos\theta_{\rm thrust}\rvert$	Barrel selection	Endcap selection
0–0.25	$(4.35 \pm 0.28)\%$	–
0.25–0.7	$(3.63 \pm 0.19)\%$	–
0.7–0.9	$(2.14 \pm 0.32)\%$	$(2.1' \pm 0.55)\%$

Table 6.20: *The variation of the hadronic contamination of the prompt electron signal with* $|\cos\theta_{\rm thrust}|$, *for* $p_T > 0.8$ *GeV/c. The endcap selection provides only enough data in the last* $|\cos\theta_{\rm thrust}|$ *bin to determine reliably the misidentification fraction.*

6.3 Kinematic and Geometric Efficiencies

In calculating absolute or relative prompt electron rates it is necessary to know the efficiency for an electron from a prompt source to satisfy certain kinematic and geometric requirements. These efficiencies were calculated using simulated data (Monte Carlo). The data were simulated using the JETSET 7.3 [32] event generator and a program to simulate the response of the OPAL detector [55]. Specifically, JETSET was used to generate simulated Z^0 decays and to fragment the quarks into hadrons.

The Peterson fragmentation scheme[34] was used for the fragmentation process. The parameter ϵ_b was 0.0035, corresponding to $\langle x_E\rangle_b = 0.72$ and $\epsilon_c = 0.024$ corresponding to $\langle x_E\rangle_c = 0.53$. These fragmentation parameters are the OPAL measured values [18] given in Section 2.3. The sensitivity of the efficiencies calculated with the above fragmentation parameters was assessed by recalculating all efficiencies using a range of choices of ϵ_q. The range used for ϵ_b was $0.009 \leq \epsilon_b \leq 0.0005$, which corresponds to a variation of $\langle x_E\rangle_b$ between 0.68 and 0.76. For charm quark fragmentation the corresponding range was $0.09 \leq \epsilon_c \leq 0.004$, or $0.48 \leq \langle x_E\rangle_c \leq 0.59$. This range of fragmentation parameters covers the range of the LEP measurements of $\langle x_E\rangle_b$ and $\langle x_E\rangle_c$ given in Section 2.3.

The efficiency for a prompt electron to satisfy the combined kinematic and

geometric requirements:

$$\begin{array}{l} > 19 \text{ space points measured in CJ} \\ p > p_{\rm low} \\ p_T > p_{T\,\rm low} \\ C_1 < |\cos\theta| < C_2 \\ |\cos\theta_{\rm thrust}| < 0.9 \\ |\cos\theta_{\rm jet}| < 0.9 \end{array} \qquad (6.5)$$

was evaluated using the simulated data. Tables 6.21 and 6.22 show the kinematic and geometric efficiencies, obtained from JETSET, for each source of prompt electrons for the requirements that were used for the measurement of $\Gamma_{Z^0\to b\bar{b}}/\Gamma_{\rm had}$ and A^b_{FB} respectively.

prompt source	kinematic and geometric efficiency
$b \to e^-$	0.0506 ± 0.0027
$b \to c \to e^+$	0.0052 ± 0.0010
$b \to c \to e^-$	0.0058 ± 0.0027
$b \to \tau \to e^-$	0.0118 ± 0.0042
$c \to e^+$	0.0084 ± 0.0008

Table 6.21: *The kinematic and geometric efficiencies for (number of CJ space points greater than 19, p> 2 GeV/c, p_T > 0.8 GeV/c, $|\cos\theta_{\rm jet}| < 0.9$, and $(0.815 < |\cos\theta| < 0.91)$, as predicted by the JETSET Monte Carlo[32]. The errors are the statistical errors due to the limited Monte Carlo statistics. These kinematic and geometric requirements were imposed for the measurement of* $\Gamma_{Z^0\to b\bar{b}}/\Gamma_{\rm had}$.

The JETSET 7.3 Monte Carlo produces the following b-flavoured hadrons; B^0_d, $B^\pm$, B^0_s, and Λ_b in the abundances; 40.5%, 40.5%, 11%, 8%. In the semileptonic decays of the B^0_d and $B^\pm$ mesons, only D or D^* charmed mesons are produced. Recent measurements by CLEO [30] suggest that approximately 30% of all B^0_d and $B^\pm$ meson semileptonic decays at the $\Upsilon(4S)$ have a D^{**} meson in the final state This deficiency in the JETSET modelling of semileptonic B decays was overcome by forcing the electron momentum spectra from JETSET B^0_d and $B^\pm$ meson semielectronic decays to reproduce the CLEO measured spectra. As it is not possible to separate the CLEO data into direct and cascade components, the three models fit by CLEO (ACM, ISGW and ISGW**) were used as the reference spectra. The ACM model was used as the central value for all efficiencies. The differences between the ACM and the other two models were used to indicate the sensitivity of the $b \to e$ efficiencies to the semileptonic decay modelling.

prompt source	kinematic and geometric efficiency
$b \to e^-$	0.110 ± 0.006
$b \to c \to e^+$	0.063 ± 0.003
$b \to c \to e^-$	0.043 ± 0.008
$b \to \tau \to e^-$	0.125 ± 0.014
$c \to e^+$	0.056 ± 0.002

Table 6.22: *The kinematic and geometric efficiencies for (number of CJ space points greater than 19, $p > 2$ GeV/c, $p_T > 0.8$ GeV/c, $|\cos\theta_{\rm thrust}| < 0.9$, $|\cos\theta_{\rm jet}| < 0.9$, and $((|\cos\theta| < 0.7)$ or $(0.815 < |\cos\theta| < 0.91))$, as predicted by the JETSET Monte Carlo[32]. The errors are the statistical errors due to the limited Monte Carlo statistics. These kinematic and geometric requirements were imposed for the measurement of $A_{\rm FB}^b$.*

The procedure used to force the JETSET momentum spectrum to reproduce the CLEO data was as follows. The kinematic and geometric efficiency for B^0_d and $B^\pm$ semielectronic decays was calculated with the original JETSET spectrum. A weight was then assigned to each B^0_d or $B^\pm$ semielectronic decay such that the distribution of the electron momentum in the parent meson rest frame reproduced the spectrum predicted by the model. The weight for each event (w) was

$$w = \frac{M(n)}{J(n)}, \tag{6.6}$$

where $M(n)$ is the model and $J(n)$ the JETSET prediction for the fraction of the total electron momentum spectrum, in the rest frame of the decaying meson, that is in the momentum region n. The momentum region was determined by the electron momentum from the JETSET simulated B decay. This procedure will be termed "reweighting" the electron momentum spectrum. Only B^0_d and $B^\pm$ to electron events were reweighted in this manner.

The ratio of the efficiencies, for $B \to e^-$, obtained by reweighting to a model and that predicted by JETSET, yielded a correction factor. This correction factor was applied to the kinematic and geometric efficiency, for $b \to e^- \overline{\nu}_e X$, calculated with JETSET including the B^0_s and Λ_b decays. The factors to correct the JETSET efficiency for $b \to e^- \overline{\nu}_e X$ were, 1.00 for the ISGW model, 0.983 for the ACM model and 0.955 for the ISGW** model, for the requirements; $nhitcj > 19$, $p > 2.0$ GeV/c, $p_T > 0.8$ GeV/c, $|\cos\theta_{\rm thrust}| < 0.9$, $|\cos\theta_{\rm jet}| < 0.9$, and $((|\cos\theta| < 0.7)$ or $(0.815 < |\cos\theta| < 0.91))$. The correction factors vary with changing momentum and transverse momentum requirements.

Since JETSET does not properly reproduce the semileptonic decay spectrum

of B mesons, it is likely that the hadronic decay spectra are not correctly modeled either. Deficiencies in reproducing these decays would affect the kinematic and geometric efficiencies calculated for the charm cascade processes. As a simple assessment of the magnitude of any possible effect, the charmed meson momentum in the B meson semileptonic decay was compared before and after reweighting the electron spectrum to the ACM model. The average charmed meson momentum in the parent B meson rest frame changed from 1.65 GeV/c to 1.66 GeV/c. A hardening of the charmed meson momentum spectrum of this magnitude would have a negligible effect on the charm cascade kinematic and geometric efficiency. Therefore no correction to the JETSET predicted efficiencies for the charm cascade process was performed.

Another shortcoming of the JETSET 7.3 Monte Carlo is the omission of $b \to u$ transitions. The CLEO collaboration has reported the branching ratio $\mathcal{B}(b \to u l \nu_l)$ to be $(0.28 \pm 0.12)\%$ in the context of the ACM model [30]. The larger b–u mass difference yields higher electron momenta in the rest frame of the decaying hadron. Figure 6.13 shoes the prediction of the ACM model for the electron spectrum for $b \to ce^-\overline{\nu_e}X$ and $b \to ue^-\overline{\nu_e}X$ decays The higher possible electron momentum implies a higher efficiency to satisfy any kinematic requirements for b to u transitions compared to b to c. The effect of the b to u transitions on the $b \to e$ kinematic and geometric efficiency was assessed using the ACM $b \to u l \nu_l$ spectrum. The efficiency for an electron from $b \to ce^-\overline{\nu_e}$ decays to satisfy the momentum and transverse momentum requirements in the lab frame in the ACM model was found. The requirement on the electron momentum in the decaying B meson rest frame that reproduced this efficiency was then applied to the ACM $b \to ue^-\overline{\nu_e}$ spectrum. This procedure implied that the kinematic efficiency for $b \to ue^-\overline{\nu_e}$ decays should be 40% larger than the corresponding $b \to ce^-\overline{\nu_e}$ efficiency. This assessment of the effect of $b \to u$ transitions assigns the full effect to the electron momentum spectrum, while the kinematic efficiency is dominated by the b hadron momentum spectrum. This should be an overestimate of any possible effect of $b \to u$ transitions. It was not possible to determine the correction factor from momentum spectra in the lab frame as $b \to ue^-\overline{\nu_e}$ events were not simulated. The CLEO measured $b \to ue^-\overline{\nu_e}$ branching ratio of $(0.28 \pm 0.12)\%$ implies that the JETSET predicted $b \to e^-\overline{\nu_e}X$ kinematic and geometric efficiency should be increased by 1.1% to account for this effect. As this is a small change, it will be used to determine the sensitivity to $b \to ue^-\overline{\nu_e}$ transitions.

JETSET 7.3 does not include radiative corrections in the decay of b-flavoured hadrons. The effect of these radiative corrections, for the semileptonic decays has been calculated by Atwood and Marciano [56]. To account for these radiative corrections, a correction factor for the JETSET predicted kinematic and geometric efficiency for $b \to e$ transitions was calculated by reweighting each B^0_d or $B^\pm$

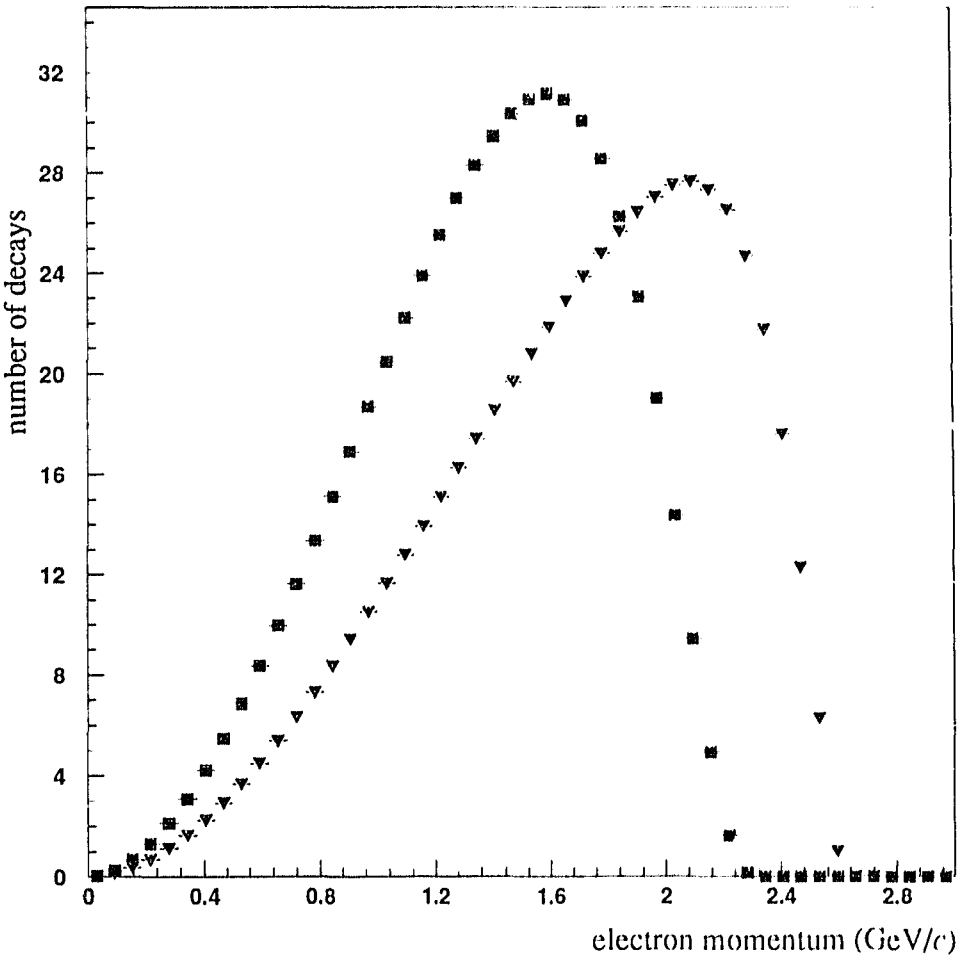

Figure 6.13: *The momentum spectrum of the decay electron in the rest frame of the decaying* B *meson, as predicted by the ACM model [31], for* $b \to ce^-\overline{\nu_e}$ *(squares)* $b \to ue^-\overline{\nu_e}$ *(triangles). Both curves are normalised to the same area. The larger electron momentum available in* $b \to ue^-\overline{\nu_e}$ *transitions is apparent.*

semileptonic decay, using the weight

$$\left(\frac{E_{\rm max}-E_{\rm e}}{cE_{\rm e}}\right)^{(2\alpha/\pi)[\ln(2E_{\rm e}/m_{\rm e})-1]}. \qquad (6.7)$$

$E_{\rm max}$ was taken to be $(m_{\rm B}^2 - m_{\rm D}^2)/2m_{\rm B}^2$ and $c = (E_{\rm max} - E_{\rm e})/E_{\rm e}$. $E_{\rm e}$ is the electron energy in the decaying B meson rest frame. Taking these radiative corrections into account decreases the JETSET predicted kinematic and geometric efficiency by 1%.

Chapter 7

$\Gamma_{Z^0\to b\bar{b}}/\Gamma_{had}$

The fraction of all hadronic Z^0 decays that produce a $b\bar{b}$ quark pair ($\Gamma_{Z^0\to b\bar{b}}/\Gamma_{had}$) can be obtained from the prompt electron rate. The number of prompt electrons present in a sample is, by definition, the sum of the number of electrons from b quark decays (direct or cascade) (N_b) and the number of electrons from c quark decays (N_c).

The number of prompt electrons produced from c quark decays in a collection of hadronic decays of the Z^0 is given by:

$$N_c = 2N_{had}\frac{\Gamma_{Z^0\to c\bar{c}}}{\Gamma_{had}}B(c\to e^+). \tag{7.1}$$

The factor $\Gamma_{Z^0\to c\bar{c}}/\Gamma_{had}$ gives the fraction of the hadronic Z^0 decays that are $c\bar{c}$ events, N_{had} is the number of hadronic events. $B(c\to e^+)$ is the average branching ratio of charmed hadrons to electrons. The factor of 2 is due to their being two primary quarks in the event and hence twice the probability of observing a prompt electron.

The number of prompt electrons produced from b quark decays is the sum of four possibilities; direct decays, the two charm cascade processes and the tau cascade process ($b\to\tau\to e^-$). The number of prompt electrons in each of these channels is given by

$$N_{b\to e^-} = 2N_{had}\frac{\Gamma_{Z^0\to b\bar{b}}}{\Gamma_{had}}B(b\to e^-) \tag{7.2}$$

$$N_{b\to c\to e^+} = 2N_{had}\frac{\Gamma_{Z^0\to b\bar{b}}}{\Gamma_{had}}B(b\to c\to e^+) \tag{7.3}$$

$$N_{b\to c\to e^-} = 2N_{had}\frac{\Gamma_{Z^0\to b\bar{b}}}{\Gamma_{had}}B(b\to c\to e^-) \tag{7.4}$$

$$N_{b\to\tau\to e^-} = 2N_{had}\frac{\Gamma_{Z^0\to b\bar{b}}}{\Gamma_{had}}B(b\to\tau\to e^-). \tag{7.5}$$

$B(b \to c \to e^+)$ and $B(b \to c \to e^-)$ are related through Equation 2.27, which implies that the reaction $b \to c \to e^-$ forms 13% of the total . arm cascade branching ratio. Since these two processes have potentially different electron momentum spectra (and therefore different efficiencies for any kinematic requirement) they have been left separate.

The number of prompt electrons is just a sum of the fi.. prompt sources. It is convenient to define the number of observable prompt electrons in a sample (N_{prompt}) as the number of prompt electrons that would satisfy the imposed kinematic and geometric requirements. Thus

$$\begin{aligned} N_{\text{prompt}} = 2N_{\text{had}} \Big[\frac{\Gamma_{Z^0\to b\bar{b}}}{\Gamma_{\text{had}}} \Big(& B(b \to e^-)\epsilon_{(b\to e^-)} \\ & + B(b \to c \to e^+)\epsilon_{(b\to c\to e^+)} \\ & + B(b \to c \to e^-)\epsilon_{(b\to c\to e^-)} \\ & + B(b \to \tau \to e^-)\epsilon_{(b\to \tau\to e^-)} \Big) \\ + \frac{\Gamma_{Z^0\to c\bar{c}}}{\Gamma_{\text{had}}} & B(c \to e^+)\epsilon_{(c\to e^+)} \Big] . \end{aligned} \tag{7.6}$$

The ϵ_i are the kinematic and geometric efficiencies for each channel. This expression may be solved for $\Gamma_{Z^0\to b\bar{b}}/\Gamma_{\text{had}}$ as:

$$\frac{\Gamma_{Z^0\to b\bar{b}}}{\Gamma_{\text{had}}} = \frac{N_{\text{prompt}} - N_{e^+(c\to e^+)}}{2N_{\text{had}}\Sigma_{Nb}} \tag{7.7}$$

$$\begin{aligned} \Sigma_{Nb} = & B(b \to e^-)\epsilon_{(b\to e^-)} \\ & + B(b \to c \to e^+)\epsilon_{(b\to c\to e^+)} \\ & + B(b \to c \to e^-)\epsilon_{(b\to c\to e^-)} \\ & + B(b \to \tau \to e^-)\epsilon_{(b\to \tau\to e^-)}]. \end{aligned} \tag{7.8}$$

With a measure of the number of observable prompt electrons in a sample of hadronic Z^0 decays, $\Gamma_{Z^0\to b\bar{b}}/\Gamma_{\text{had}}$ can be determined.

7.1 Data Sample

The OPAL multihadronic data (selected as in Section 4.1) for the 1990 and 1991 LEP runs have been analysed for this measurement of $\Gamma_{Z^0\to b\bar{b}}/\Gamma_{\text{had}}$. After requiring that the relevant portions of the detector were functioning properly when the data was recorded 484 367 multihadronic events were available and 482 101 of these events had five "good" track. to be used in the jetfinding. In these events, 629 prompt electron candidates with transverse momentum greater than 0.8 GeV/c were found using the endcap selection. Three events had two prompt electron candidates. This number is consistent with the number expected, taking into account $B(b \to e^-)$, the kinematic and geometric efficiency, and the electron selection efficiency. Table 7.1 shows the number of candidates found in the four bins of

momentum and the number of potential candidates that were removed from the sample by the photon conversion finder.

p (GeV/c)	number of candidates	number of removed conversion electrons
2–4	115	28
4–6	98	12
6–10	187	17
above 10	229	15

Table 7.1: *The number of prompt electron candidates with transverse momentum greater than 0.8 GeV/c, observed in the sample of 484 367 multihadronic events. The second column gives the number of potential candidates that were removed from the sample as being consistent with originating from photon conversions.*

By correcting the observed number of prompt electron candidates for the number of hadrons misidentified as electrons (from Section 6.2), the number of electrons from photon conversions (from Section 5.5), the number of electrons from Dalitz decays and the selection efficiency, the number of observable prompt electrons may be obtained. The correction procedure is described below.

For each bin of momentum, the expected number of misidentified hadrons present was subtracted from the total number of prompt electron candidates. In Section 6.2 the number of all identified electrons that are expected to be misidentified hadrons was determined and are shown again in Table 7.2.

In Section 5.5 the efficiency for identifying an electron originating from a photon conversion, when the electron had $p_t > 0.8$ GeV/c, was given as (0.84 ± 0.04) and the purity of the conversion electron sample is expected to be (0.65 ± 0.10). Table 7.2 shows the estimated number of electrons originating from photon conversions expected to be present in the prompt electron candidate sample. An estimated additional 0.5% of the selected prompt electron sample is electrons originating from Dalitz decays and (3 ± 1)% of all observable prompt electrons are expected to have been wrongly removed from the sample as conversion electrons.

Table 7.3 shows the number of observed prompt electrons after subtracting the misidentification and conversion backgrounds. Also shown is the number of observable prompt electrons, obtained by correcting each bin by the electron identification efficiency. 1385 ± 112.5 observable (with the endcap selection) prompt electrons were expected to be present in the sample of 484 367 multihadronic events. The error in this number is only the statistical error resulting from the number of observed electron candidates.

p (GeV/c)	number of misidentified hadrons	number of conversion electrons
2–4	(0.2 ± 0.3)	(3.46 ± 1.38)
4–6	(1.5 ± 0.4)	(1.48 ± 0.67)
6–10	(6.8 ± 0.2)	(2.10 ± 0.90)
above 10	(8.0 ± 0.7)	(1.85 ± 0.81)

Table 7.2: *The number of hadrons expected to have been misidentified as electrons and the number of remaining electrons from photon conversion.*

p (GeV/c)	observed prompt electrons	observable prompt electrons
2–4	111.3	(219.2 ± 21.1)
4–6	95.0	(201.3 ± 21.0)
6–10	178.1	(437.6 ± 33.6)
above 10	219.2	(493.6 ± 34.1)

Table 7.3: *The number of observed prompt electrons (first column). The second column shows the expected number of observable prompt electrons present in the total sample of multihadronic events. The error is the statistical error from the number of observed prompt electron candidates.*

7.2 The $\Gamma_{Z^0\to b\bar{b}}/\Gamma_{had}$ Measurement

In determining $\Gamma_{Z^0\to b\bar{b}}/\Gamma_{had}$ from Equation 7.7, the various semileptonic branching ratios must be known. The relevant kinematic and geometric efficiencies were determined in Section 6.3.

The charm semileptonic branching ratio ($B(c \to e^+)$) is taken to be an average of $B(c \to \mu^+)$ measurements [28]

$$B(c \to e^+) = (0.079 \pm 0.011). \tag{7.9}$$

This average is for an unknown mix of charmed hadrons, measured at lower centre of mass energies. The factor $\Gamma_{Z^0\to c\bar{c}}/\Gamma_{had}$ is taken to be the Standard Model prediction of 0.171 [17].

The branching ratios $B(b \to e^-)$ and $B(b \to c \to e)$ must be chosen to correspond to the appropriate B semileptonic decay model prediction. For the central value of $\Gamma_{Z^0\to b\bar{b}}/\Gamma_{had}$, the ACM model will be used. The CLEO collaboration has measured

$$B(b \to e^-) = (0.105 \pm 0.005) \tag{7.10}$$

and

$$B(b \to c \to e) = (0.097 \pm 0.010) \tag{7.11}$$

using the ACM decay model [30]. Reweighting the JETSET 7.3 $b \to e^-$ spectrum, as described in Section 6.3, to the ACM model changes the JETSET predicted kinematic and geometric efficiency by a factor of 0.979.

At the $\Upsilon(4S)$ resonance only enough energy is available to produce B^0_d and $B^\pm$ mesons. Evidence for the production of the strange b-flavoured meson B^0_s and the lightest b-flavoured baryon Λ_b has been reported [57, 58, 59, 60, 61]. It is possible that these heavier b-flavoured hadrons have different semileptonic branchings than the light B mesons. The Spectator Model predicts that all hadrons containing b quarks (and not the postulated t quark) should have the same semileptonic branchings. This expectation will be assumed, however an error of 25% on the semileptonic branching fractions of these two heavy b-flavoured hadrons will be assigned. The JETSET 7.3 Monte Carlo estimates that approximately 11% of all primary b quarks will fragment into a B^0_s meson and approximately 8% to the baryon Λ_b. Thus an additional 25% error on $B(b \to e^-)$ is assigned to 19% of the total $b \to e^-$ sample, giving $B(b \to e^-) = (10.5 \pm 0.6)\%$ for the ACM model.

The presence of B^0_s and Λ_b may also modify the cascade branching ratio $B(b \to c \to e^+)$. To assess the magnitude of the effect of these heavy b hadrons on the charm cascade rate it will be assumed that B^0_s decays to $D^\pm_s$ 100% of the time and that Λ_b decays to Λ_c 100% of the time. Equation 2.15 can be used to relate the uncertain $D^\pm_s$ and Λ_c semileptonic branching ratios to the known D meson semileptonic branching ratios. The lifetimes of the $D^\pm_s$ and Λ_c have been measured to be [28]

$$\tau_{D^\pm_s} = (4.45^{+0.38}_{-0.29}) \times 10^{-13} \text{ s} \tag{7.12}$$

$$\tau_{\Lambda_c} = (1.91^{+0.17}_{-0.13}) \times 10^{-13} \text{ s}. \tag{7.13}$$

Using Equation 2.15 and taking the D^0 meson as the reference the various semileptonic branching ratios may be written as :

$$B(D^\pm \to e^+ \nu_e X) = 2.52 B(D^0 \to e^+ \nu_e X) \tag{7.14}$$

$$B(D^+_s \to e^+ \nu_e X) = 1.06 B(D^0 \to e^+ \nu_e X) \tag{7.15}$$

$$B(\Lambda_c \to e^+ \nu_e X) = 0.454 B(D^0 \to e^+ \nu_e X). \tag{7.16}$$

The CLEO collaboration has measured the inclusive B decay rates at the $\Upsilon(4S)$ to be [62]

$$B(B \to D^0 X) = 0.55 \pm 0.03 \tag{7.17}$$

$$B(B \to D^+ X) = 0.25 \pm 0.05 \tag{7.18}$$

$$B(B \to D^+_s X) = 0.10 \pm 0.04 \tag{7.19}$$

$$B(B \to \Lambda_c X) = 0.064 \pm 0.011. \tag{7.20}$$

Using these inclusive rates, the charm cascade branching fraction at the $\Upsilon(4S)$ resonance may be written in terms of the branching ratio $B(D^0 \to e^- \nu_e X)$ as $B(b \to c \to e^+) = 1.315 B(D^0 \to e^+ \nu_e X)$. In the above calculation the $(1.12 \pm 0.18)\%$ of $B \to J/\psi$ decays, measured by CLEO have been ignored.

Using the above assumption on the B^0_s and Λ_b decays, the expected branching ratio at centre of mass energies near the Z^0 resonance may be written as $B(b \to c \to e^+) = 1.218 B(D^0 \to e^+ \nu_e X)$. In deriving this, it has been assumed that 81% of all decays are those measurable by CLEO, 11% are from B^0_s and 8% arise from Λ_b. Thus $B(b \to c \to e^+)$ at centre of mass energies near m_{Z^0} can be related to $B(b \to c \to e^+)$ measured at the $\Upsilon(4S)$ resonance by

$$\frac{B(b \to c \to e^+)_{\rm LEP}}{B(b \to c \to e^+)_{\Upsilon(4S)}} = \frac{1.218}{1.315} = 0.926. \tag{7.21}$$

In all calculations using this factor, an error equal to 100% of the induced change is quoted (i.e. 0.926 ± 0.073). This error should cover all the possible extremes in the correction.

The τ cascade branching ratio $B(b \to \tau \to e^-)$ was derived as the product of $B(\tau^- \to e^-) = 0.177 \pm 0.004$ [28] and $B(b \to \tau^-)/B(b \to e^-) = 0.25 \pm 0.10$. The last factor was derived using the phase space formulas given in [29]. The error is derived by varying the b quark mass from 5.0 GeV/c^2 in the range $4.7 < m_b < 5.3$ GeV/c^2 and the charm quark mass in the range $1.3 < m_c < 1.7$ GeV/c^2 from a central value of 1.5 GeV/c^2.

The individual terms in Equation 7.7 are then:

$$N_{\rm prompt} = 1385 \pm 112 \tag{7.22}$$

$$N_c \epsilon_{(c \to e^+)} = 109.9 \tag{7.23}$$

$$2N_{\rm had} B(b \to e^-) \epsilon_{(b \to e^-)} = 5042.3 \tag{7.24}$$

$$2N_{\rm had} B(b \to c \to e^+) \epsilon_{(b \to c \to e^+)} = 391.3 \tag{7.25}$$

$$2N_{\rm had} B(b \to c \to e^-) \epsilon_{(b \to c \to e^-)} = 70.5 \tag{7.26}$$

$$2N_{\rm had} B(b \to \tau \to e^-) \epsilon_{(b \to \tau \to e^-)} = 52.8 \tag{7.27}$$

and thus

$$\frac{\Gamma_{Z^0 \to b\bar{b}}}{\Gamma_{\rm had}} = 0.230 \pm 0.020, \tag{7.28}$$

where the error is statistical only.

7.3 Systematic Errors

The sensitivity of the measurement of $\Gamma_{Z^0 \to b\bar{b}}/\Gamma_{\rm had}$ to possible systematic effects is discussed below.

In determining the number of prompt electrons expected from each source, the branching ratios $B(b \to e^-)$, $B(b \to c \to e)$, $B(b \to \tau \to e^-)$ and $B(c \to e^+)$ were needed. The most precise measurements of the first two come from measurements at the $\Upsilon(4S)$ resonance[1]. These measurements of the b semileptonic branching ratios use theoretical models to extrapolate the lepton spectra to low momenta and to attribute parts of the lepton spectra to direct and cascade components. Such an extrapolation is shown in Figure 2.12. The theoretical curves, fitted to the data, are then used to obtain the semileptonic branching ratios $B(b \to l)$, $B(b \to c \to l)$ and $B(b \to ul)$. Different theories may fit the data equally well in the measured region, but predict different low momentum behaviour and therefore different branching ratios. The constraint on the models is that the observed total rate of prompt leptons must be reproduced; i.e.: $B(b \to e^-)\epsilon_{(b\to e^-)} + B(b \to c \to e)\epsilon_{(b\to c\to e^+)}$ is fixed. This constraint may be used to reduce the sensitivity of the measurement of $\Gamma_{Z^0\to b\bar{b}}/\Gamma_{had}$ to b semileptonic decay modelling if the branching ratios measured with a particular model are used together with the momentum spectrum predicted by that model. The CLEO collaboration has reported a measurement of $B(b \to l)$, $B(b \to c \to l)$ and $B(b \to ul)$ that separates the modelling uncertainties from the other sources of error. These other sources of error include the statistical error on the fit, continuum subtraction, efficiencies etc. and will be termed "intrinsic" (to CLEO) errors hereafter.

The sensitivity of the determination of $\Gamma_{Z^0\to b\bar{b}}/\Gamma_{had}$ to the semileptonic decay modelling was determined by recalculating $\epsilon_{(b\to e^-)}$ after reweighting the JETSET electron momentum spectrum to agree with the ISGW and ISGW** models, as described in Section 6.3. The semileptonic branching ratios appropriate to each model were then used to determine the number of observable electrons from each source. Using the ISGW model, $\Gamma_{Z^0\to b\bar{b}}/\Gamma_{had}$ was 0.234 while 0.224 was found with ISGW** model. A systematic error of ± 0.006 is thus added to the error on $\Gamma_{Z^0\to b\bar{b}}/\Gamma_{had}$ to account for the b semileptonic decay modelling error.

The intrinsic error in $B(b \to e^-) = (10.5 \pm 0.6)\%$ contributes an error of 0.012 on $\Gamma_{Z^0\to b\bar{b}}/\Gamma_{had}$.

The CLEO measurement of $B(b \to c \to l)$, in the context of the ACM model, was $B(b \to c \to l) = (9.7 \pm 1.0)\%$. The error in this parameter contributes 0.002 to the systematic error on $\Gamma_{Z^0\to b\bar{b}}/\Gamma_{had}$.

To account for the different branching ratio $B(b \to c \to e^+)$ at $\sqrt{s} \approx m_{Z^0}$, due to the different mix of b hadrons from that present in $\Upsilon(4S)$ decays, the CLEO measured branching ratio of $B(b \to c \to l)$ was multiplied by the factor 0.926 ± 0.074 to obtain $B(b \to c \to e^+)$ at LEP. The uncertainty in this factor contributes 0.001 to the systematic error in $\Gamma_{Z^0\to b\bar{b}}/\Gamma_{had}$.

[1]There is a measurement of this quantity at LEP $B(b \to l) = 0.113 \pm 0.010 \pm 0.006$ [23], however it is not clear how this measurement is affected by b semileptonic decay modelling.

The process $b \rightarrow c \rightarrow e^-$ has been assumed to contribute 13% of the total charm cascade rate. Varying this rate between 9% and 17% (corresponding to varying $B(b \rightarrow c)/B(b \rightarrow cX)$ between 10% and 20%) induces a negligible change on $\Gamma_{Z^0 \rightarrow b\bar{b}}/\Gamma_{had}$. If m_b is varied between 4.7 and 5.3 GeV/c^2 and m_c is varied between 1.3 and 1.7 GeV/c^2 in the phase space formulae leading to Equation 2.27, $\Gamma(b \rightarrow c(s\bar{c}) + c(d\bar{c}))/\Gamma(b \rightarrow cX)$ varies between 9% and 17%.

The branching ratio $B(b \rightarrow \tau \rightarrow e^-)$ has been taken to be $(0.044 \pm 0.018) B(b \rightarrow e^-)$. The error in this branching ratio contributes 0.001 to the systematic error on $\Gamma_{Z^0 \rightarrow b\bar{b}}/\Gamma_{had}$.

The presence of $b \rightarrow ue^-$ transitions will affect the kinematic and geometric efficiency for $b \rightarrow e^-$ as discussed in Section 6.3. Increasing the kinematic and geometric efficiency for $b \rightarrow e^-$ to account for the possibility of $b \rightarrow ue^-$ transitions changes the derived $\Gamma_{Z^0 \rightarrow b\bar{b}}/\Gamma_{had}$ value by 0.003, which is added to the systematic error.

Radiative corrections in $b \rightarrow e^-$ transitions soften the electron momentum spectrum and therefore lower $\epsilon_{(b \rightarrow e^-)}$. In principle, radiative corrections of this kind should also affect the cascade (and charm) processes as well, however the exact nature of these corrections has not been determined for these channels here. Incorporating the radiative corrections to the process $b \rightarrow e^-$, as described in Section 6.3, changes the resulting $\Gamma_{Z^0 \rightarrow b\bar{b}}/\Gamma_{had}$ value by 0.002 and is added to the systematic error.

$B(c \rightarrow e^+)$ was taken to be $(7.9 \pm 1.1)\%$. The error in this branching ratio contributes 0.003 to the systematic error on $\Gamma_{Z^0 \rightarrow b\bar{b}}/\Gamma_{had}$.

In calculating the expected number of prompt electrons from direct charm decays, the Standard Model value for $\Gamma_{Z^0 \rightarrow c\bar{c}}/\Gamma_{had}$ of 0.171 was used. Varying the top quark mass between 82 and 177 GeV/c^2 produces a negligible change in this value. There are measurements of this quantity [18, 24, 63, 64] which are all consistent with the Standard Model prediction. Since it is not the aim here, nor is it entirely possible, to determine $\Gamma_{Z^0 \rightarrow b\bar{b}}/\Gamma_{had}$ independent of input from the Standard Model, no error on the assumed value of $\Gamma_{Z^0 \rightarrow c\bar{c}}/\Gamma_{had}$ is assessed. The dependence of the obtained $\Gamma_{Z^0 \rightarrow b\bar{b}}/\Gamma_{had}$ value on the assumed value of $\Gamma_{Z^0 \rightarrow c\bar{c}}/\Gamma_{had}$ can be expressed as

$$\Delta\left(\frac{\Gamma_{Z^0 \rightarrow b\bar{b}}}{\Gamma_{had}}\right) = -0.02\Delta\left(\frac{\Gamma_{Z^0 \rightarrow c\bar{c}}}{\Gamma_{had}}\right), \tag{7.29}$$

where $\Delta(\frac{\Gamma_{Z^0 \rightarrow c\bar{c}}}{\Gamma_{had}})$ is the difference from the assumed value of 0.171 for $\Gamma_{Z^0 \rightarrow c\bar{c}}/\Gamma_{had}$.

The uncertainty in the ϵ_i arising from the limited Monte Carlo statistics contributes 0.016 to the systematic error on $\Gamma_{Z^0 \rightarrow b\bar{b}}/\Gamma_{had}$.

The sensitivity of the derived value of $\Gamma_{Z^0 \rightarrow b\bar{b}}/\Gamma_{had}$ to b quark fragmentation was assessed by varying $\langle x_E \rangle_b$ from the central value of 0.72 to the extremes of 0.68 and 0.76. Within this range of $\langle x_E \rangle_b$ values, the derived value of $\Gamma_{Z^0 \rightarrow b\bar{b}}/\Gamma_{had}$

changed by 0.010, which is added to the systematic error to account for b quark fragmentation.

$\langle x_E \rangle_c$ was varied between 0.48 and 0.59 from the central value of 0.53 to assess the sensitivity of the $\Gamma_{Z^0\to b\bar{b}}/\Gamma_{had}$ determination to charm quark fragmentation. A change of 0.007 was observed and is added to the systematic error on $\Gamma_{Z^0\to b\bar{b}}/\Gamma_{had}$.

The uncertainty in the number of hadrons misidentified as prompt electrons amounts to (± 3.2) in N_{prompt}. This results in an uncertainty of 0.001 in $\Gamma_{Z^0\to b\bar{b}}/\Gamma_{had}$ which is added to the systematic error.

The uncertainties in the efficiency and purity of the photon conversion finder algorithm results in a systematic error of 0.001 in $\Gamma_{Z^0\to b\bar{b}}/\Gamma_{had}$. The uncertainty in the number of prompt electrons wrongly flagged as electrons from photon conversions $(3 \pm 1)\%$ contributes 0.002 to the systematic error on $\Gamma_{Z^0\to b\bar{b}}/\Gamma_{had}$.

The error on the prompt electron selection efficiency results in an uncertainty of (± 119.9) in N_{prompt}. This corresponds to an uncertainty of 0.002 on $\Gamma_{Z^0\to b\bar{b}}/\Gamma_{had}$ which is added to the systematic error. This error is dominated by the uncertainty on the efficiency of the $N\sigma_{dE/dx}$ requirement.

The 0.1% each of $e^+e^- \to \tau^+\tau^-$ and $e^+e^- \to \gamma\gamma$ events estimated to contaminate the multihadron selection produce a negligible uncertainty in the $\Gamma_{Z^0\to b\bar{b}}/\Gamma_{had}$ determination. The inefficiency of the jetfinding requirement of five "good" tracks also contributes negligibly to the error on $\Gamma_{Z^0\to b\bar{b}}/\Gamma_{had}$.

Table 7.4 shows the various contributions to the systematic error on $\Gamma_{Z^0\to b\bar{b}}/\Gamma_{had}$.

As a check on the stability of this result with increasing p_T requirements, $\Gamma_{Z^0\to b\bar{b}}/\Gamma_{had}$ was calculated using the electron identification efficiencies the misidentification rates and the numbers of observed prompt electron candidates for $p_T > 1.0$ GeV/c, given in Chapter 6. A value of

$$\frac{\Gamma_{Z^0\to b\bar{b}}}{\Gamma_{had}} = 0.226 \pm 0.022,$$

where the error is statistical only, was obtained[2]. This is in good agreement with the value obtained for $p_T > 0.8$ GeV/c (Equation 7.30).

7.4 Summary

From the number of prompt electrons observed in 484 367 multihadronic events, the ratio of the partial width of the Z^0 boson to b quarks to the hadronic width is

[2]The number of prompt electron candidates removed as consistent with arising from photon conversions was 12(2–4) GeV/c, 6(4–6) GeV/c, 9(6–10) GeV/c and 10(above 10) GeV/c. The kinematic and geometric efficiencies, calculated as in Section 6.3, for $p_T > 1.0$ GeV/c are: $\tilde{\epsilon}_{(b\to e^-)} = 0.038$, $\epsilon_{(b\to c\to e^+)} = 0.0019$, $\epsilon_{(b\to c\to e^-)} = 0.0058$, $\epsilon_{(b\to\tau\to e^-)} = 0.0088$ and $\tilde{\epsilon}_{(c\to e^+)} = 0.0049$. The value of $\epsilon_{(b\to e^-)}$ has been corrected to agree with the ACM model.

Error Source	Contribution
b decay modelling	0.006
$B(\mathrm{b} \to \mathrm{e}^-)$ error	0.012
$B(\mathrm{b} \to \mathrm{c} \to \mathrm{e})$ error	0.002
$B(\mathrm{b} \to \mathrm{c} \to \mathrm{e}^+)$ correction	0.001
$B(\mathrm{b} \to \tau \to \mathrm{e}^-)$ uncertainty	0.001
$\mathrm{b} \to \mathrm{ue}^-\overline{\nu_\mathrm{e}}$	0.003
radiative corrections	0.002
$B(\mathrm{c} \to \mathrm{e}^+)$ error	0.003
Monte Carlo statistics	0.016
b fragmentation	0.010
c fragmentation	0.007
misidentified hadrons	0.001
conversion efficiency	0.001
conversion purity	0.002
selection efficiency	0.022
Total	0.033

Table 7.4: *The sources of systematic error in the determination of* $\Gamma_{\mathrm{Z^0 \to b\overline{b}}}/\Gamma_{\mathrm{had}}$ *and their contributions to the total error.*

determined to be

$$\frac{\Gamma_{\mathrm{Z^0 \to b\overline{b}}}}{\Gamma_{\mathrm{had}}} = (0.230 \pm 0.020 \pm 0.033). \tag{7.30}$$

Using $\Gamma_{\mathrm{had}} = (1.740 \pm 0.012)$ GeV [25], then

$$\Gamma_{\mathrm{b\overline{b}}} = (400 \pm 35 \pm 57 \pm 3) \text{ MeV} \tag{7.31}$$

where the errors are statistical, systematic and due to the error in Γ_{had} respectively. This value is in good agreement with the Standard Model prediction of 376 MeV [17] and with the previous determinations cited in Section 2.1.

It should be stressed that in obtaining this value of $\Gamma_{\mathrm{Z^0 \to b\overline{b}}}/\Gamma_{\mathrm{had}}$ from the observed number of prompt electrons it has been assumed that the semileptonic branching ratios for $\mathrm{B^0_s}$ and Λ_b are the same as for $\mathrm{B^0_d}$ and $\mathrm{B^\pm}$. This assumption has, in part, been made to be able to take advantage of the reported CLEO lepton spectra to reduce the uncertainty due to b hadron decay modelling. When fully reconstructed events are used to determine the lepton spectrum from direct B decays, reliance on theoretical models should be reduced.

Chapter 8

The b Quark Forward-Backward Asymmetry

Only data collected between centre of mass energies of 90.7 and 91.6 GeV were used for the forward-backward asymmetry measurement This corresponds roughly to the peak in the cross section for $e^+e^- \to Z^0 \to X$ (see Section 2.1). The choice of the centre of mass energy was made to avoid complications associated with the energy dependence of A_{FB}^b and A_{FB}^c (see Figure 2.3). After requiring that the detector was functioning properly, 320 706 multihadronic events were available. This number of hadronic Z^0 decays corresponds to an integrated luminosity of approximately 11 pb^{-1}. In these events, 5167 prompt electron candidates were selected, of which 4697 were within the barrel selection and 470 within the endcap selection. The method used to measure the b quark forward-backward asymmetry using this sample is described below.

8.1 The Asymmetry Measurement

The angular distribution of prompt electrons, before any detector effects is:

$$\begin{aligned}\frac{d\sigma_{\text{prompt}}}{d\cos\theta} &= C\Big(f_{(b\to e^-)}[1+x^2+\tfrac{8}{3}A_{FB}^b x] \\ &+f_{(b\to c\to e^+)}[1+x^2-\tfrac{8}{3}A_{FB}^b x] \\ &+f_{(b\to c\to e^-)}[1+x^2+\tfrac{8}{3}A_{FB}^b x] \\ &+f_{(b\to\tau\to e^-)}[1+x^2+\tfrac{8}{3}A_{FB}^b x] \\ &+f_{(c\to e^+)}[1+x^2-\tfrac{8}{3}A_{FB}^c x]\Big).\end{aligned} \tag{8.1}$$

$x = -Q\cos\theta_{\text{thrust}}$, with $\cos\theta_{\text{thrust}}$ defined as in Section 2.3 and Q is the charge of the observed electron. A_{FB}^b is the b quark forward-backward asymmetry and A_{FB}^c is the corresponding charm asymmetry. The sign of the linear term reflects the product of the observed lepton charge and the quark charge. The f_i are the

fractions of the prompt electron signal from each source that satisfy the kinematic requirements.

The angular distribution in Equation 8.1 is modified by detector acceptance and the presence of non prompt background. The angular distribution of prompt electrons candidates ($G(x)$) can be written as:

$$\begin{aligned} G(x) &= C'\Big(\epsilon_{(b\to e^-)}(x)[1+x^2+\tfrac{8}{3}A^b_{FB}x] \\ &+\epsilon_{(b\to c\to e^+)}(x)[1+x^2-\tfrac{8}{3}A^b_{FB}x] \\ &+\epsilon_{(b\to c\to e^-)}(x)[1+x^2+\tfrac{8}{3}A^b_{FB}x] \\ &+\epsilon_{(b\to \tau\to e^-)}(x)[1+x^2+\tfrac{8}{3}A^b_{FB}x] \\ &+\epsilon_{(c\to e^+)}(x)[1+x^2-\tfrac{8}{3}A^c_{FB}x] \\ &+\epsilon_{(misID)}(x)[1+x^2] \\ &+\epsilon_{(conv)}(x)[1+x^2]\Big). \end{aligned} \tag{8.2}$$

The $\epsilon_i(x)$ are the acceptances for each source of prompt electron candidates. "misID" refers to hadrons misidentified as electrons and "conv" to electrons from photon conversions. Figure 8.1 shows the observed $-Q\cos\theta_{thrust}$ distribution for all prompt electron candidates with momentum greater than 2 GeV/c and transverse momentum greater than 0.8 GeV/c.

Equation 8.2 assumes that the conversion and misidentification backgrounds have no asymmetry. This a safe assumption barring any detector induced asymmetries. The main source of photons is the decay of short lived neutral particles (π^0,η) and therefore do not have a charge asymmetry. There is the possibility of an asymmetry of the misidentification background. Leading particles in jets may carry the flavour (charge), and hence the asymmetry of the primary quark. The inherent asymmetry of leading tracks in multihadronic events (selected to have high momentum and low transverse momentum) has been measured in OPAL to be (0.040 ± 0.007) [65]. Since the electron selection criteria select tracks with high transverse momenta, it is unlikely that leading particles are selected preferentially.

The observed asymmetry $((N(x>0)-N(x<0))/(N(x>0)+N(x<0)))$ of electrons from photon conversions, selected to satisfy the momentum and transverse momentum requirements, was measured to be (-0.006 ± 0.013). This asymmetry is consistent with the zero expected. Since no electron selection criteria, besides the p and p_T requirements, were applied to this conversion sample, this is an indication of the actual parent distribution asymmetry.

The asymmetry of the misidentified hadron background was measured with the same techniques used to measure the number of hadrons in the final sample. The forward-backward asymmetry of particles that satisfied all of the electron selection criteria, except the E/p (or E_{cone}/p) requirement, which was placed at $0.2 < E/p < 0.6$, was (-0.014 ± 0.034). This is again consistent with the zero asymmetry expected. $N\sigma_{dE/dx}$ was not used to select this test sample, as a

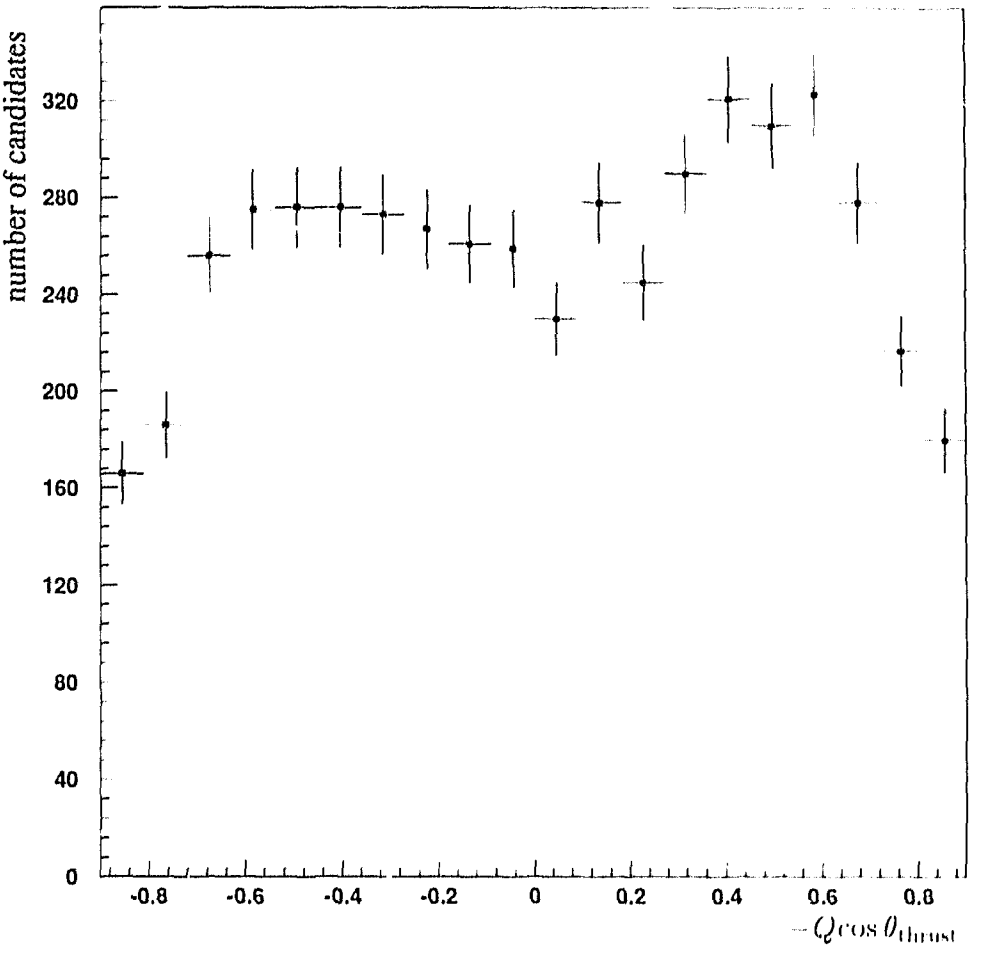

Figure 8.1: *The distribution of $-Q\cos\theta_{\rm thrust}$ for all prompt electron candidates with $p_T > 0.8$ GeV/c and $p > 2$ GeV/c. The effect of the complicated detector acceptance and the asymmetry of the distribution is evident.*

selection that biases against electrons using the $N\sigma_{dE/dx}$ distribution would bias against high momentum particles (high momentum particles have dE/dx values approaching that of electrons). It is these high momentum particles that are expected to carry any possible asymmetry. The E/p selection does not have a significant momentum bias. The lower E/p requirement was not zero, so as to avoid selecting prompt muons that would have a measurable asymmetry. These muons definitely do not satisfy the E/p criteria and are not present in the prompt electron sample.

Equation 8.2 assumes that electrons from photon conversions are produced as $(1 + x^2)$. While photons are produced as $(1 + x^2)$, the probability that a photon will convert into an e^+e^- pair is not constant in $|x|$, due to the variation in the material in the detector with $\cos\theta$. The distribution of conversion electrons as a function of $|x|$ was measured using the sample of tagged conversions used to measure the conversion asymmetry. Figure 8.2 shows the distribution and the best fit line $(1 + 1.7x^2)$. The sensitivity of the asymmetry measurement to the assumed conversion angular distribution is discussed in Section 8.2.

If the acceptances, $\epsilon_i(x)$, for each source of prompt electron candidate have the same x dependence, i.e.

$$\frac{\epsilon_i(x)}{\epsilon_{(b\to e^-)}(x)} = \frac{F_i}{F_{(b\to e^-)}}, \tag{8.3}$$

then Equation 8.2 may be rewritten as

$$G(x) = C''\epsilon(x)[1 + x^2 + \frac{8}{3}A^{obs}x], \tag{8.4}$$

with $\epsilon(x) \equiv \epsilon_{(b\to e^-)}(x)$. A^{obs} is the observed asymmetry in the prompt electron sample. In deriving this expression use was made of the condition

$$\sum_i F_i = 1, \tag{8.5}$$

which states that all sources of prompt electron candidates have been considered. The F_i are the fraction of prompt electron candidates from each source that satisfies the kinematic and geometric and electron identification criteria. A^b_{FB} is then related to A^{obs} through

$$A^b_{FB} = \frac{A^{obs} + F_{(c\to e^+)}A^c_{FB}}{F_{(b\to e^-)} - F_{(b\to c\to e^+)} + F_{(b\to c\to e^-)} + F_{(b\to\tau\to e^-)}}. \tag{8.6}$$

In Equation 8.4 it has been assumed that the variations with x of the acceptances for all sources of prompt electrons are the same, for electrons from photon conversions and misidentified hadrons this assumption may be tested directly. The

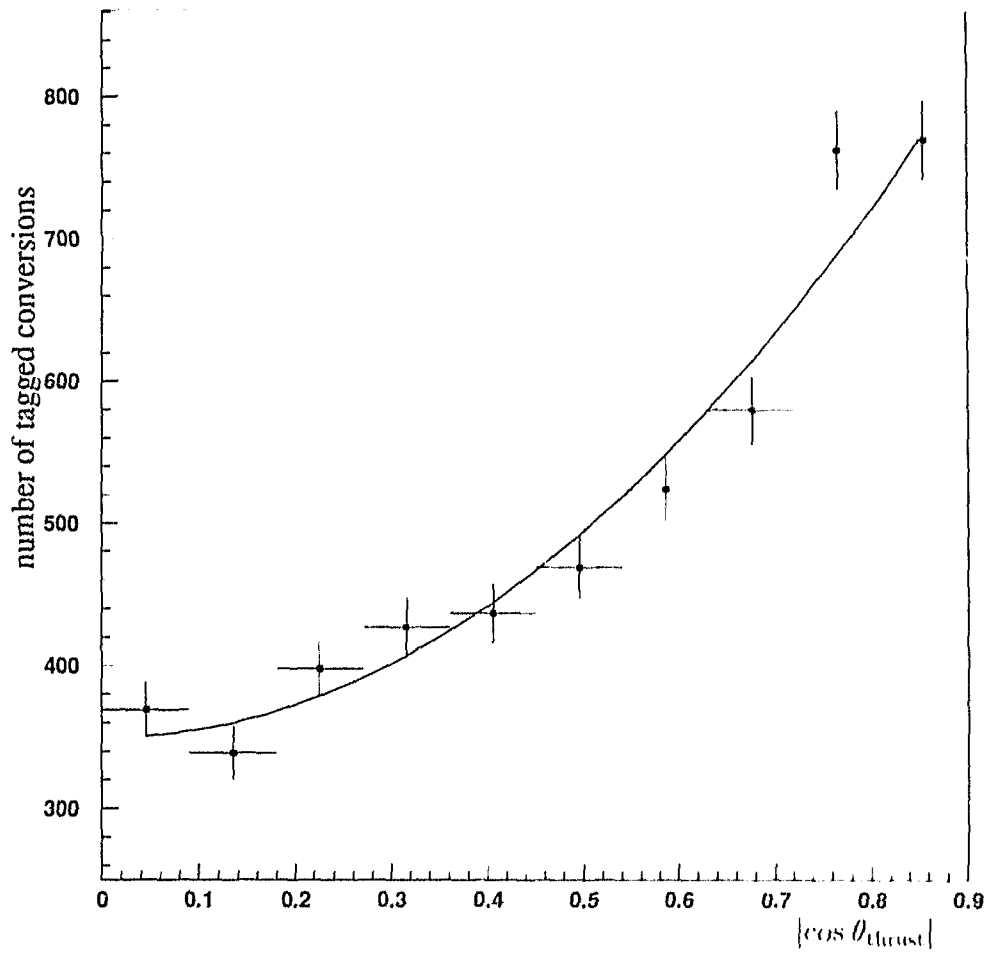

Figure 8.2: *The number of identified electrons from photon conversions as a function of* $|\cos\theta_{\rm thrust}|$. *No prompt electron selection criteria have been applied to this sample, except the* p *and* p_T *requirements. The line is* $(1 + 1.7\cos^2\theta_{\rm thrust})$.

fraction of the prompt electron sample that was expected to be electrons from photon conversion was determined in three regions of $|x|$. Table 8.1 shows that the fraction of the prompt electron sample that is expected to be conversion electrons is constant in $|x|$, after correcting for the $(1 + 1.7x^2)$ angular distribution of the conversion electrons. This shows directly that the acceptance for conversions has the same $|x|$ dependence as the prompt electrons.

$\lvert\cos\theta_{\rm thrust}\rvert$	uncorrected fraction	corrected fraction
0–0.25	(0.019 ± 0.005)	(0.019 ± 0.005)
0.25–0.7	(0.022 ± 0.006)	(0.019 ± 0.005)
0.7–0.9	(0.024 ± 0.006)	(0.019 ± 0.005)

Table 8.1: *The fraction of the prompt electron sample that is expected to be electrons from photon conversions in three regions of* $|\cos\theta_{\rm thrust}|$. *The uncorrected fraction is the fraction calculated from the number of prompt electron candidates rejected as photon conversions. The corrected fraction is the uncorrected fraction multiplied by* $(1 + \cos^2\theta_{\rm thrust})/(1 + 1.7\cos^2\theta_{\rm thrust})$ *to account for the original angular distribution of the conversion electrons.*

In Section 6.2 the variation with $|x|$ of the fraction of hadrons misidentified as electrons was determined. This fraction varies from 5.4% at $|x| \approx 0.0$ to 2.5% at $|x| \approx 0.9$. The sensitivity of the asymmetry measurement to this variation is assessed in Section 8.2.

Since it is not possible to separate the tagged prompt electrons into the different sources, there is no direct means to establish the relative acceptance variations. A first indication that the $|x|$ variation of the acceptances for prompt sources is the same, comes from the conversion sample. Of all the sources of prompt electron candidates, conversion electrons are expected to be the least isolated, since the parent particle is created in the fragmentation process and has a high probability to be in the jet core and there is only a small chance that the resulting electron will be separated from the other particles in the jet. The acceptance for the conversion electrons was measured to be the same function of $|x|$ as the other prompt sources. This provides an indication that the acceptance for all prompt sources should have the same $|x|$ variation.

Simulated data may also be used to determine the relative acceptance variations of the prompt sources. Figure 8.3 shows the ratio of the number of electrons from the different sources to the number from $b \to e$ selected with the electron identification criteria in the simulated data. These ratios are consistent with being constant.

It should be noted that it has not been assumed that the absolute selection

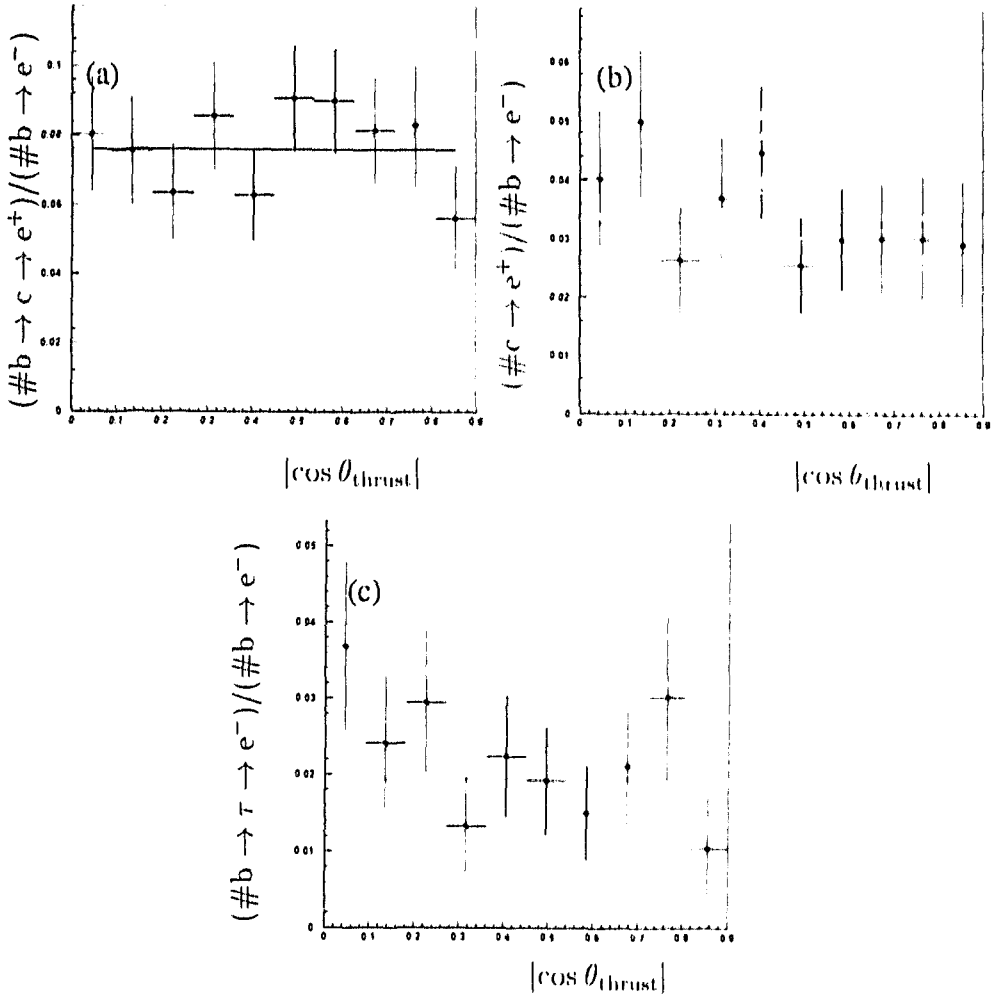

Figure 8.3: *The ratio of the number of electrons identified in simulated data for each prompt source to the number of electrons identified from direct b decay. (a)* $b \to c \to e$ *(b)* $c \to e$ *(c)* $b \to \tau \to e$.

efficiency for each source of prompt electron candidates is the same. What has been assumed is that the variation of the relative efficiencies with x is the same for all sources of prompt electrons. Any differences in the overall selection efficiency between the different physics channels may be absorbed in the F_i.

In obtaining the asymmetry ($A^{\rm obs}$) of the distribution of the prompt electron candidates, it will be assumed that $\epsilon(x) = \epsilon(-x)$. This is equivalent to stating that the acceptance is the same for positive and negative charges at the same $\cos\theta$. This is the case for large enough track momenta. At low (< 1 GeV/c) momenta, there is a tendency for negative charges to satisfy criteria on the number of CJ measured space points more often than positive charges. This arises primarily because of the Lorentz angle in CJ. Tracks which cross anode planes parallel to the drift direction (positive charges) will have a smaller maximum number of CJ track samples than oppositely charged tracks at the same momentum. Figure 8.4(a) shows the distribution of CJ measured space points for negative and positive charged tracks, with no momentum requirement. Figure 8.4(b) shows the same distributions with a minimum momentum criteria of 2 GeV/c applied to the tracks. The differences in the number of CJ samples in the region of 20 disappears at these higher momenta. (The sagitta for a 2 GeV/c track at $|\cos\theta| = 0$ is approximately 2 cm.) Of the 5167 candidate electrons, 2563 had positive charge and 2604 had negative charge. No overall charge asymmetry in the selection is thus expected.

If the acceptance, $\epsilon(x)$, is even in x, then the normalisation C'' in Equation 8.4 is independent of $A^{\rm obs}$ and the $A^{\rm obs}x$ term contains all of the asymmetry of the distribution. The right hand side of Equation 8.4 can then be used as a likelihood function and $A^{\rm obs}$ can be obtained by maximising

$$\prod_j C''\epsilon(x_j)[1 + x_j^2 + \frac{8}{3}A^{\rm obs}x_j]. \tag{8.7}$$

The product over j implies a product over all electron candidates. Since $\epsilon(x)$ and C'' are unknown, the maximum of the log of Equation 8.7

$$\sum_j \ln[C''\epsilon(x_j)] + \sum_j \ln[1 + x_j^2 + \frac{8}{3}A^{\rm obs}x_j] \tag{8.8}$$

may be obtained instead. For a given set of events the sum $\sum_j \ln[C''\epsilon(x_j)]$ is a constant and therefore the maximum of Equation 8.8 occurs when

$$\sum_j \ln[1 + x_j^2 + \frac{8}{3}A^{\rm obs}x_j] \tag{8.9}$$

is maximum. In Equation 8.9, $A^{\rm obs}$ is the only free parameter.

For the prompt electron data, taken at centre of mass energies between 90.7 GeV/c and 91.6 GeV/c the maximum of Equation 8.9 occurred at

$$A^{\rm obs} = 0.0473 \pm 0.0147. \tag{8.10}$$

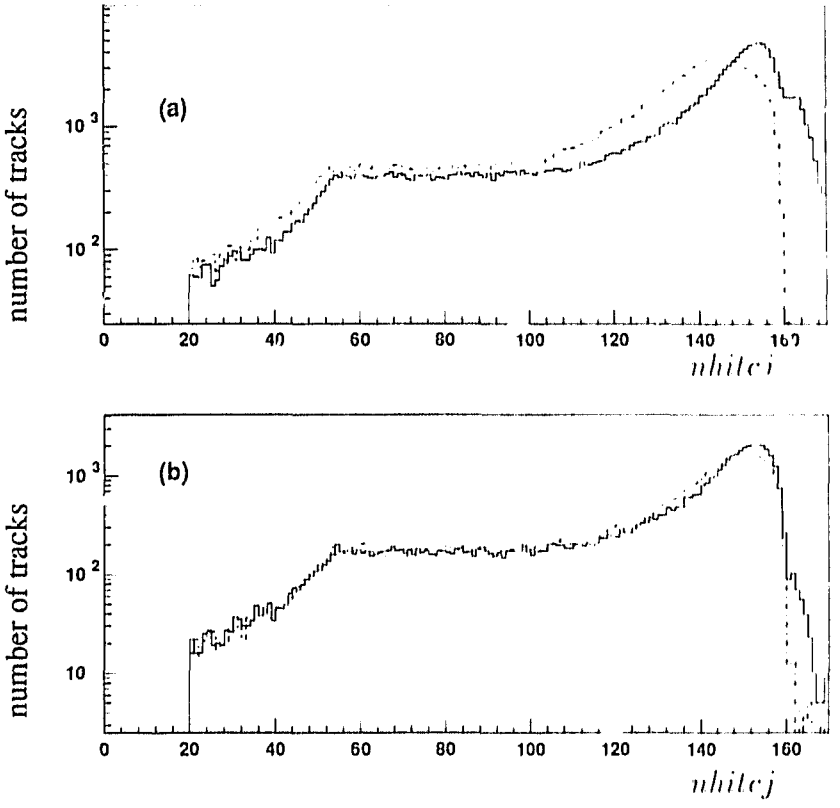

Figure 8.4: *(a)The distribution of the number of CJ samples used in the track fit, for all momenta, for negative (solid line) and positive (dashed line) charges. The differences in the distributions arise from Lorentz angle effects in CJ. (b) shows the same distribution, except with a minimum momentum requirement of 2 GeV/c on the tracks. The distributions are similar, except at large numbers of samples*

The error is the statistical error on the maximum. Figure 8.5 shows the distribution

$$\frac{N(|x|) - N(-|x|)}{N(|x|) + N(-|x|)} = \frac{8}{3}\frac{A^{\rm obs}x}{1+x^2} \tag{8.11}$$

with the curve corresponding to $A^{\rm obs} = 0.0473$ and the 1σ contours from the likelihood fit. Clearly the data are inconsistent with zero asymmetry (the $\chi^2/dof = 1.9$ for no asymmetry, excluding zero asymmetry at the 95% confidence level), which would imply a line at 0. The χ^2/dof of the central line in Figure 8.5 is 0.7. This shows that the data are not inconsistent with the $[1 + x^2 + 8/3A^{\rm obs}x]$ description.

It is necessary to know the fraction of each source of prompt electron candidate in the sample to obtain the b asymmetry from $A^{\rm obs}$. In Section 6.2 the fraction of hadrons misidentified as electrons was calculated to be $(3.78 \pm 0.21)\%$ for the barrel selection and $(2.62 \pm 0.26)\%$ for the endcap selection. There were 4697 prompt electron candidates tagged at $|\cos\theta| < 0.7$ and 470 tagged at $0.815 < |\cos\theta| < 0.91$, resulting in a track weighted $F_{\rm (misID)}$ of $(3.7 \pm 0.2)\%$. The errors in the misidentification rates were taken as correlated in deriving the error in $F_{\rm (misID)}$.

581 tracks that would have otherwise been accepted as prompt electron candidates were identified as originating from photon conversions. Using the $(84 \pm 4)\%$ conversion tagging efficiency from Section 5.5 and the $(65 \pm 10)\%$ estimated purity of the conversion electron sample, (72.8 ± 21.4) prompt electron candidates were estimated to be electrons originating from photon conversions. Another 0.5% of the prompt electron sample was estimated to be electrons originating from Dalitz decays. Thus

$$F_{\rm (conv)} = 0.019 \pm 0.005. \tag{8.12}$$

The fraction of the sample that is prompt electrons is then

$$F_{\rm prompt} = 1 - F_{\rm (misID)} - F_{\rm (conv)} = 0.944 \pm 0.005({\rm conv}) \pm 0.002({\rm misID}). \tag{8.13}$$

The F_i are given by

$$\frac{F_{(b\to c\to e^+)}}{F_{(b\to e^-)}} = \frac{\epsilon_{(b\to c\to e^+)}}{\epsilon_{(b\to e^-)}} \cdot \frac{B(b\to c\to e^+)}{B(b\to e^-)} \tag{8.14}$$

$$\frac{F_{(b\to c\to e^-)}}{F_{(b\to e^-)}} = \frac{\epsilon_{(b\to c\to e^-)}}{\epsilon_{(b\to e^-)}} \cdot \frac{B(b\to c\to e^-)}{B(b\to e^-)} \tag{8.15}$$

$$\frac{F_{(b\to \tau\to e^-)}}{F_{(b\to e^-)}} = \frac{\epsilon_{(b\to \tau\to e^-)}}{\epsilon_{(b\to e^-)}} \cdot \frac{B(b\to \tau\to e^-)}{B(b\to e^-)} \tag{8.16}$$

$$\frac{F_{(c\to e^+)}}{F_{(b\to e^-)}} = \frac{\Gamma_{Z^0\to c\bar{c}}}{\Gamma_{\rm had}} \cdot \left(\frac{\Gamma_{Z^0\to b\bar{b}}}{\Gamma_{\rm had}}\right)^{-1} \frac{\epsilon_{(c\to e^+)}}{\epsilon_{(b\to e^-)}} \cdot \frac{B(c\to e^+)}{B(b\to e^-)}. \tag{8.17}$$

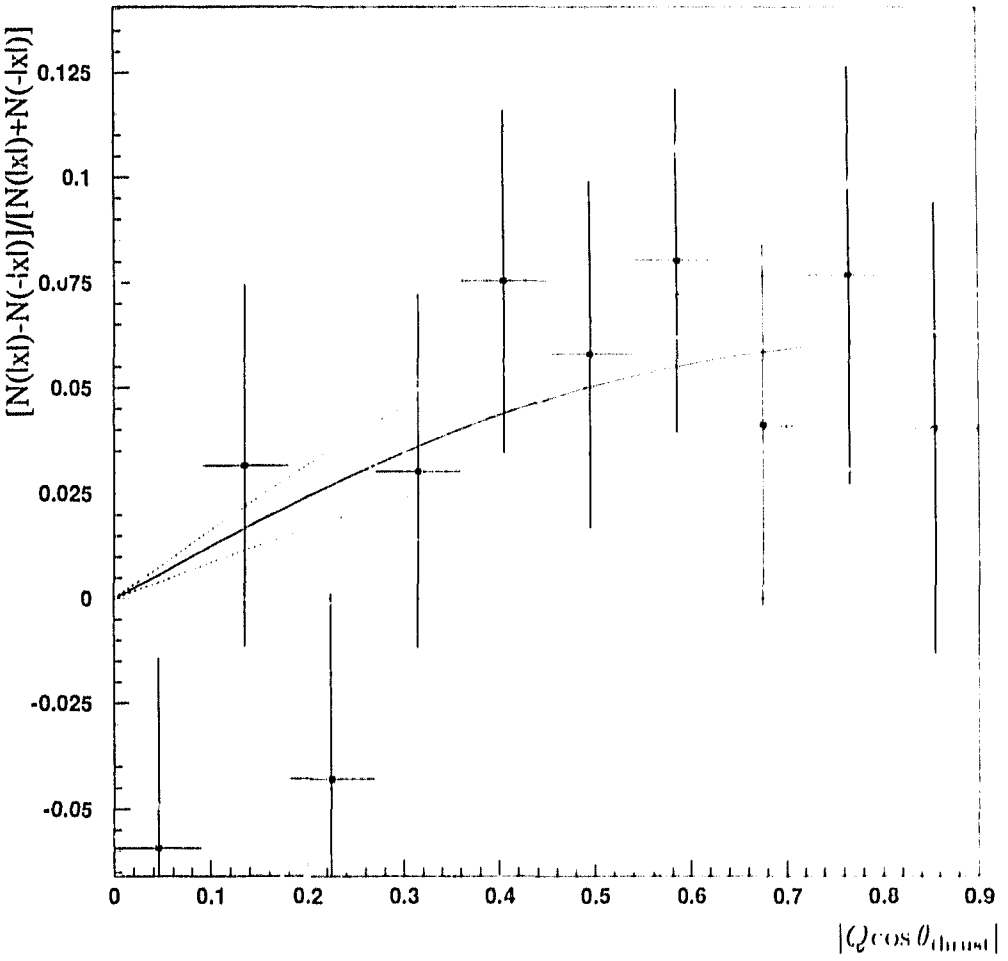

Figure 8.5: *The observed number of events in a forward ($x = |x|$) bin minus the number of events in the corresponding backward ($x = -|x|$) bin divided by the sum ($x = -Q\cos\theta_{\rm thrust}$). The solid line corresponds to the asymmetry from the maximum likelihood fit and the small dashed lines to the 1σ statistical errors. The χ^2/dof of the solid line is 0.7. The large dashed line at 0 corresponds to zero asymmetry and has a χ^2/dof of 1.9.*

$F_{(b\to e^-)}$ is fixed by the constraint

$$F_{\text{prompt}} = F_{(b\to e^-)} + F_{(b\to c\to e^+)} + F_{(b\to c\to e^-)} + F_{(b\to\tau\to e^-)} + F_{(c\to e^+)}. \quad (8.18)$$

The kinematic and geometric efficiencies (ϵ_i) were calculated as in Section 6.3.

As used in the measurement of $\frac{\Gamma_{Z^0\to b\bar{b}}}{\Gamma_{had}}$, $B(b\to\tau\to e^-)$ is taken to be

$$B(b\to\tau\to e^-) = (0.044\pm 0.018)B(b\to e^-). \quad (8.19)$$

Following Equation 2.27,

$$B(b\to c\to e^+) = 0.87B(b\to c\to e) \quad (8.20)$$
$$B(b\to c\to e^-) = 0.13B(b\to c\to e). \quad (8.21)$$

In calculating $F_{(c\to e^+)}/F_{(b\to e^-)}$, $\frac{\Gamma_{Z^0\to c\bar{c}}}{\Gamma_{had}}$ was taken to be the Standard Model value of 0.171 [17]. $\frac{\Gamma_{Z^0\to b\bar{b}}}{\Gamma_{had}}$ was taken to be the OPAL measured value of 0.226 ± 0.020 [22]. This value is used as opposed to the value determined in Chapter 7 since it is more precise. This value of $\frac{\Gamma_{Z^0\to c\bar{c}}}{\Gamma_{had}}$ contains the assumption that the semileptonic branching ratios of Λ_b and B_s are the same as the light B mesons.

Table 8.2 shows the prompt fractions normalised to $F_{(b\to e^-)}$. The sources of error in these fractions are often correlated and therefore each error source will be considered separately.

Prompt source	$F_i/F_{(b\to e^-)}$
$b\to c\to e^+$	0.12
$b\to c\to e^-$	0.013
$b\to\tau\to e^-$	0.014
$c\to e^+$	0.080

Table 8.2: *The ratio $F_i/F_{(b\to e^-)}$ for each prompt source. These fractions were determined in the context of the ACM model [31]. There are many sources of uncertainty in these numbers (branching ratios, modelling, fragmentation, etc.), many of which are correlated between the sources and are assessed in Section 8.2.*

The Standard Model value of [17]

$$A_{FB}^c = 0.0542, \quad (8.22)$$

was used in calculating A_{FB}^b. This value corresponds to a centre of mass energy of 91.2 GeV, a top quark mass of 132 GeV/c^2 and 300 GeV/c^2 for the mass of the Higgs boson.

Using Equation 8.6 then gives the b quark forward-backward asymmetry as

$$A_{FB}^{b} = \frac{0.0473 + 0.062 \cdot 0.0542}{0.769 - 0.092 + 0.010 + 0.011} = 0.0724 \pm 0.0210. \qquad (8.23)$$

The error is the statistical error from the fit to A^{obs}. It should be noted that this value of the asymmetry contains no correction for $B^0\bar{B}^0$ mixing.

8.2 Systematic Errors

The sensitivity of the above A_{FB}^{b} value to various systematic effects will now be discussed. Each independent source of error is considered separately and the error will be added in quadrature to obtain the final systematic error.

The parent distribution of electrons from photon conversions has been assumed to be described by a $(1 + x^2)$ distribution, while Figure 8.2 shows that the observed distribution varies as $(1 + 1.7x^2)$. This variation was determined from a sample of tagged conversion electrons with none of the prompt electron selection criteria applied, except the momentum and transverse momentum requirements. Since the tagging efficiency for conversion electrons is independent of $|\cos\theta|$ in the angular range considered [54], this distribution reflects the parent distribution. This parent angular distribution for the conversion electrons can be incorporated in Equation 8.2, thus modifying Equation 8.4 to

$$G(x) = C''\epsilon(x)[\alpha + \beta x^2 + \frac{8}{3}A^{obs}x]. \qquad (8.24)$$

A_{FB}^{b} is still related to A^{obs} through Equation 8.6. α and β are 0.997 and 1.009 respectively for $F_{(conv)} = 0.019$ and a $(1 + 1.7x^2)$ distribution.

In obtaining Equation 8.24 it has been assumed that the acceptance $(\epsilon_{(conv)}(x))$ is a constant in x. Since $F_{(conv)}$ is fixed we must then have a normalisation factor k such that

$$\int_{-1}^{1}(1 + x^2)dx = k\int_{-1}^{1}(1 + 1.7x^2)dx. \qquad (8.25)$$

The normalisation factor k is to keep the constant C'' in Equation 8.4 the same as that in Equation 8.24. From Figure 8.1 it is seen that approximating the acceptance as a constant overestimates the effect the $(1 + 1.7x^2)$ distribution will have on the result.

Using the right hand side of Equation 8.24 as the likelihood to obtain A^{obs} resulted in a negligible difference from that obtained using Equation 8.4.

The uncertainty of (± 0.005) in $F_{(conv)}$ induces an uncertainty of (± 0.0004) in A_{FB}^{b} which is assigned to the systematic error.

In contrast to electrons from photon conversions, the angular distribution of hadrons misidentified as electrons cannot be separated from the detector acceptance. The sensitivity of the measured A_{FB}^{b} to the variation of $F_{(\mathrm{misID})}$ with $|x|$, given in Table 6.20, was assessed by performing the likelihood fit in the three bins of $|x|$ used in that table. Within these three bins the ratio $\epsilon_{(\mathrm{misID})}(x)/\epsilon_{(b\to e^-)}(x)$ was taken to be constant. Table 8.3 shows the fitted A^{obs} for each of the three $|x|$ ranges. The weighted average of these values reproduces the 0.0473 from the fit to the entire distribution when $F_{(\mathrm{misID})}$ is taken to be 0.037 for all $|x|$. Table 8.4 shows the resulting values of A_{FB}^{b} in each of the three $|x|$ bins when A_{FB}^{b} was calculated using the values of $F_{(\mathrm{misID})}$ given in Table 6.20 for that range of $|x|$. The weighted average of these three A_{FB}^{b} values is 0.0003 lower than the value obtained assuming that $\epsilon_{(\mathrm{misID})}(x)/\epsilon_{(b\to e^-)}(x)$ was constant. Thus 0.0003 is assigned to the systematic error on A_{FB}^{b} due to the variation of the acceptance for hadrons misidentified as electrons.

$\lvert\cos\theta_{\mathrm{thrust}}\rvert$	fitted asymmetry
0–0.25	(-0.055 ± 0.071)
0.25–0.7	(0.055 ± 0.018)
0.7–0.9	(0.045 ± 0.026)

Table 8.3: *The asymmetry obtained by performing the likelihood fit in three bins of* $|\cos\theta_{\mathrm{thrust}}|$.

$\lvert\cos\theta_{\mathrm{thrust}}\rvert$	A_{FB}^{b}
0–0.25	(-0.075 ± 0.103)
0.25–0.7	(0.083 ± 0.026)
0.7–0.9	(0.069 ± 0.037)

Table 8.4: A_{FB}^{b} *obtained from the observed asymmetry in three bins of* $|\cos\theta_{\mathrm{thrust}}|$, *when* $F_{(\mathrm{misID})}$ *is taken from Table 6.20.*

Besides the variation of $F_{(\mathrm{misID})}$ with $|x|$, the average value of $F_{(\mathrm{misID})}$ is uncertain. In Section 6.2 the fraction of the prompt electron sample estimated to be hadrons was determined to be $(3.8 \pm 0.2)\%$ for the barrel selection and $(2.6 \pm 0.3)\%$ for the endcap selection. Of the 5167 candidate prompt electrons, 4697 were tagged with the barrel selection and 470 with the endcap selection. Weighting the two misidentification errors by the number of candidates selected

gives an uncertainty of ± 0.002 in $F_{(\mathrm{misID})}$. In obtaining this uncertainty the uncertainties in the barrel and endcap selections were taken to be 100% correlated. This uncertainty in $F_{(\mathrm{misID})}$ induces an uncertainty of 0.0001 in A_{FB}^{b}, which is assigned to the systematic error.

The kinematic and geometric efficiencies for the various sources of prompt electrons vary with the average fraction of the beam energy carried by the hadron containing the primary quark (first rank hadron). For $b\bar{b}$ events, this average was chosen to be $\langle x \rangle_b = 0.72$ (Section 6.3). The value of the average fractional energy carried by the first rank b-flavoured hadron was varied between 0.68 and 0.76 and the kinematic and geometric efficiencies for $b \to e^-$, $b \to c \to e^+$, $b \to c \to e^-$ and $b \to \tau \to e^-$ were recalculated. Changing the b quark fragmentation in this range resulted in a change of 0.0012 in A_{FB}^{b} which is assigned to the systematic error.

Similarly, the average energy of the first rank charmed hadron ($\langle x \rangle_c$) was varied between 0.48 and 0.59 from the central value of 0.53. The kinematic and geometric efficiency for the process $c \to e^+$ was recalculated at these values and a variation of 0.0024 in A_{FB}^{b} was observed. Thus 0.0024 is added to the systematic error on A_{FB}^{b} to account for the uncertainty in c quark fragmentation.

The statistical error on the kinematic and geometric efficiencies, due to the limited Monte Carlo statistics, make the F_i uncertain. The ϵ_i were varied to the extremes of the 1σ statistical errors in such a manner to induce the largest possible change in A_{FB}^{b} (e.g. lower $\epsilon_{(b\to e^-)}$, $\epsilon_{(b\to c\to e^+)}$ and $\epsilon_{(b\to\tau\to e^-)}$ and raise $\epsilon_{(b\to c\to e^+)}$, etc.). A maximum change of 0.0013 in A_{FB}^{b} could be induced in this manner and is added to the systematic error.

The fractions $F_{(b\to e^-)}$, $F_{(b\to c\to e^+)}$ and $F_{(b\to c\to e^-)}$ are uncertain due to the measurement errors in the branching ratios obtained at the $\Upsilon(4S)$. As for the measurement of $\Gamma_{Z^0\to b\bar{b}}/\Gamma_{had}$, the branching ratio errors are considered in two parts, intrinsic and modelling. The intrinsic error of ± 0.0045 in $B(b \to e^-)$ contributes an error of 0.0010 to A_{FB}^{b}. The intrinsic error of ± 0.0010 in $B(b \to c \to e)$ contributes and error of ± 0.0016 to A_{FB}^{b}. It should be noted that these errors are assessed in the context of the ACM model [31].

The uncertainty in the F_i due to the electron momentum modelling must be assessed using the branching ratios obtained by the CLEO collaboration in the context of a particular decay model. The procedure used to establish the uncertainty in A_{FB}^{b} due to the electron momentum modelling was identical with that used for the measurement of $\Gamma_{Z^0\to b\bar{b}}/\Gamma_{had}$. Unlike the case of $\Gamma_{Z^0\to b\bar{b}}/\Gamma_{had}$, the constraint on the sum $(F_{(b\to e^-)} + F_{(b\to c\to e^+)})$ from the total observed rate at the $\Upsilon(4S)$ does not help to lessen the sensitivity to the decay modelling. A_{FB}^{b} is obtained from A^{obs} using Equation 8.6, which has as a denominator

$$F_{(b\to e^-)} - F_{(b\to c\to e^+)} + F_{(b\to c\to e^-)} + F_{(b\to\tau\to e^-)}. \qquad (8.26)$$

The fact that the CLEO branching ratio measurements coupled with the model dependence constrain the sum ($F_{(b\to e^-)} + F_{(b\to c\to e^+)}$) to be almost constant, does not preclude large variations in the difference. When the ISGW model was used to obtain A_{FB}^b from A^{obs} the result was 0.0763, while 0.0705 was obtained when the ISGW** model was used. The largest difference of these two with the central value of 0.0724 using the ACM model is 0.0039, which is added to the systematic error to account for the semileptonic decay modelling.

As for $\Gamma_{Z^0\to b\bar{b}}/\Gamma_{had}$, the possibility of $b \to u e^- \bar{\nu}_e$ transitions change $\epsilon_{(b\to e^-)}$. Taking these corrections into account, as described for $\Gamma_{Z^0\to b\bar{b}}/\Gamma_{had}$ (Section 7.3), changed A_{FB}^b by 0.0003 and this amount is assigned to the systematic error.

Radiative corrections in b semileptonic decay also modify $\epsilon_{(b\to e^-)}$. Accounting for these, as was done for $\Gamma_{Z^0\to b\bar{b}}/\Gamma_{had}$, contributes 0.0003 to the systematic error in A_{FB}^b.

The uncertainty in the correction to $B(b \to c \to e^+)$ to account for the different mix of b-flavoured hadrons at LEP (0.926 ± 0.073) induces an uncertainty of 0.0013 in A_{FB}^b which is assigned to the systematic error.

In calculating $F_{(b\to c\to e^+)}$ and $F_{(b\to c\to e^-)}$ it was assumed that b quark decays to a c quark and a virtual W^- 100% of the time. The resulting virtual W^- was estimated to produce an anti-c quark 15% of the time (Equation 2.27). Since this value relies on phase space calculations involving quark masses, it is uncertain. The branching ratio for the virtual W^- to c was varied from 10% to 20%. A change of 0.0008 in A_{FB}^b was observed and is added to the systematic error.

As in Section 7 $B(b \to \tau \to e^-)$ was taken to be $(0.044 \pm 0.018) B(b \to e^-)$. The uncertainty in this branching ratio contributes 0.0001 to the systematic error in A_{FB}^b.

$F_{(c\to e^+)}$ was determined from Equation 8.17. Three quantities contribute to the uncertainty in $F_{(c\to e^+)}$; $\frac{\Gamma_{Z^0\to c\bar{c}}}{\Gamma_{had}} \cdot \left(\frac{\Gamma_{Z^0\to b\bar{b}}}{\Gamma_{had}}\right)^{-1}$, $\frac{B(c\to e^+)}{B(b\to e^-)}$ and $\frac{\epsilon_{(c\to e^+)}}{\epsilon_{(b\to e^-)}}$. The systematic errors arising from $B(b \to e^-)$ and the kinematic and geometric efficiencies have been discussed above. $B(c \to e^+)$ was taken to be $(7.9 \pm 1.1)\%$ [28]. The error on this branching ratio contributes 0.0013 to the systematic error on A_{FB}^b.

In the Standard Model, $\frac{\Gamma_{Z^0\to c\bar{c}}}{\Gamma_{Z^0\to b\bar{b}}}$ varies slightly with m_t and m_{Higgs}. The Standard Model value of $\frac{\Gamma_{Z^0\to c\bar{c}}}{\Gamma_{had}} = 0.171$ and the OPAL measured value $\frac{\Gamma_{Z^0\to b\bar{b}}}{\Gamma_{had}} = (0.226 \pm 0.020)$ [22] were taken to determine the ratio $\frac{\Gamma_{Z^0\to c\bar{c}}}{\Gamma_{Z^0\to b\bar{b}}}$. Since the error in $\frac{\Gamma_{Z^0\to b\bar{b}}}{\Gamma_{had}}$ induces a larger error in the ratio than any allowed top mass variation would in the Standard Model ($\frac{\Gamma_{Z^0\to c\bar{c}}}{\Gamma_{Z^0\to b\bar{b}}}$ varies by 0.1% when m_t is varied between 82 GeV/c^2 and 177 GeV/c^2), it was used to assess the systematic error on A_{FB}^b arising from $\frac{\Gamma_{Z^0\to c\bar{c}}}{\Gamma_{Z^0\to b\bar{b}}}$. The error in $\Gamma_{Z^0\to b\bar{b}}/\Gamma_{had}$ induces an uncertainty of 0.0009 in A_{FB}^b, which is added to the systematic error.

A_{FB}^c was taken to be the Standard Model value of 0.0542 [17]. Two mea-

surements of this quantity have been reported at LEP $A_{FB}^{c} = (0.064 \pm 0.039 \pm 0.030)$ [19] and $A_{FB}^{c} = (0.064 \pm 0.049 \pm 0.024)$ [66]. These measurements are consistent with the Standard Model prediction, although within the errors they do not exclude a zero asymmetry either. Since the aim of this measurement of A_{FB}^{b} is to test the Standard Model, the Standard Model prediction for A_{FB}^{c} and its uncertainty is used. If m_t is varied between 82 and 177 GeV/c^2, which corresponds to the 1σ errors obtained by combining the Z^0 lineshape results of the four LEP experiments [25], the Standard Model prediction for A_{FB}^{c} varies between 0.0494 and 0.0602 [17]. This variation in A_{FB}^{c} induces a change of 0.0005 in A_{FB}^{b}, which is added to the systematic error on A_{FB}^{b}. Equation 8.23 can be used to assess the effect a larger variation of A_{FB}^{c} would have on A_{FB}^{b}.

A mismeasurement of the sign of the charge of the prompt electron candidate would change the sign of $-Q\cos\theta_{\rm thrust}$ and therefore affect the asymmetry measurement. Radiative muon pair events ($e^+e^- \rightarrow \mu^+\mu^-\gamma$) were studied to determine how often the incorrect sign was attributed to a track. For events in which one muon had a momentum of less than 30 GeV/c, the sum of the charges of the two muons in the event was taken. 0.2% of events selected in this manner had a total charge that was not zero. Since it is more likely that the higher momentum muon track had a mismeasured charge, due to the smaller sagitta, 0.2% could be considered an upper limit on the charge confusion rate. In the dense track environment of a multihadronic event, the charge of a track may be confused due to effects not present in muon pair events. A study of simulated multihadronic events suggested that 0.1% of all tracks with momentum greater than 2 GeV/c and $p_T > 0.8$ GeV/c are charged confused. This agrees with the expectation that the 0.2% might be an overestimate. Since the 0.2% is determined from the data, it was used to assess the systematic error due to charge confusion.

The effect of a charge confusion rate of 0.2% per track on the observed asymmetry was assessed by randomly changing the sign of the charge of 0.2% of the prompt electron candidates and fitting the resulting $-Q\cos\theta_{\rm thrust}$ distribution to obtain $A^{\rm obs}$. After many trials a gaussian distribution of $A^{\rm obs}$ values, centred at zero with a sigma of 0.0013, was obtained. This corresponds to a sigma of 0.0019 in A_{FB}^{b}, which is added to the systematic error to account for charge confusion.

The resolution in $\cos\theta_{\rm thrust}$ also contributes to the error on A_{FB}^{b}. The effect of the resolution on the thrust direction was assessed using simulated events. The quark directions in simulated events were smeared by a gaussian resolution of 0.05 rad. This resolution was observed to contribute an error of 0.0012 in A_{FB}^{b} and is added to the systematic error.

In obtaining the F_i, for the prompt sources, it was assumed that the absolute electron selection efficiency for each source was the same. Because of different isolation properties of electrons from direct b, cascade and direct charm decays, one might expect the efficiencies to differ. Differences in surrounding activity

would lead to different efficiencies for an isolation requirement ($E_{\rm cone}/E_{\rm cone2}$, 0-match). At present the only way to assess such an effect is with simulated data. For the barrel selection the Monte Carlo predicts that

$$\frac{\mathrm{EID}_{\mathrm{b}\to\mathrm{c}\to\mathrm{e}}}{\mathrm{EID}_{\mathrm{b}\to\mathrm{e}^-}} = 0.8 \pm 0.1$$

$$\frac{\mathrm{EID}_{\mathrm{b}\to\tau\to\mathrm{e}^-}}{\mathrm{EID}_{\mathrm{b}\to\mathrm{e}^-}} = 1.0 \pm 0.1$$

$$\frac{\mathrm{EID}_{\mathrm{c}\to\mathrm{e}^+}}{\mathrm{EID}_{\mathrm{b}\to\mathrm{e}^-}} = 0.7 \pm 0.1.$$

Where $\mathrm{EID_i}$ is the efficiency for an electron, with $p > 2$ GeV/c and $p_T > 0.8$ GeV/c, from source i to be identified as a prompt electron. For the endcap selection the corresponding predictions are:

$$\frac{\mathrm{EID}_{\mathrm{b}\to\mathrm{c}\to\mathrm{e}}}{\mathrm{EID}_{\mathrm{b}\to\mathrm{e}^-}} = 0.7 \pm 0.1$$

$$\frac{\mathrm{EID}_{\mathrm{b}\to\tau\to\mathrm{e}^-}}{\mathrm{EID}_{\mathrm{b}\to\mathrm{e}^-}} = 0.9 \pm 0.1$$

$$\frac{\mathrm{EID}_{\mathrm{c}\to\mathrm{e}^+}}{\mathrm{EID}_{\mathrm{b}\to\mathrm{e}^-}} = 0.5 \pm 0.1.$$

The errors in the ratios are due to the limited Monte Carlo statistics.

The requirement which leads to the largest difference in efficiency between the prompt sources is predicted to be that of $E_{\rm cone}/E_{\rm cone2}$ for the barrel selection. For the endcap selection, the differences are predicted to arise mostly in the 0-match and E/p requirements. Nearby particles are predicted to be the cause of the differences in efficiency for selecting prompt electrons from different sources, for both the barrel and endcap selections. For the Monte Carlo to be trusted to predict the source dependence of the prompt electron selection correctly, the simulation of energy deposition in the electromagnetic calorimeter and the particle flow near prompt leptons must be correct.

The efficiency for prompt electrons to satisfy the $E_{\rm cone}/E_{\rm cone2}$ requirement ($\mathrm{eff}_{E_{\rm cone}/E_{\rm cone2}}$) may be written as

$$\mathrm{eff}_{E_{\rm cone}/E_{\rm cone2}} = \mathrm{eff}_{SS} \cdot (1 - \mathrm{Ieff}_{OV}), \tag{8.27}$$

where eff_{SS} is the efficiency that arises from the electromagnetic shower spread and Ieff_{OV} is the inefficiency induced by overlapping activity[1]. Since eff_{SS} will

[1]The same arguments hold for the efficiency for a prompt electron to satisfy the 0-match or E/p requirements. $E_{\rm cone}/E_{\rm cone2}$ is used as an illustrative example.

be the same for all electrons with the same incident momentum, only differences in Ieff_{OV} between sources can change $\mathrm{eff}_{E_{\mathrm{cone}}/E_{\mathrm{cone2}}}$ and affect the ratio $\frac{\mathrm{EID}_i}{\mathrm{EID}_{b\to e^-}}$.

Energy that is deposited in E_{cone2} (or the outer ring of "next-to-touching" blocks) by a nearby pion will contribute to Ieff_{OV}. In the simulated data, the energy deposited by a pion as it traverses the electromagnetic calorimeter is overestimated. Figure 8.6 shows a comparison of the raw cluster energy associated to a track with momentum between 2 and 5 GeV/c and dE/dx less than 9 keV/cm in the data and Monte Carlo. The clusters were required to have only one track associated to them. Too much energy is predicted to be deposited by low energy pions in the Monte Carlo. Since it is expected that there are more hadrons close to prompt electrons from sources other than direct b decay, this will lead to an overestimate of the effect of this overlapping activity on Ieff_{OV}.

Figure 8.7 [67] compares the data and the JETSET Monte Carlo prediction for the particle flow in three jet events, where one jet had an identified prompt lepton (muon or electron) [2]. There is an indication that JETSET does not model the particle flow correctly for jets with a prompt lepton.

Thus, it is not clear that the Monte Carlo prediction for the differences in the electron identification efficiencies for the different sources of prompt electrons is valid. Nonetheless, some differences in efficiency might be expected. Since the predicted energy deposit for pions is too large, it leads to an overestimate of the differences, and the particle flow is not modelled too poorly, the Monte Carlo may be thought of as providing an upper bound on the possible effect. If the F_i are calculated using the Monte Carlo predictions for $\frac{\mathrm{EID}_i}{\mathrm{EID}_{b\to e^-}}$, the calculated value of A_{FB}^b changes by 0.0052. The entire amount of this change is added to the systematic error on A_{FB}^b to account for any possible source bias in the efficiency.

Two photon events ($e^+e^- \to e^+e^-X$) with hadrons in the final state are potentially a serious source of bias in the asymmetry measurement. In these events the e^- is almost always scattered forward, and therefore a hadronic two photon event, in which the initial state electron was scattered into the acceptance, could bias the asymmetry measurement. 20 pb^{-1} of Monte Carlo two photon events, produced with the Vermaseren generator [69], were studied and only one event satisfied the event selection criteria and had an electron in the geometric acceptance of the electron selection. The electron in this event did not satisfy the $p_T > 0.8$ GeV/c requirement. Thus for the approximately 11 pb^{-1} of data used in the determination of A_{FB}^b, this is not a serious source of background

Table 8.5 shows the various contributions to the systematic error on A_{FB}^b. Before correcting for $B^0\bar{B}^0$ mixing

$$A_{FB}^b = 0.072 \pm 0.021 \pm 0.008. \tag{8.28}$$

[2] Version 7.2 of the JETSET Monte Carlo [32] was used for this comparison, however the results are expected to hold for version 7.3 as well.

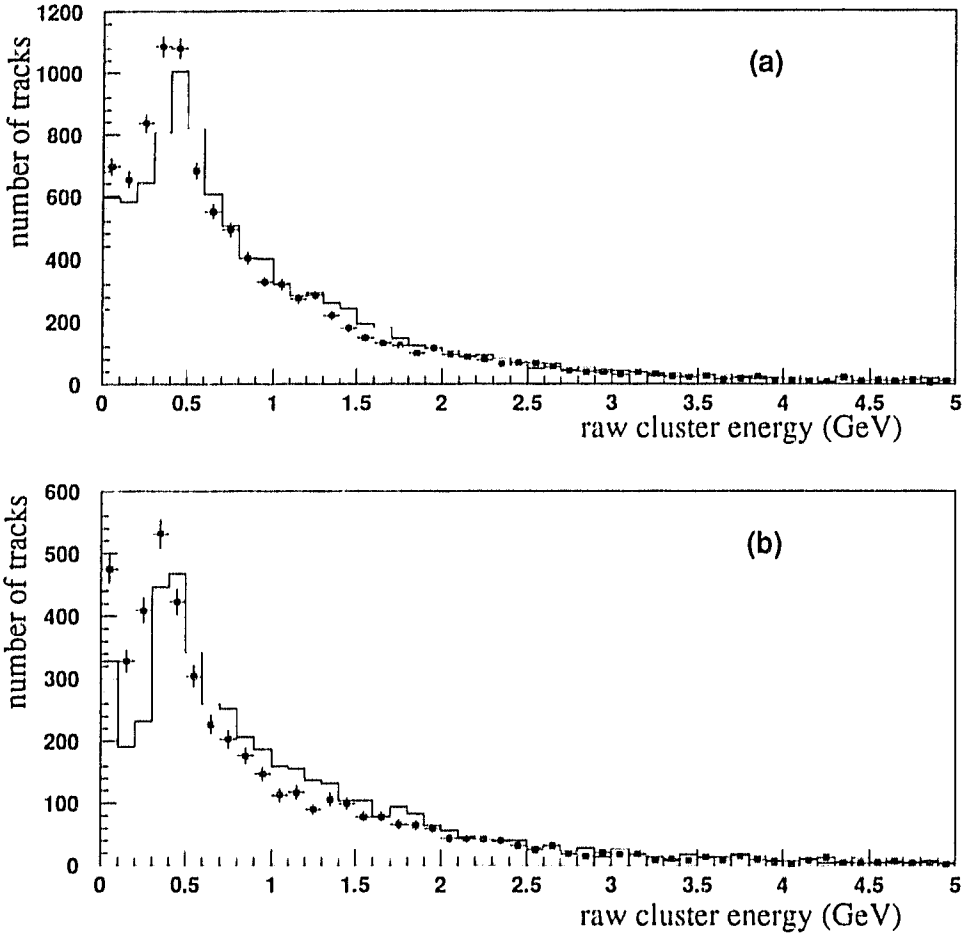

Figure 8.6: *The raw cluster energy for isolated particles in multihadronic events. The points are from the data and the histogram is the Monte Carlo prediction. The particles were selected to have a dE/dx value less than 9 keV/cm, momentum between 2 and 5 GeV/c and the cluster was required to be matched to only one track. (a) is for* $|\cos\theta| < 0.7$ *and (b) is for* $0.815 < |\cos\theta| < 0.91$. *The Monte Carlo histograms are normalised to the same number of tracks. The Monte Carlo predicts too much energy to be deposited in the electromagnetic calorimeter for low energy hadrons.*

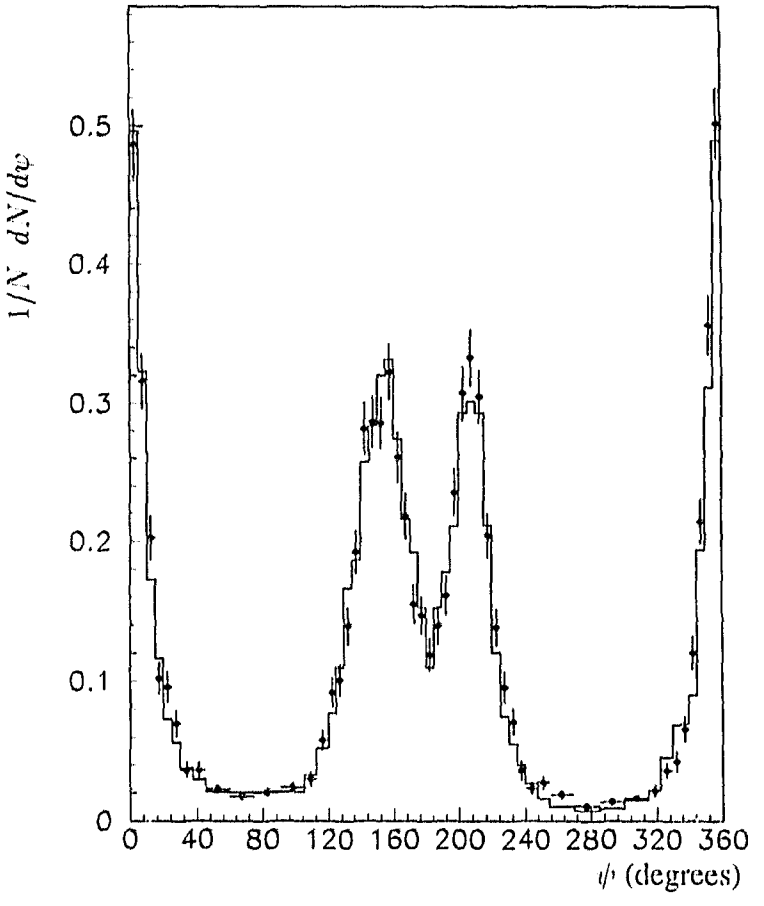

Figure 8.7: *The particle flow in three jet events [67]. The data (points) are from [68], the Monte Carlo (histogram) is JETSET 7.2 [32]. The angle ψ is measured from the core of the highest energy jet in the event. The jet at 210° was required to contain a prompt lepton candidate. There is an indication that JETSET does not reproduce the particle flow in jets with a prompt lepton.*

Error Source	Contribution
Photon conversion fraction	0.0004
Misidentification acceptance variation	0.0003
Misidentification fraction	0.0001
b fragmentation	0.0012
c fragmentation	0.0024
Monte Carlo statistics	0.0013
$B(\mathrm{b} \to \mathrm{e}^-)$	0.0010
$B(\mathrm{b} \to \mathrm{c} \to \mathrm{e})$	0.0016
b decay modelling	0.0039
$\mathrm{b} \to \mathrm{u}\mathrm{e}^-\overline{\nu_e}$	0.0003
Radiative corrections	0.0003
$B(\mathrm{b} \to \mathrm{c} \to \mathrm{e}^+)$ correction	0.0013
$\mathrm{b} \to \mathrm{c}\mathrm{c}X/\mathrm{b} \to \mathrm{c}X$	0.0008
$B(\mathrm{b} \to \tau \to \mathrm{e}^-)$	0.0001
$\Gamma_{\mathrm{Z}^0 \to \mathrm{b}\overline{\mathrm{b}}}/\Gamma_{\mathrm{had}}$	0.0009
$B(\mathrm{c} \to \mathrm{e}^+)$	0.0013
$\mathrm{A}_{\mathrm{FB}}^{\mathrm{c}}$	0.0005
Charge confusion	0.0019
Thrust axis resolution	0.0012
Electron identification flavour dependence	0.0052
total	0.0081

Table 8.5: *The contributions to the systematic error on* $A_{\mathrm{FB}}^{\mathrm{b}}$ *before correcting for* $\mathrm{B}^0\overline{\mathrm{B}}^0$ *mixing.*

The first error is statistical and the second systematic.

8.3 $\mathrm{B}^0\overline{\mathrm{B}}^0$ mixing correction

B^0 mesons ($\mathrm{B}^0_{\mathrm{d}}$ and $\mathrm{B}^0_{\mathrm{s}}$) may transform to $\overline{\mathrm{B}}^0$ mesons through processes similar to that shown in Figure 8.8. The presence of these transitions can cause b quarks to decay as $\overline{\mathrm{b}}$ quarks and potentially produce a lepton of the opposite sign. This affects the asymmetry measurement by creating a misassignment of forward and backward events.

The parameter χ is used to characterise $\mathrm{B}^0\overline{\mathrm{B}}^0$ mixing. χ is the probability that a produced b quark will decay as a $\overline{\mathrm{b}}$ quark. An average of χ measurements from

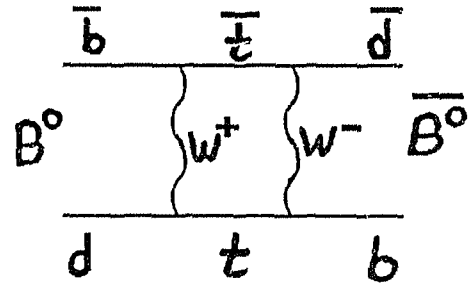

Figure 8.8: *A process that gives* $B^0\overline{B}^0$ *mixing. The virtual t quark may also be an u or c quark.*

prompt leptons at LEP is [70]

$$\chi = 0.144 \pm 0.020. \tag{8.29}$$

Since the amount of mixing in the B^0_s system is potentially much different from the B^0_d system[3], it is important that this χ is for the (unknown) mix of B^0_d and B^0_s produced at LEP.

The forward-backward asymmetry is

$$A^b_{FB} = \frac{N_F - N_B}{N_F + N_B}, \tag{8.30}$$

with N_F (N_B) the number of b quarks produced in the forward (backward) direction. In the presence of $B^0\overline{B}^0$ mixing, a fraction χ of the forward (backward) produced b quarks will decay as $\overline{b}$ quarks and appear to be backward (forward) produced. This modifies N_F and N_B to

$$N_F^{obs} = N_F(1-\chi) + N_B\chi \tag{8.31}$$

$$N_B^{obs} = N_B(1-\chi) + N_F\chi, \tag{8.32}$$

where N_F^{obs} and N_B^{obs} are the observed number of forward and backward quark decays. Thus the true A^b_{FB} is related to the observed A^b_{FB} ($(A^b_{FB})_{obs}$) by

$$A^b_{FB} = \frac{1}{1-2\chi}(A^b_{FB})_{obs}. \tag{8.33}$$

[3] χ has been measured at the $\Upsilon(4S)$ to be 0.16 ± 0.04 [28] for B^0_d mesons only.

Only $(A_{FB}^{b})_{obs}$ is to be corrected and not the observed asymmetry (A^{obs}), since there is no observed mixing in the charm system [28].

Using the value of χ given in Equation 8.29 and the A_{FB}^{b} value given in Equation 8.28, A_{FB}^{b} corrected for $B^0\bar{B}^0$ mixing, is then

$$A_{FB}^{b} = 0.101 \pm 0.029 \pm 0.011 \pm 0.006. \quad (8.34)$$

The errors are statistical and systematic on the determination of the observed A_{FB}^{b} and in addition an error due to the error in χ. No error is assessed to account for the fluctuations in the actual number of b quarks that decayed as b quarks in the sample used.

This value of A_{FB}^{b} is in agreement with the Standard Model prediction of 0.085, for a top mass of 132 GeV/c^2 and a Higgs mass of 300 GeV/c^2 [17].

Chapter 9

Conclusion

Measurements of A_{FB}^{b}, the forward-backward asymmetry in $b\bar{b}$ production, at $\sqrt{s} \approx 91.2$ GeV and $\Gamma_{Z^0 \to b\bar{b}}$, the partial width of the Z^0 boson into b quarks have been reported. Figure 9.1 shows these two values along with the Standard Model [17] predicted allowed region. Within the measurement errors, there is agreement with the Standard Model prediction. The dominant error on A_{FB}^{b} is statistical, while the dominant error on $\Gamma_{Z^0 \to b\bar{b}}$ is systematic, arising mainly from the prompt electron selection efficiency.

$\Gamma_{Z^0 \to b\bar{b}}/\Gamma_{had}$ has been determined to be $(0.230 \pm 0.020 \pm 0.033)$, the errors are statistical and systematic. This measurement is consistent with the Standard Model prediction of $\Gamma_{Z^0 \to b\bar{b}} = 376$ MeV [17], when Γ_{had} is taken to be the LEP value of 1.740 ± 0.012 GeV [25]. This value is also consistent with previous measurements of $\Gamma_{Z^0 \to b\bar{b}}/\Gamma_{had}$:

$$\frac{\Gamma_{Z^0 \to b\bar{b}}}{\Gamma_{had}} = 0.226 \pm 0.008 \pm 0.018 \quad \text{OPAL [22]}$$

$$\frac{\Gamma_{Z^0 \to b\bar{b}}}{\Gamma_{had}} = 0.193 \pm 0.006 \pm 0.011 \pm 0.021 \quad \text{OPAL [18]}$$

$$\Gamma_{Z^0 \to b\bar{b}} = 385 \pm 7 \pm 11 \text{ MeV} \quad \text{L3 [23]}$$

$$\frac{\Gamma_{Z^0 \to b\bar{b}}}{\Gamma_{had}} = 0.215 \pm 0.017 \pm 0.024 \quad \text{ALEPH [24]}.$$

This measurement uses, as in [22], CLEO measurements of the prompt electron spectrum from B decays to reduce the sensitivity to b-flavoured hadron decay modelling. The CLEO semileptonic branching ratios are used in conjunction with the predicted momentum spectra to take advantage of the correlation between the direct b and cascade branching ratios and the kinematic efficiency. Therefore it has been assumed that the semileptonic branching ratios of the Λ_b and B^0_s are the same as the B^0_d and $B^{\pm}$ mesons. The measurement of the L3 collaboration of $B(b \to l) = 0.113 \pm 0.010 \pm 0.006$ [23], supports this assumption.

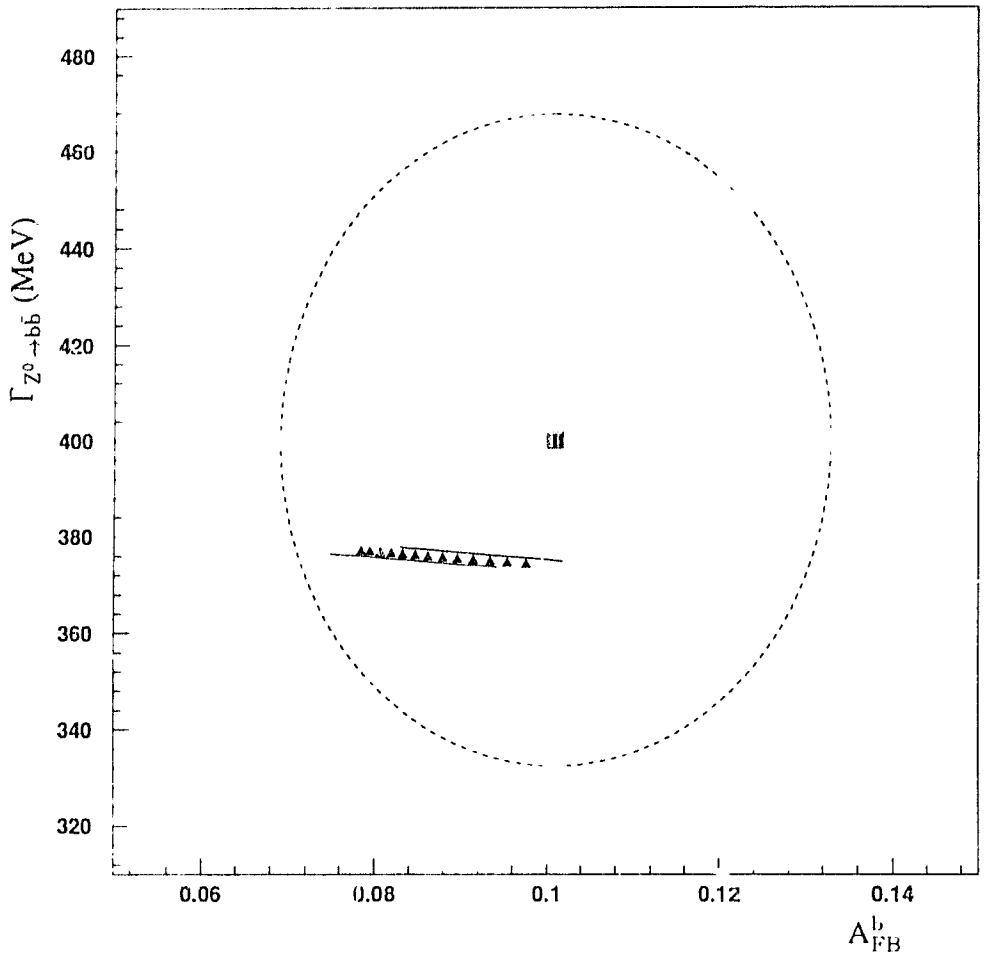

Figure 9.1: $\Gamma_{Z^0\to b\bar{b}}$ *vs.* A^b_{FB} *at* $\sqrt{s} = 91.2$ *GeV and* $m_{Z^0} = 91.175$ *GeV/c*^{2}. *The triangles correspond to the Standard Model prediction [17] with a Higgs mass of 300 GeV/c*^{2} *and various values of the top quark mass from 80 GeV/c*^{2} *to 200 GeV/c*^{2}. *The upper curve is for a Higgs mass of 60 GeV/c*^{2} *and the lower curve is for a Higgs mass of 1000 GeV/c*^{2}. *The square is this measurement of these two quantities and the dotted ellipse denotes the 60% confidence region of the two measurements combined.*

A_{FB}^{b} has been determined to be $A_{FB}^{b} = 0.101 \pm 0.029 \pm 0.011 \pm 0.006$. The errors are statistical, systematic and the error on $B^0\bar{B}^0$ mixing parameter χ. This is again consistent with the Standard Model prediction of 0.085 [17] and with the previous measurements given in Chapter 2.1. Since different experiments use different values of χ, it is less ambiguous to compare the values of A_{FB}^{b} obtained before correcting for $B^0\bar{B}^0$ mixing. Before correcting for $B^0\bar{B}^0$ mixing the measurements are:

A_{FB}^{b}	$= 0.072 \pm 0.021 \pm 0.008$	This measurement
A_{FB}^{b}	$= 0.072 \pm 0.042 \pm 0.010$	OPAL [18]
A_{FB}^{b}	$= 0.093 \pm 0.021 \pm 0.005$	ALEPH [19]
A_{FB}^{b}	$= 0.115 \pm 0.043 \pm 0.013$	DELHI [20]
A_{FB}^{b}	$= 0.084 \pm 0.025$	L3 [21].

This measurement of A_{FB}^{b} includes an assessment of the b hadron decay modelling uncertainties that are absent in the previous measurements [18, 19, 20, 21]. These uncertainties are significant in this measurement and cannot be ignored.

Bibliography

[1] P. Langacker, *Particle physics summary, Where are we and where are we going?*, Summary talk given at XXVIIth Rencontre de Moriond on Electroweak Interactions and Unified Theories, Les Arcs, France, March 1992, UPR-0512T (1992).

[2] F.J. Hasert, *et al.*, Phys. Letters **B46**, (1973) 138.

[3] G. Arnison *et al.*, Phys. Letters **122B**, (1983) 103

[4] *LEP Design Report*, CERN-LEP/84-01 (1984).

[5] T. Mori, private communication.

[6] D. Decamp *et al.*, Nucl. Inst. and Methods **A294** (1990) 121.

[7] P. Aarnio *et al.*, Nucl. Inst. and Methods **A303** (1991) 233.

[8] B. Adeva *et al.*, Nucl. Inst. and Methods **A289** (1990) 35.

[9] K. Ahmet *et al.*, Nucl. Instr. and Meth. **A305** (1991) 275.

[10] S.L. Glashow, J. Iliopoulos and L. Maiani, Phys. Rev. **D2** (1970) 1285.

[11] S. Weinberg, Phys. Rev. Lett. **19** (1967) 1264.

[12] A. Salam, *Elementary Particle Theory*, Ed. N. Svartholm, (Almquist and Wiksells, Stockholm, 1969) p. 367.

[13] E. Fermi, Nuovo Cimento **11** (1934) 1.

[14] R.P. Feynman, *Quantum Electrodynamics*, (Benjamin-Cummings, Reading, Mass., 1961.)

[15] Z Physics at LEP 1, ed. G. Altarelli et al, CERN 89-08 (1989).

[16] G. Alexander *et al.*, Z. Phys. **C52** (1991) 175.

[17] Using the line shape program ZFITTER. D. Bardin *et al.*, Berlin Zeuthen preprint PHE 89-19, 1989;
R. Kleiss *et al.*, in [15].

[18] M.Z. Akrawy *et al.*, Phys. Letters **B263** (1991) 311. This OPAL result uses inclusive muons only.

[19] D. Decamp *et al.*, *Measurement of the Forward-Backward Asymmetry in* $Z^0 \rightarrow b\bar{b}$ *and* $Z^0 \rightarrow c\bar{c}$, submitted to Phys. Letters B, CERN-PPE/91-71 (1991).

[20] P. Abreu *et al.*, *A Measurement of the* $b\bar{b}$ *Forward Backward Asymmetry Using the Semileptonic Decay into Muons*, submitted to Phys. Lett. B, CERN-PPE 91-213 (1991).

[21] B. Adeva *et al.*, Phys. Letters **B252** (1990) 713.

[22] P.D. Acton *et al.*, Z. Phys. **C55** (1992) 191. This OPAL result uses inclusive electrons only.

[23] B. Adeva *et al.*, Phys. Letters **B261** (1991) 177.

[24] D. Decamp *et al.*, Phys. Letters **B244** (1990) 551.

[25] The LEP Collaborations: ALEPH, DELPHI, L3 and OPAL, *Electroweak Parameters of the* Z^0 *Resonance and the Standard Model*, submitted to Physics Lett. B, CERN-PPE/91-232 (1991).

[26] P.D.Acton *et al.*, Phys. Letters **B274** (1992) 513.

[27] Vernon D. Barger and Roger J.N. Phillips, *Collider Physics*, (Addison-Wesley Publishing Company, Don Mills, Ontario, 1987).

[28] J.J. Hernández *et al.*, Phys. Letters **B239** (1990) 1.

[29] C. Quigg and J.L. Rosner, Phys. Rev. **D19** (1979) 1532.

[30] S. Henderson *et al.*, Phys. Rev. **D45** (1992) 2212.

[31] G. Altarelli *et al.*, Nucl. Phys. **B208** (1982) 365.

[32] T. Sjöstrand, Comp. Phys. Comm. **39** (1986) 347.

[33] N. Isgur, D. Scora, B. Grinstein and M.B. Wise, Phys. Rev. **D39** (1989) 799.

[34] C. Peterson *et al.*, Phys. Rev. **D27** (1983) 105.

[35] O. Biebel *et al.*, *Performance of the OPAL Jet Chamber*, submitted to Nucl. Instr. and Meth., CERN-PPE/92-55 (1992).

[36] P. Schenk and R. Shypit, *Electron Identification in the OPAL Endcap Region*, OPAL Technical Note, TN095.

[37] CEREN-25 lead glass, from Corning France, 44 Avenue de Valvins, Avon, Cedex 77210 France.

[38] C. Beard *et al.*, Nucl. Inst and Methods **A286** (1990) 117.

[39] M. Arignon *et al.*, Nucl. Instr. and Meth. **A313** (1992) 103.

[40] J. T .M Baines *et al.*, *The Data Acquisition System of the OPAL Detector at LEP*, submitted to Nucl. Instr. and Meth., CERN-ECP/92-8 (1992).

[41] D. G. Charlton *et al.*, *The Online Event Filter of the OPAL Experiment at LEP*, submitted to Nucl. Instr. and Meth., CERN-PPE/92-136 (1992).

[42] D. G. Charlton, *Muon Matching*, OPAL Technical Note, TN065.

[43] W. Bartel *et al.*, Z. Phys. **C33** (1986) 23;
S. Bethke *et al.*, Phys. Lett. **B213** (1988) 235.

[44] M. Z. Akrawy *et al.*, Z. Phys. **C49** (1991) 375.

[45] M. Hauschild *et al* , *Particle Identification with the OPAL Jet Chamber*, submitted to Nucl. Inst. and Methods, CERN PPE/91-130 (1991).

[46] E. Fermi, Phys. Rev. **57** (1940) 485.

[47] A. Crispin and G. Fowler, Rev. Mod. Phys. **42** (1970) 290.

[48] J. Va'vra *et al.*, Nucl. Instr. and Methods **203** (1982) 203.

[49] W.W.M. Allison and J H. Cobb, Ann. Rev. Nucl. Part. Sci. **30** (1980) 253.

[50] A.H Walenta, Physica Scripta **23** (1981) 354.

[51] C. Fabjan in *Experimental Techniques in High Energy Physics*, T. Ferbel, ed. (Addison-Wesley Publishing Company, Inc., Don Mills, 1985) p.257.

[52] G. Alexanger *et al.*, Physics Lett. **B264** (1991) 467.

[53] R.K. Bock *et al.*, Nucl. Instr. and Methods **186** (1981) 533.

[54] R. Van Kooten and S. Tarem, private communication.

[55] J. Allison *et al.*, *The Detector Simulation Program for the OPAL Experiment at LEP*, submitted to Nucl. Inst. and Methods, CERN-PPE/91-234 (1991).

[56] D. Atwood and W.J. Marciano, Phys. Rev. **D41** (1990) 1736.

[57] D. Buskulic *et al.*, *Observation of the Semileptonic Deacys of* B_s *and* Λ_b *Hadrons at LEP*, submitted to Phys. Letters B, CERN-PPE/92-074 (1992).

[58] P. Acton *et al.*, *Evidence for the Existence of the Strange b-flavour Meson* B^0_s *in* Z^0 *Decays*, submitted to Phys. Letters B, CERN-PPe/92-144.

[59] P. Abreu *et al.*, *Evidence for* B^0_s *Meson Production in* Z^0 *Decays*, submitted to Phys. Letters B, CERN-PPE/92-104 (1992).

[60] D.Decamp *et al.*, *Evidence for b Baryons in* Z^0 *Decays*, submitted to Phys. Letters B, CERN-PPE/91-229 (1991).

[61] P. Acton *et al.*, Phys. Letters **B281** (1992) 394.

[62] D. Bortoletto *et al.*, Phys. Rev. **D45** (1992) 21.

[63] G. Alexander *et al.*, Physics Lett. **B262** (1991) 341.

[64] P. Abreu *et al.*, Physics Lett. **B252** (1990) 140.

[65] P.D. Acton *et al.*, *A Measurement of the Forward-Backward Charge Asymmetry in Hadronic Decays of the* Z^0, submitted to Phys. Letters B, CERN-PPE/92-119 (1992).

[66] The OPAL Collaboration, *A Measurement of the Forward-Backward Charge Asymmetry of Charm Quarks using* D^* *Mesons*, OPAL Physics Note PN076, (1992).

[67] J.W. Gary, private communication.

[68] M.Z. Akrawy *et al.*, Physics Lett. **B261** (1991) 334.

[69] J. Smith, J.A.M. Vermaseren, G. Grammer, Phys. Rev. **D15** (1977) 3280.

[70] J.R. Carter, *Proc. Joint International Lepton-Photon Symposium & Europhysics Conference on High Energy Physics, Geneva, 1991*, eds. S. Hegarty, K. Potter and E. Quercigh, (World Scientific, Singapore, 1992) vol.2 p. 1.